INTERROGATING THE INFLUENCE OF ELECTRONICS AND SOLVATION ON
THERMODYNAMIC HYDRICITY

Kelsey R. Brereton

A dissertation submitted to the faculty at the University of North Carolina at Chapel Hill in
partial fulfillment of the requirements for the degree of Doctor of Philosophy in the Department
of Chemistry.

Chapel Hill
2018

Approved by:

Alexander J. M. Miller

Frank A. Leibfarth

Gerald J. Meyer

Jillian L. Dempsey

Marcey L. Waters

ABSTRACT

Kelsey R. Brereton: Interrogating the Influence of Electronics and Solvation on Thermodynamic Hydricity
(Under the direction of Alexander J. M. Miller)

A 'hydrogen economy' using dihydrogen (H_2) as a fuel has been proposed as a leading strategy for new environmentally friendly energy sources. Toward this end, the safe and efficient storage of H_2 is an ongoing challenge in successful implementation on an industrial scale. As key catalysts in hydrogenation and hydrogen production reactions, transition metal hydride complexes must balance the strength of the metal hydride bond to maximize reactivity and retain stability. *This work focuses on an in-depth investigation into the intricate thermodynamics that govern these systems and their potential use in guiding catalyst design and optimizing performance.*

The hydricity of metal hydride complexes is a thermodynamic measure of the strength of the metal hydride bond. Hydricity has been measured extensively in acetonitrile and has been used as a valuable tool to guide catalyst design. The utility of these thermodynamic measurements has motivated expanded studies investigating the observed solvent dependence of hydricity. Presented here are three focused studies examining strategies for measurement, solvent dependence, and catalytic utility of hydricity. 1) A bimetallic Ir/Ru catalyst is used as a case study of solvent dependent thermodynamics. The electrochemistry, acidity, hydricity, and electronic structure of the complex is explored in two solvents and applied to a detailed picture describing catalysis observed by the system. 2) Density Functional Theory (DFT) calculations are used to overcome

traditional challenges in aqueous hydricity measurement. Through the development of appropriate training sets to calibrate computational results, the reduction potentials and acidities of a series of iridium complexes are determined in water and used to calculate aqueous hydricities for comparison with experimental values. 3) The first example of a systematic study of the solvent dependence of hydricity across a series of electronically tuned iridium catalysts is presented in acetonitrile and water: this work explores the connection between the influence of electronic tuning and effective hydricity.

This work unveils the thermodynamics driving kinetic observations for transition metal hydride complexes. Through a thorough understanding of the optimal strategies for catalyst tuning in multiple solvents, new generation of systems powering the 'hydrogen economy' can be developed.

ACKNOWLEDGEMENTS

Thankfully, there is one outlet in this experience dedicated to reflection on the incredible journey the last several years has been. I find this section the most difficult to write; I have so much to say and so many people to thank that I imagine I will never be satisfied with the product.

I would like to start by thanking all of the professors at UNC for always having open doors and welcoming discussions of chemistry, basketball and life. Thank you to Jillian Dempsey, Marcey Waters, Jerry Meyer, Frank Leibfarth, Joe Templeton, and Dave Nicewicz for serving as engaged members my thesis committees of past and present. Thank you to the National Science Foundation and the Center for Enabling New Technologies through catalysis for funding and professional support and thank you to UNC for the dissertation completion fellowship.

I have been lucky enough to have several incredible mentors in my scientific career, and Alex is no exception. From the first time I heard him talk at the 2013 ACS Meeting, I knew I wanted to learn from him. Being a member of his lab has been integral to my growth as a chemist and (maybe more importantly) as a person. He had faith in me during the lows of this program, celebrated with me during the highs, and challenged me when I became complacent. Thank you, Alex, for your determination for me to be confident and take ownership of my chemistry and for being a mentor and a friend as I move forward with my career.

I tell people that one of the main reasons I chose UNC was because during the visitation weekend, the current graduate students seemed happy. Somehow, in the mix of long nights in lab, endless drafts of manuscripts, and trying to maintain a personal life, the students at UNC were still happy to be here. I have found that happiness here with the help of my friends. The members of the Miller lab are a supportive and welcoming group of people (that are also weirdly obsessed with puns). Thank you to all of them for making the ridiculous amount of time we spend together in one room enjoyable. Thank you to Javier Grajeda and Andrew Walden for always being down for an adventure. From Friday afternoon blue cups (thanks Fleming) and finding new music at Cat's Cradle to exploring New Haven and Philadelphia together, being with them reminds me how valuable simply being with friends can be. Lauren Gregor (LDOC), thank you for letting me share in the joy of life with you. Whether its weddings, jobs, golf, roadtrips or crossfit, I know there will be laughter and probably a Fall Out Boy soundtrack. Erika Van Goethem and Melissa Gish – I would have lost my mind if you two weren't around to share my crazy with. Guy Goodman, I would have lost a piece of myself without your friendship. Thank you for always being there (with a bottle of wine) to analyze how weird life can be. Thank you to all of my friends at Eyes, Ears, Nose and Paws: Deb Cunningham, Maria Ikenberry, Carolyn Ikenberry, and Lynn Ikenberry for providing a (much needed) diversion from chemistry in the form of puppies and a wonderful community of people. You have all been family to me while mine was so far away.

I need an entirely new ackowledgments section to adequately thank the people that have been there for me since I blessed the world with my presence. Mom, Dad, and Jenny, it has been an insane journey from the kid who wore fanny packs (not ironically) to the slightly older kid that wears lab coats (also not ironically). My relationship with each of you is unique and

irreplaceable. Mom, I am so proud of you. You give so much of yourself to support Jenny and me and we will forever be trying to live up to your example of how to be a mother, a Christian, and a friend. Thank you for flying so far to be with me and make life easier, binge watch Naked and Afraid, and tell me I can get through this. Dad, from my days collecting rocks in the backyard to the time I called you to say I wasn't coming home for the summer because I had joined a research lab, you have never failed to tell me how proud you are of me. I remember so many visits home where we sat on the porch and talked about life and graduate school and I left feeling like maybe I could finish this thing. Your work ethic and dedication to your family is truly inspirational. Jenny, you are my very best friend. Moving across the country has put a lot of strain on our relationship but we have found a way to grow closer through it. Thank you for always being willing to listen and offer advice. You have shown me that the best things in life are worth fighting for and to fight hardest of all for your family. To all of my family, thank you for being so supportive through this process, still making me feel missed, and always being eager to hear about what I'm up to in the lab.

Now, let's get back to the good stuff.

TABLE OF CONTENTS

LIST OF TABLES

LIST OF FIGURES

LIST OF SCHEMES

LIST OF ABBREVIATIONS AND SYMBOLS

$[Bu_4N][PF_6]$	Tetrabutylammonium hexafluorophosphate
ΔE_p	Difference between the peak currents
ΔG^o_{H-}	Hydricity
$\Delta G^o_{H-}(L)$	Effective Hydricity
ΔG^o_{sv}	Solvation energy
ΔG^o_{tr}	Transfer energy (difference between two solvation energies)
Å	Angstrom
B3LYP	Becke, 3-parameter, Lee-Yang-Parr functional
Bpm	Bipyrimidine
Bpy	Bipyridine
cm^{-1}	Wavenumber
Cp*	Pentamethylcyclopentadiene
Cp_2Fe	Ferrocene
CV	Cyclic voltammetry or cyclic voltammogram
δ	Delta-denotes chemical shift in NMR spectroscopy
DCM	Dichloromethane
DFT	Density Functional Theory
DMF	Dimethylformamide
e^-	Electron
E^o	Standard reduction potential
$E^o_{H+/H-}$	Standard reduction potential for H^+

$E_{1/2}$	Reduction potential under certain conditions
eq	Equation
equiv	Equivalent
HMDF	Protonated dimethylformamide
HOMO	Highest occupied molecular orbital
i	Current
ICP-MS	Inductively coupled plasma-mass spectrometry
kcal mol^{-1}	Kilocalories per mole
LANL2DZ	Los Alamos National Laboratory Effective Core Potential
λ_{max}	Wavelength of maximum absorbtion
LUMO	Lowest unoccupied molecular orbital
μ	micro
M	Molarity
M06	Minnesota functional
mC	Millicoloumb
Me	Methyl
MeCN	Acetonitrile
mL	Milliliters
mV	Millivolts
NHE	Normal hydrogen electrode
NMR	Nuclear magnetic resonance
PBE	Perdew-Burke-Ernzerhof functional
PCM	Polarizable continuum model of solvation

pK_a	Acidity
RVC	Reticulated vitreous carbon electrode
S$_0$	Singlet state
TD-DFT	Time-Dependent Density Functional Theory
THF	Tetrahydrofuran
Triflate	trifluoromethanesulfonate
Triflic acid	Trifluoromethanesulfonic acid
UV-Vis	Ultra-violet/visible spectroscopy

Chapter 1: Introduction

1.1   Metal Hydride Catalysts for Hydrogen Storage Applications

Hydrogen (H_2) as a fuel is at the forefront of strategies for environmentally friendly

energy sources that minimize global consumption of fossil fuels.[1–3] While H_2 is a clean source of

energy, releasing only water upon combustion, it requires storage in high-pressure or cryogenic

tanks. These storage technologies require significant energy to achieve for widespread

commercial use when compared with traditional liquid fuel sources, such as gasoline.[2,4]

Scheme 1.1. Examples of different strategies for hydrogen storage.
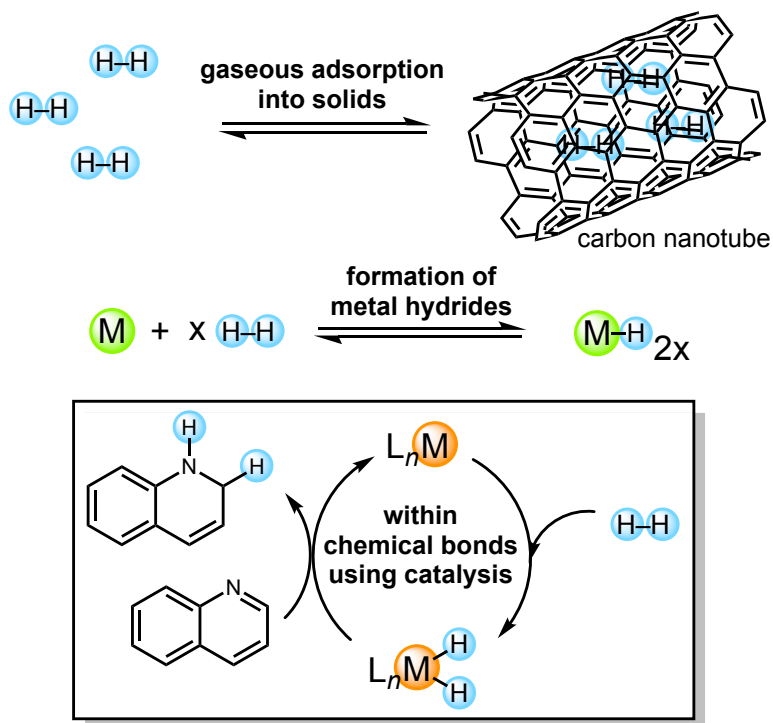
Current strategies to avoid the obstacles of transporting H_2 are focused on new storage methods (Scheme 1.1). Adsorption of gaseous hydrogen can occur in solids[5–7] or within complex metal hydrides (such as MgH_2). H_2 can also be stored within chemical bonds in organic molecules via metal hydride catalysts.[8,9] The heterolytic cleavage of H_2 for storage within chemical bonds is an attractive option for several reasons. The choice of substrate for hydrogenation provides flexibility, enabling the storage of hydrogen in liquid fuels that mitigate many of the safety concerns that arise when using high pressure or cryogenic tank strategies. Additionally, fuels with high energy density can be generated by focusing on compounds that maximize hydrogen capacity per unit mass.[10–12] The successful implementation of any strategy outlined in Scheme 1.1 requires an intimate understanding of the kinetics and thermodynamics of H_2 cleavage and H_2 production. Storage in solid materials and within complex hydrides must be reversible, requiring a careful balance of adsorption and desorption thermochemistry. The thermodynamics of metal hydrides, which is the focus of this work, must also be modulated in order to cleave H_2 to form a stable metal hydride species that is also reactive enough to release H_2 or transfer the H_2 equivalent to a substrate.

Transition metal hydride complexes are key players in many hydrogenation or hydrogen production reactions relevant to energy storage schemes.[13–16] A storage scheme fueled by catalysis requires complexes that can (a) hydrogenate organic molecules to store H_2 equivalents and (b) dehydrogenate those molecule in order to release H_2. Homogeneous hydrogenation and transfer hydrogenation by transition metal complexes is well documented in the literature.[15,17–19] Complexes like Wilkinson's catalyst ([$Rh(PPh_3)_3Cl$]; Ph = phenyl) and Crabtree's catalyst ([$Ir(COD)(Py)PCy_3$]$^+$; COD = cyclooctadiene, Py = pyridine, PCy_3 = tricyclohexylphosphine) are highly efficient at olefin hydrogenation.[20] Heteroarenes also present an attractive option for

storage materials due to a high potential for hydrogen capacity (Scheme 1.1). These heterocycles

are also common substrates for hydrogenation catalysis.[21,22] Hydrogen release from organic

molecules via dehydrogenation catalysis can also be driven using transition metal complexes.[23]

Iridium pincer complexes are capable of efficient dehydrogenation of alkanes as well as

substrates with heteroatom-hydrogen bonds (such as amines).[24,25] Iridium complexes similar to

those investigated in this study (*vida infra*) catalyze both the hydrogenation and dehydrogenation

of quinolines such as the one depicted above, showing promise for a thermodynamically

accessible and reversible scheme for hydrogen storage.

1.2   Metal Hydride Thermodynamics

Scheme 1.2. Methods of metal hydride bond cleavage to generate H^+, $H^\bullet$, or H^-.
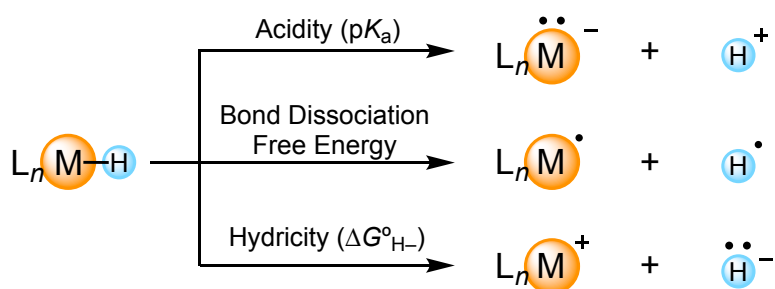
After protonation at the metal center to generate the hydride, several potential modes of

reactivity exist. Complexes such as these can accept an additional proton to form H_2 complexes

or cleave the metal hydride to release H^+ (acting as an acid), release H^- (acting as a hydride

donor), or release $H^\bullet$ (acting as a hydrogen atom donor).[26–28] The versatility of transition metal

hydrides is responsible for the wide range of transformations accessible through these species

and the mode of reactivity is governed by the thermodynamics and kinetics involved in metal

hydride bond cleavage (Scheme 1.2).

Scheme 1.3. Selected examples representing the variety of mechanisms available for hydrogenation catalysts.
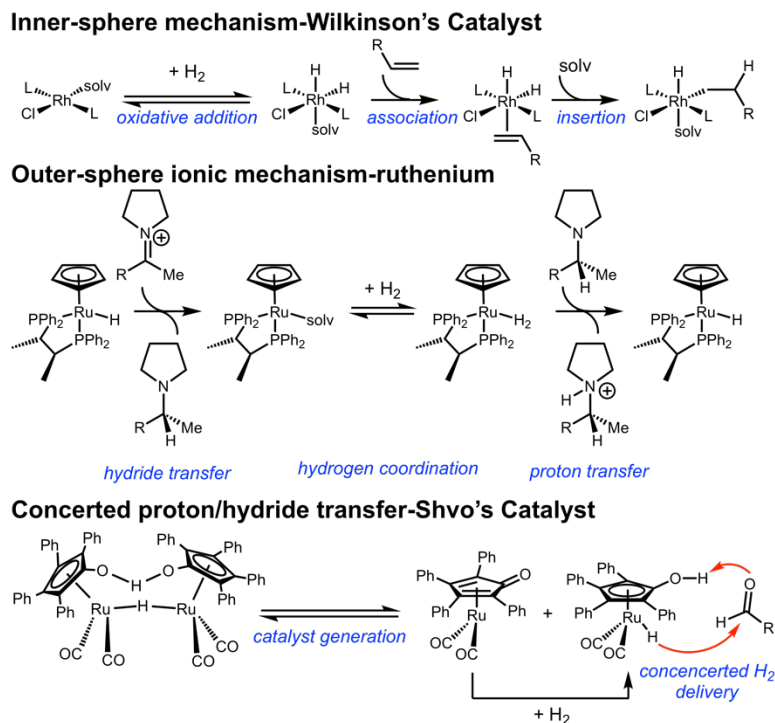
The Brønsted acidity or basicity of the hydride ligand can have important implications in the mechanism of hydrogenation reactions.[27] For example, Wilkinson's olefin hydrogenation catalyst operates through oxidative addition of dihydrogen to generate a dihydride complex followed by olefin insertion into the metal-hydride bond. Finally, reductive elimination yields the desired product (Scheme 1.3, top).[20] The thermodynamics of the metal hydride bond are significant to promoting the activity of this catalyst as evidenced by the turnover-limiting, migratory insertion step. Co-solvents such as ethanol are suggested to facilitate this step, also highlighting the value of knowledge of the solvent-dependence of metal hydride thermodynamics. Alternatively, hydrogenation catalysts can operate through an outer-sphere mechanism, such as in the hydrogenation of ketones and imines by ruthenium complexes. The catalyst shown in center reaction of Scheme 1.3 operates through an ionic mechanism, where H_2 is transferred as proton and hydride equivalents.[15] Within this subset of ionic hydrogenations, the

order of hydride transfer or proton transfer from the metal is highly dependent on the balance of the acidity of the metal hydride and substrate. Some structurally similar transition metal hydrides, such as $[(Cp)W(H)(CO)_3]$, $[(Cp)Mo(H)(CO)_2(PPh_3)]$, and $[Re(H)(CO)_5]$ display different types of reactivity depending on the substrate and conditions.[15] One illustration of this reactivity is the ionic hydrogenation of hindered olefins by $[(Cp)W(H)(CO)_3]$ and trifluoroacetic acid (CF_3SO_3H). Modulating the acidity of the tungsten hydride avoids irreversible protonation of the metal hydride to release H_2. Instead, product formation is achieved by protonation of the substrate by the acid and hydride donation by the metal.[15,29,30] In addition, hydrogenation has been shown to occur in a concerted fashion. An in depth mechanistic investigation of hydrogenation by Shvo's catalyst concluded that proton transfer from OH^- occurs concurrently with hydride transfer from Ru (bottom of Scheme 1.3).[31] Though hydrogenation can occur through a variety of mechanisms, metal hydrides remain a focus in all three. Knowledge of the thermodynamics governing the reactivity of these complexes will aide in the development of new strategies for efficient hydrogenation catalysis.

This work focuses on the solvent dependence of the third method of heterolytic M–H bond scission shown in Scheme 1.2, hydricity. Solvent dependent thermodynamics and kinetics of several iridium complexes will be explored in both water and acetonitrile as they relate to catalysis. Both experimental and computational strategies will be employed to dissect the factors governing the hydricity of transition metal hydride complexes.

The choice of hydricity is motivated by the increasing number of examples of hydricity governing the rational design of improved catalysts.[26] For example, in acetonitrile, a systematic study of the hydride donating abilities for a series of Ni diphosphine species resulted in the construction of a library of complexes that can be used for H_2 oxidation as well as H_2

5

production.[32] This study culminated in the development of a catalyst that can outperform the hydrogenase enzyme itself in H_2 production under some conditions.[33] These studies have spurred a dramatic growth (to date more than 100 values are known) in the number of hydricities determined for transition metal hydrides in acetonitrile.[26]

The developing knowledge of hydricity in acetonitrile has led to an increasing interest in the solvent dependence of hydricity, specifically in aqueous media. Aqueous hydride transfer reactions are implicated in many transformations relevant to water-splitting catalysis,[34] CO_2 reduction,[35] and hydrogenation catalysis relevant to hydrogen storage.[36,37] The unique properties of the highly polar water solvent have impeded traditional strategies for aqueous hydricity measurement.

1.3 Strategies for the Measurement of Thermodynamic Hydricity

Thermodynamic hydricity involves the release of free hydride ion, H^-, which is too reactive for direct experimental measurements. As such, the measurement of hydricity relies on the construction of a thermodynamic cycle composed of the acidity of the hydride along with the reduction potential of the conjugate base (Scheme 1.4).

Scheme 1.4. Potential–pK_a thermodynamic cycle for the determination of hydricity

$$L_nM\text{–}H^+ \rightleftharpoons L_nM + H^+ \qquad 1.364(pK_a) \quad (1)$$

$$L_nM \rightleftharpoons L_nM^{2+} + 2e^- \qquad -(-46.12E^o) \quad (2)$$

$$H^+ + 2e^- \rightleftharpoons H^- \qquad -(-46.12E^o_{H+/H-}) \quad (3)$$

$$L_nM\text{–}H^+ \rightleftharpoons L_nM^{2+} + H^- \qquad \Delta G^o_{H-} \quad (4)$$
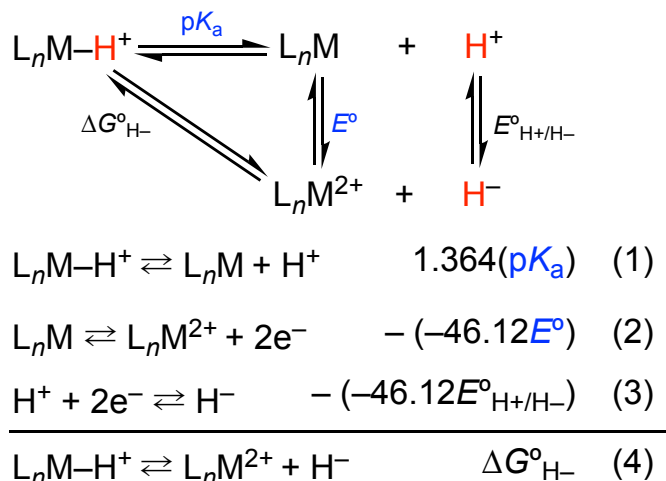
The thermodynamic cycle shown in Scheme 1.4 can be used for the determination of hydricity in any solvent, provided the constant for proton reduction is known, and the acidity and electrochemical measurements are feasible. Acetonitrile provides a convenient media for the pK_a–potential thermodynamic cycle, as the electrochemistry is relatively well behaved and there is an extensive acidity scale in acetonitrile.[38,39] Water would seem to feature favorable properties for hydricity measurements, as well. However, upon moving into aqueous solvent, several complications with this strategy arise for measurements involving organometallic hydrides. The conjugate base, (L$_n$M in Scheme 1.4) is neutral for monocationic metal hydrides and often insoluble in water. This insolubility leads to precipitation in titrations aimed at measuring acidity and adsorption to the electrode surface in electrochemical experiments.[40] In chapter 2, these challenges are overcome in water through investigation of a bimetallic iridium-ruthenium hydride complex with a dicationic conjugate base. The solubility imparting (bpm)Ru(bpy)$_2^{2+}$ (bpm = 2,2'-bipyrimidine and bpy = 2,2-bipyridine) metalloligand enables acidity measurements through spectrophotometric titration and straightforward electrochemical analysis by cyclic voltammetry. The hydricity for the bimetallic iridium-ruthenium complex was determined in both water and acetonitrile, adding another complex to those with hydricities determined in multiple solvents.[41–43]

Another avenue to obtain aqueous hydricity is through the development of accurate computational models that enable determination using Density Functional Theory (DFT). Chapter 3 capitalizes on computational strategies for the determination of acidity[44,45] and reduction potential[46–48] as well as a few reports of hydricity determination in acetonitrile.[49–51] Through the development of accurate training sets based on experimentally determined values to calibrate theoretical calculations, the hydricities of a series of [Cp*Ir(bpy-X)(H)]$^+$ (Cp* = η^5-

pentamethylcyclopentadienyl; bpy-R = 4,4'-substituted 2,2'-bipyridine) complexes in water. As

mentioned above, direct measurement of these monocationic hydrides using a pK_a–potential

thermodynamic cycle is impossible due to the insolubility of the neutral conjugate base.

Scheme 1.5. Equilibration methods to obtain relative hydricity of a complex $L_nM–H^+$.

Equilibration with external reference

$$L_nM–H^+ + ref^{2+} \xrightleftharpoons{K_{eq}} L_nM^{2+} + ref–H^+$$

$L_nM–H^+ + ref^{2+} \rightleftharpoons L_nM^{2+} + ref–H^+$	$-RT\ln(K_{eq})$ (5)
$ref^{2+} + H^- \rightleftharpoons ref–H^+$	$\Delta G^\circ_{H–(ref–H+)}$ (6)
$L_nM–H^+ \rightleftharpoons L_nM^{2+} + H^-$	$\Delta G^\circ_{H–}$ (4)

Equilibration with H$_2$

$$L_nM^{2+} + H_2 \xrightleftharpoons{K_{eq}} L_nM–H^+ + H^+$$
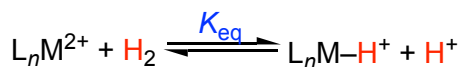
$L_nM^{2+} + H_2 \rightleftharpoons L_nM–H^+ + H^+$	$-RT\ln(K_{eq})$ (5)
$H^+ + H^- \rightleftharpoons H_2$	$-HBDE(H_2)$ (7)
$L_nM^{2+} + H^- \rightleftharpoons L_nM–H^+$	$-\Delta G^\circ_{H–}$ (4)

In order to experimentally determine aqueous hydricities for complexes without water

soluble conjugate bases, relative hydricities can be determined through equilibration with a

complex of known hydricity or with H_2 (Scheme 1.5). This method has been used widely in

acetonitrile to add complexes to the known scale of hydricities.[52–54] Applying this method in

water led our group to a general method for aqueous hydricity determination.[40] Through these

studies the hydricities of five structurally homologous Ir complexes and three Ru complexes

were determined in water. These measurements provided a dramatic contribution not only to the

number of known aqueous hydricities, but also to the knowledge of factors governing hydricity

in water. Synthetic modification to the 2,2'-bipyridine ligands was found to have a relatively

small influence on hydricity (~ 3 kcal mol^{-1}). Instead, the stability of the complex formed after

hydride donation was found to have a significantly stronger influence on the thermodynamics of hydride donation.
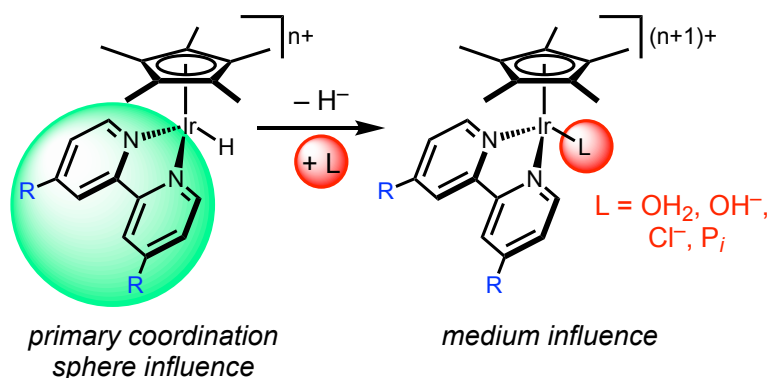
Figure 1.1. Factors influencing aqueous hydricity: modest effects resulting from substitution of the bipyridine supporting ligand and more pronounced effects from tuning the medium to form a stable complex after hydride donation.

Effective hydricity is a thermodynamic hydricity parameter that also includes the influence of incoming ligands on the hydride donating ability of a complex.[26,40] As the 16e$^-$ species formed after hydride donation is often unstable, the measured hydricity is that of hydride donation coupled with the association energy of the ligand that coordinates to the metal center. The binding affinity for the metal center will be different for each solvent as well as with any salt additives or buffers, making effective hydricity of particular importance in water. However, to date, the influence of solvation on effective hydricity is unknown.

The final chapter assembles the knowledge gained from aqueous hydricity studies in our lab and solvation dependence studies of individual complexes to conduct a systematic study of the hydricities of a family of complexes in two solvents. Through the investigation of a series of structurally homologous iridium hydrides, the influence of solvation on the magnitude of hydricity, the extent of electronic tuning, and the impact of effective hydricity can be measured. One could expect that substituent effects would be greater in a solvent less efficient at

solubilizing charged ions. For example, in studies of phenols and benzoic acid derivatives, acidity is more than twice as sensitive to substitution in acetonitrile when compared with water.[55] Additionally, the influence of the ligand that coordinates the metal center upon hydride donation could be influenced by solvation. The effect of chloride on both the thermodynamics and kinetics of hydride transfer are explored in acetonitrile to compare with aqueous measurements. Finally, the origin of the dramatic solvent dependence of hydricity are examined using Density Functional Theory and empirical methods to determine the free energy difference between the solvation of the hydride ion and the metal-containing species in water and acetonitrile. This knowledge of thermochemistry puts us in a better position to correlate thermodynamic parameters with catalytic activity and selectivity.

1.4   Rationalizing Hydrogen Generation from Metal Hydrides with Thermodynamics

The family of iridium complexes that was investigated in thermochemical studies in water are proposed intermediates in a number of H_2 generating reactions.[56–58] The very stability of the $[Cp^*Ir(bpy)(H)]^+$ catalysts depends on the aqueous hydricity of these species (Figure 1.2). Hydricity can be used to determine the pH at which H_2 release in the ground state is thermodynamically favorable (blue area in Figure 1.2). When coupled with the acidity of a hydride, a full pH stability diagram can be calculated.
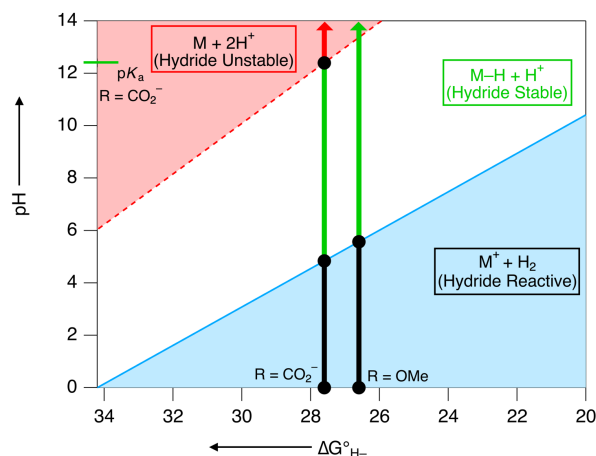
Figure 1.2. Plot of pH vs. hydricity (ΔG°_{H-}) illustrating the regions of stability of transition metal hydrides. The dashed red line is an estimation of the relationship between the hydride pK_a and the hydricity, based on DFT calculated trends.[59] At higher pH values the hydride will be deprotonated (red shading), precluding further reactivity. The blue solid line is the pH at which H_2 release in the dark is thermoneutral for a hydride with a given ΔG°_{H-}; in the white region, the hydride is stable (green lines), while in the blue shaded region, the hydride will release H_2 in the dark (black lines). Black circles represent the stability boundaries of $[Cp*Ir(bpy-CO_2)(H)]^-$ and $[Cp*Ir(bpy-OMe)(H)]^+$.

As seen from Figure 1.2, the iridium hydrides under study are stable to H_2 release in water at neutral pH. This stability enabled the thermochemical studies described above. However, ideal catalytic H_2 production catalysts could operate at neutral pH, negating the use of strong acids or harsh conditions. Our group has discovered that H_2 production from neutral water can be achieved by introducing a photochemical step into catalysis.[60] In this way, the stability of these hydrides can be retained while maintaining catalytic activity upon irradiation. This reactivity can also be expanded to photochemical formic acid dehydrogenation to formate, which can be coupled with CO_2 capture at basic pH to exclusively release pure H_2, as desired for a good H_2 carrier.[61] This work has been developed in our lab to establish the growing field of photoelectrocatalytic H_2 production.[60,62]

In photoelectrocatalysis, a single molecule performs both light absorption and H_2 bond formation. As is common in many catalyst design schemes, optimization of one step influences other steps in the catalytic cycle as well. For photoelectrocatalysis, several correlations were found between the thermodynamic parameters governing catalyst activity (Figure 1.3).
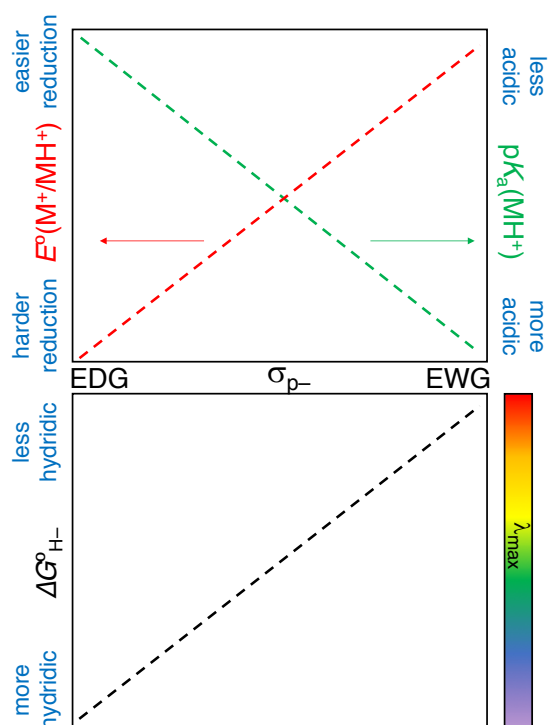
Figure 1.3. Correlation diagrams describing the general relationship between the electronic properties of the bipyridine ligand and the thermodynamic factors governing photoelectrocatalysis (EDG is electron donating group, EWG is electron withdrawing group).

These scaling relationships can be used to guide catalyst optimization. As synthetic modification to the bipyridine ligand tunes the hydricity of a complex, it also influences the absorptivity, reduction potential, and acidity. All of these factors need to be considered when making a synthetic adjustment. Effective hydricity adds another consideration that could be beneficial in aqueous photoelectrocatalysis. It is known that the addition of chloride will make

hydride donation more thermodynamically favorable and reduction less favorable.[40,60] For this application, optimizing the reduction potential will have more of an impact on the efficiency of the reaction as the hydride transfer is photochemically driven. An intimate knowledge of the thermodynamics of the metal hydride involved in catalysis can lead to more intelligently and efficiently designed photoelectrocatalysts.

In the quest for more efficient alternative energy strategies, transition metal hydrides are key players in homogeneous hydrogenation and hydrogen production schemes. Thermodynamic hydricity provides a valuable means for translating observed reactivity into a template that can be applied to guide catalyst design.

REFERENCES

(1)   Schlapbach, L.; Züttel, A. *Nature* **2001**, *414*, 353.

(2)   Jena, P. *J. Phys. Chem. Lett.* **2011**, *2*, 206.

(3)   Teets, T. S.; Nocera, D. G. *Chem. Commun.* **2011**, *47*, 9268.

(4)   Holladay, J. D.; Hu, J.; King, D. L.; Wang, Y. *Catal. Today* **2009**, *139*, 244.

(5)   Sircar, S.; Golden, T. C.; Rao, M. B. *Carbon N. Y.* **1996**, *34*, 1.

(6)   Rosi, N. L.; Eckert, J.; Eddaoudi, M.; Vodak, D. T. *Science* **2003**, *300*, 1127.

(7)   Ma, S.; Zhou, H. C. *Chem. Comm.* **2010**, *46*, 44.

(8)   Sakintuna, B.; Lamari-Darkrim, F.; Hirscher, M. *Int. J. Hydrogen Energy* **2007**, *32*, 1121.

(9)   Orimo, S.-I.; Nakamori, Y.; Eliseo, J. R.; Züttel, A.; Jensen, C. M. *Chem. Rev.* **2007**, *107*, 4111.

(10) Lewis, N. S.; Nocera, D. G. *Proc. Natl. Acad. Sci.* **2006**, *103*, 15729.

(11) Esswein, A. J.; Nocera, D. G. *Chem. Rev.* **2007**, *107*, 4022.

(12) Cook, T. R.; Dogutan, D. K.; Reece, S. Y.; Surendranath, Y.; Teets, T. S.; Nocera, D. G. *Chem. Rev.* **2010**, *110*, 6474.

(13) Jessop, P. G.; Joó, F.; Tai, C. C. *Coord. Chem. Rev.* **2004**, *248*, 2425.

(14) Young, J. F.; Osborn, J. A.; Jardine, F. H.; Wilkinson, G. *Chem. Commun.* **1965**, 131.

(15) Bullock, R. M. *Chem. Eur. J.* **2004**, *10*, 2366.

(16) Fukuzumi, S.; Suenobu, T. *Dalton Trans.* **2013**, *42*, 18.

(17) Wang, D.; Astruc, D. *Chem. Rev.* **2015**, *115*, 6621.

(18) Clapham, S. E.; Hadzovic, A.; Morris, R. H. *Coord. Chem. Rev.* **2004**, *248*, 2201.

(19) Xie, J.-H.; Zhu, S.-F.; Zhou, Q.-L. *Chem. Rev.* **2011**, *111*, 1713.

(20) Hartwig, J. F. *Organotransition Metal Chemistry*; University Science Books: Mill Valley.

(21) Crabtree, R. H. *Energy Environ. Sci.* **2008**, *1*, 134.

(22) Zhou, Y. G. *Acc Chem Res* **2007**, *40*, 1357.

(23) Choi, J.; MacArthur, A. H. R.; Brookhart, M.; Goldman, A. S. *Chem. Rev.* **2011**, *111*, 1761.

(24) Bernskoetter, W. H.; Brookhart, M. *Organometallics* **2008**, *27*, 2036.

(25) Liu, F.; Goldman, A. S. *Chem. Commun.* **1999**, 655.

(26) Wiedner, E. S.; Chambers, M. B.; Pitman, C. L.; Bullock, R. M.; Miller, A. J. M.; Appel, A. M. *Chem. Rev.* **2016**, *116*, 8655.

(27) Morris, R. H. *Chem. Rev.* **2016**, *116*, 8588.

(28) Hu, Y.; Shaw, A. P.; Estes, D. P.; Norton, J. R. *Chem. Rev.* **2016**, *116*, 8427.

(29) Bullock, R. M.; Song, J.-S. *J. Am. Chem. Soc.* **1994**, *116*, 8602.

(30) Bullock, R. M.; Rappoli, B. J. *J. Chem. Soc. Chem. Commun.* **1989**, 1447.

(31) Casey, C. P.; Singer, S. W.; Powell, D. R.; Hayashi, R. K.; Kavana, M. *J. Am. Chem. Soc.* **2001**, *123*, 1090.

(32) Fraze, K.; Wilson, A. D.; Appel, A. M.; Rakowski DuBois, M.; DuBois, D. L. *Organometallics* **2007**, *26*, 3918.

(33) Helm, M. L.; Dubois, M. R.; Dubois, D. L. *Science* **2011**, *333*, 863.

(34) Thoi, V. S.; Sun, Y.; Long, J. R.; Chang, C. J. *Chem. Soc. Rev.* **2013**, *42*, 2388.

(35) Mcdaniel, N. D.; Bernhard, S. *Dalton Trans.* **2010**, *39*, 10021.

(36) Robertson, A.; Matsumoto, T.; Ogo, S. *Dalton Trans.* **2011**, *40*, 10304.

(37) Joó, F. *Acc. Chem. Res.* **2002**, *35*, 738.

(38) Eckert, F.; Leito, I.; Kaljurand, I.; Kütt, A.; Klamt, A.; Diedenhofen, M. *J. Comput. Chem.* **2009**, *30*, 799.

(39) Kaljurand, I.; Kütt, A.; Sooväli, L.; Rodima, T.; Mäemets, V.; Leito, I.; Koppel, I. A. *J. Org. Chem.* **2005**, *70*, 1019.

(40) Pitman, C. L.; Brereton, K. R.; Miller, A. J. M. *J. Am. Chem. Soc.* **2016**, *138*, 2252.

(41) Connelly Robinson, S. J.; Zall, C. M.; Miller, D. L.; Linehan, J. C.; Appel, A. M. *Dalton Trans.* **2016**, *45*, 10017.

(42) Tsay, C.; Livesay, B. N.; Ruelas, S.; Yang, J. Y. *J. Am. Chem. Soc.* **2015**, *137*, 14114.

(43) Taheri, A.; Thompson, E. J.; Fettinger, J. C.; Berben, L. A. *ACS Catal.* **2015**, *5*, 7140.

(44) Muckerman, J. T.; Skone, J. H.; Ning, M.; Wasada-Tsutsui, Y. *Biochim. Biophys. Acta* **2013**, *1827*, 882.

(45) Qi, X.-J.; Liu, L.; Fu, Y.; Guo, Q.-X. *Organometallics* **2006**, *25*, 5879.

(46) Marenich, A. V.; Majumdar, A.; Lenz, M.; Cramer, C. J.; Truhlar, D. G. *Angew. Chem. Int. Ed.* **2012**, *51*, 12810.

(47) Marenich, A. V; Ho, J.; Coote, M. L.; Cramer, C. J.; Truhlar, D. G. *Phys. Chem. Chem. Phys.* **2014**, *16*, 15068.

(48) Baik, M. H.; Friesner, R. A. *J. Phys. Chem. A* **2002**, *106*, 7407.

(49) Qi, X. J.; Fu, Y.; Liu, L.; Guo, Q. X. *Organometallics* **2007**, *26*, 4197.

(50) Muckerman, J. T.; Achord, P.; Creutz, C.; Polyansky, D. E.; Fujita, E. *Proc. Natl. Acad. Sci.* **2012**, *109*, 15657.

(51)   Kovács, G.; Pápai, I. *Organometallics* **2006**, *25*, 820.

(52)   Rakowski DuBois, M.; DuBois, D. L. *Acc. Chem. Res.* **2009**, *42*, 1974.

(53)   William W. Ellis, James W. Raebiger, Calvin J. Curtis, Joseph W. Bruno, and D. L. D. *J. Am. Chem. Soc.* **2004**, *126*, 2738.

(54)   Ellis, W. W.; Ciancanelli, R.; Miller, S. M.; Raebiger, J. W.; DuBois, M. R.; DuBois, D. L. *J. Am. Chem. Soc.* **2003**, *125*, 12230.

(55)   Chantooni, M. K.; Kolthoff, I. M. *J. Phys. Chem.* **1976**, *80*, 1306.

(56)   Ogo, S.; Makihara, N.; Kaneko, Y.; Watanabe, Y. *Organometallics* **2001**, *20*, 4903.

(57)   Miller, A. J. M.; Heinekey, D. M.; Mayer, J. M.; Goldberg, K. I. *Angew. Chem. Int. Ed.* **2013**, *52*, 3981.

(58)   Brewster, T. P.; Ou, W. C.; Tran, J. C.; Goldberg, K. I.; Hanson, S. K.; Cundari, T. R.; Heinekey, D. M. *ACS Catal.* **2014**, *4*, 3034.

(59)   Brereton, K. R.; Bellows, S. M.; Fallah, H.; Lopez, A. A.; Adams, R. M.; Miller, A. J. M.; Jones, W. D.; Cundari, T. R. *J. Phys. Chem. B* **2016**, *120*, 12911.

(60)   Pitman, C. L.; Miller, A. J. M. *ACS Catal.* **2014**, *4*, 2727.

(61)   Barrett, S. M.; Slattery, S. A.; Miller, A. J. M. *ACS Catal.* **2015**, *5*, 6320.

(62)   Brereton, K. R.; Bonn, A. G.; Miller, A. J. M. *ACS Energy Lett.* **2018**, *accepted*.

Chapter 2: Solvent-Dependent Thermochemistry of an Iridium/Ruthenium H₂ Evolution Catalyst

2.1   Introduction

The bimetallic hydride $[Cp*Ir(H)(\mu\text{-bpm})Ru(bpy)_2]^{3+}$ (**1**, Scheme 2.1) has been implicated as an intermediate in the catalytic dehydrogenation of formic acid to CO_2 and H_2,[1] the four-electron reduction of oxygen,[2] and the photocatalytic production of H_2 in conjunction with a $[Ru(bpy)_3]^{2+}$ photosensitizer[3] in aqueous solvent. In formic acid dehydrogenation, the bimetallic catalyst (as the sulfate salt) produces H_2 with turnover frequencies greater than 400 h^{-1} via an unusual hydrogen tunneling mechanism.[1] The photocatalytic production of H_2 from **1** was not observed without additional $[Ru(bpy)_3]^{2+}$, despite containing a fragment of the widely used chromophore[4–8] as part of its ligand scaffold. Instead of functioning as a light absorber itself, as observed in other Cp*Ir-supported hydride complexes,[9–11] a separate $[Ru(bpy)_3]^{2+}$ chromophore initiates catalysis by electron transfer to the bimetallic species leading to **1** after protonation. The high catalytic activity of **1** in water motivated thermochemical and electronic structure studies.

The transformations illustrated in Scheme 2.1 are all proposed to involve an iridium hydride intermediate. The thermochemistry of the metal–hydride bond may therefore provide valuable insight into the catalytic reactivity. Thermodynamic hydricity ($\Delta G°_{H–}$),[12] the free

energy required to heterolytically cleave the metal–hydride bond and release H⁻, has been used

to predict or explain the reactivity of metal hydride complexes.[13–20]

Scheme 2.1. Reactions catalyzed by 1 in water.
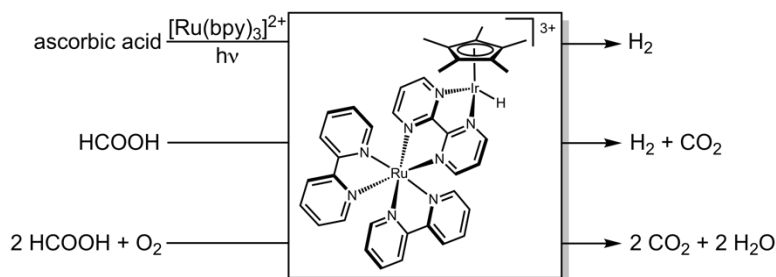
Several experimental methods to measure $\Delta G°_{H-}$ have been established, including the

common practice of establishing equilibrium with H_2 or another hydride donor/acceptor pair of

known hydricity.[21,22] Alternatively, a "potential–pK_a" thermochemical cycle can provide

hydricity values without need for a known reference species. Equations 1 - 4 show how hydricity

(eq 4) can be determined through measurement of the pK_a of the hydride (eq 1) and the reduction

potential of its conjugate base (eq 2), along with the free energy for the reduction of a proton to a

hydride (eq 3).

$$[M–H]^+ \leftrightarrows [M] + H^+ \qquad\qquad 1.365(pK_a) \qquad (1)$$
$$[M] \leftrightarrows [M]^{2+} + 2e^- \qquad\qquad -[-46.12(E°)] \qquad (2)$$
$$H^+ + 2e^- \leftrightarrows H^- \qquad\qquad -46.12(E°_{H+/H-}) \qquad (3)$$
$$[M–H]^+ \leftrightarrows [M]^{2+} + H^- \qquad\qquad \Delta G°_{H-} \qquad (4)$$

Despite sustained interest in developing aqueous catalytic reactions that utilize metal

hydrides, hydricity measurements in water have only recently seen significant development. As a

result, hydricity comparisons between different solvents are also rare. A breakthrough in this

area came from Creutz and coworkers who determined the hydricity of two Ru complexes in

water[23,24] and acetonitrile.[25] More recently, the Berben group determined the hydricity of an Fe

electrocatalyst in both water and acetonitrile,[19] and the groups of Yang[18] and Appel[26] established

18

the hydricity of Ni hydrides in both solvents. Miller *et al.* also determined the hydricity of $[Cp*Ir(bpy)(H)]^+$ in both acetonitrile[10] and water.[20]

Solvent effects on hydricity can be substantial. In general, hydride complexes are more hydridic (lower $\Delta G°_{H-}$ value) in water.[12] The efficacy of ion solvation by the solvent has been recognized as important in contributing to this trend. Ligands present in water can also influence hydricity; water, hydroxide, or anions in the aqueous medium can bind the metal center as ligands following hydride release.[20] The bimetallic system under investigation here can be conveniently studied in both acetonitrile and water, owing to the favorable solubility profile imparted by the doubly-charged Ru polypyridyl unit. We have fully characterized several bimetallic intermediates proposed in the catalytic cycles for aqueous catalysis and established the thermodynamic hydricity of $[Cp*Ir(H)(\mu\text{-}bpm)Ru(bpy)_2]^{3+}$ (**1**) in water and acetonitrile.

2.2   Results and Discussion

2.2.1   Characterization of 2-OH₂ in water.

The complex investigated in prior studies was the sulfate salt of $[Cp*Ir(OH_2)(\mu\text{-}bpm)Ru(bpy)_2]^{4+}$ (**2-OH₂**).[1] Initial efforts to isolate $[Cp*Ir(OH_2)(\mu\text{-}bpm)Ru(bpy)_2][SO_4]_2$ were complicated by sulfate coordination to the iridium center. In order to avoid this speciation and to maintain solubility in both MeCN and H₂O, the corresponding trifluoromethanesulfonate (triflate, $SO_3CF_3^-$) salt was targeted. Stirring $[Cp*Ir(OH_2)_3][SO_3CF_3]_2$ and $[Ru(bpy)_2(bpm)][SO_3CF_3]_2$ in water adjusted to pH 2 with dilute triflic acid under N₂ afforded dark, forest green aqua complex **2-OH₂** in 94% yield. Adding Na₂SO₄ to the triflate salt of **2-OH₂** in D₂O resulted in equilibrium mixtures of **2-OH₂** and **2-SO₄** (Figure 2.1). The Cp* resonance (^{1}H NMR δ 1.71 in D₂O) of **2-SO₄** is consistent with Fukuzumi's prior report.[1]
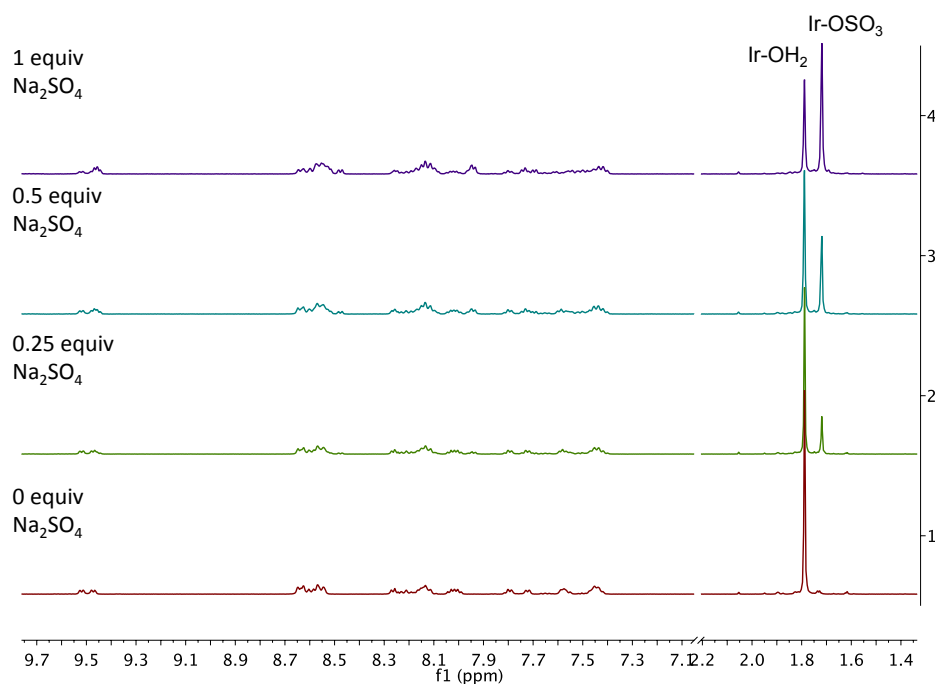
Figure 2.1. ^{1}H NMR spectrum of **2-OH$_2$** and **2-OH$_2$** with addition of Na$_2$SO$_4$ (0-1 equiv.) to form the sulfate bound complex [Cp*Ir(OSO$_3$)(μ-bpm)Ru(bpy)$_2$][SO$_4$] reported previously.[1] HRMS (ESI[+]) of independently prepared [Cp*Ir(OSO$_3$)(μ-bpm)Ru(bpy)$_2$][SO$_4$] *m/z* [Cp*Ir(OSO$_3$)(μ-bpm)Ru(bpy)$_2$] calcd, 498.07; found, 498.10.

In order to establish the protonation state of the complex under the experimental conditions the acidity of the aqua ligand of **2-OH$_2$** was measured. The pK_a was determined by spectrophotometric titration of hydroxo complex [Cp*Ir(OH)(μ-bpm)Ru(bpy)$_2$]$^{3+}$ (**4**) with phosphoric acid to form aqua complex **2-OH$_2$**.
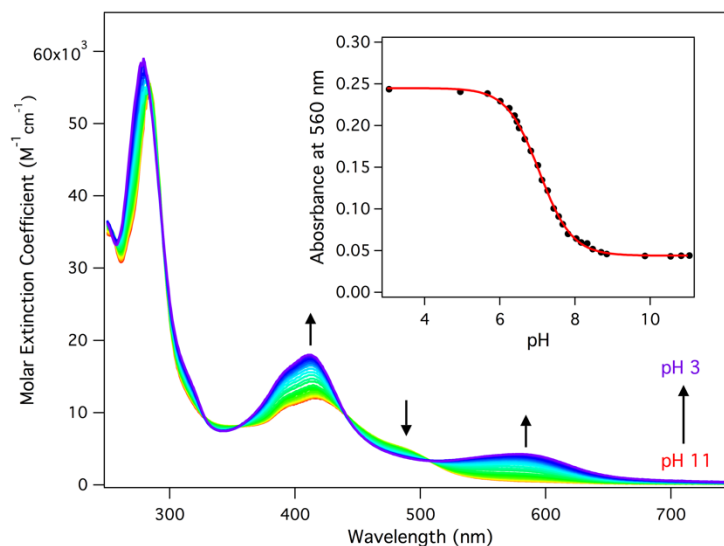
Figure 2.2. Spectrophotometric titration of **4** (red trace) to form **2-OH$_2$** (purple trace) in 0.1 M sodium phosphate. Inset shows absorbance at 560 nm (black circles) and least-squares fitting to the Henderson-Hasselbalch equation (red line) to give a pK_a = 7.0 ± 0.1.

The change in the absorbance at three different wavelengths (400, 560, and 600 nm) as a function of pH was fit to the Henderson-Hasselbalch equation to provide a pK_a of 7.0 ± 0.1 (Figure 2.2, inset). Structurally related aqua complexes [Cp*Ir(bpy-X)(OH$_2$)]$^{2+}$ (bpy-X refers to substitution at the 4 and 4' positisions on 2,2'-bipyridine; X= H, OMe, or COO$^-$), [(η^6-C$_6$Me$_6$)Ru(bpy-X)(OH$_2$)]$^{2+}$ (X = H or OMe), and [(cymene)Ru(bpy-COO$^-$)(OH$_2$)]$^{2+}$ have similar acidity to **2-OH$_2$**, with pK_a values in the range of 7 - 10.[20,27,28] This confirms that the d^6 Ir(III) center is ligated by water, and that the aqua complex will be dominant below pH 7

The concentration of Ir and Ru was determined by inductively coupled plasma-mass spectrometry (ICP-MS), providing a molar extinction coefficient for **2-OH$_2$** at λ_{max}(410 nm) of 1800 M^{-1} cm^{-1}; the extinction coefficient of **4** was also determined at λ_{max}(415 nm) to be 1200 M^{-1} cm^{-1}.
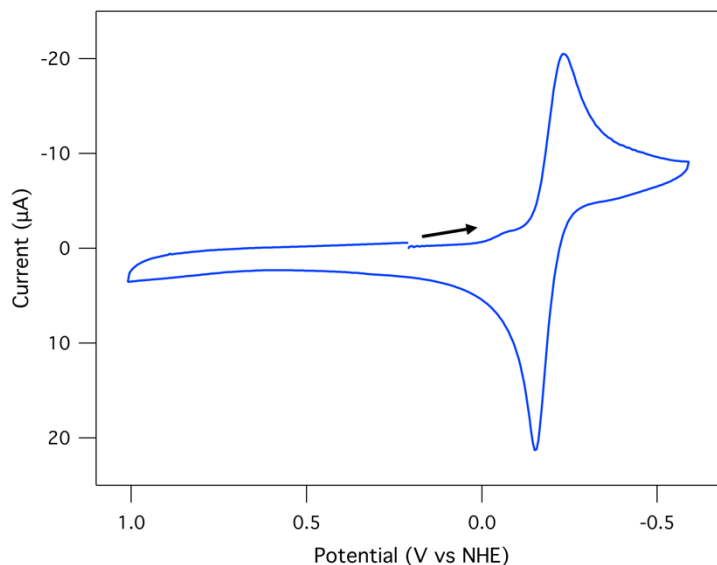
Figure 2.3. Cyclic voltammetry of **2-OH₂** in 0.1 M sodium phosphate adjusted to pH 5 with a glassy carbon working electrode, Ag/AgCl reference electrode, and a platinum wire counter electrode. Scan rate is 100 mV s⁻¹. Arrow shows direction of scan.

The reduction potential of **2-OH₂** was determined using cyclic voltammetry (CV), as shown in Figure 2.3 in pH 5 phosphate buffer. The reduction feature, $E_{1/2} = -0.19$ V vs NHE, was assigned as a quasi-reversible two-electron reduction on the basis of the narrow peak-to-peak separation ($\Delta E_p = 49$ mV). A Randles-Sevcik plot showed a linear dependence of peak current on the square root of the scan rate, indicating a diffusion-limited reduction.

To confirm that the reduction is a 2e⁻ process, controlled potential electrolysis of **2-OH₂** was conducted in pH 7 phosphate buffer at –0.54 V vs NHE. During electrolysis, current equivalent to 1.6e⁻ per complex was passed as the dark green solution turned a dark maroon color (see experimental section for additional details). ¹H NMR spectra of the electrolyzed solution showed diagnostic resonances for [Cp*Ir(μ-bpm)Ru(bpy)₂]²⁺ (**3**) while UV-Vis spectra contained characteristic structured bands between 600-900 nm consistent with **3**. The pK_a of **2-**

22

OH₂ indicates that an aqua ligand will be present under the experimental conditions, such that the reduction potential corresponds to the 2e⁻ reduction of aqua complex **2-OH₂** to the reduced species **3** (which is not ligated by water). The standard reduction potential of **2-OH₂** is the same as [Cp*Ir(OH)(bpy-COO)]⁻,[20] and occurs at potentials less negative than expected for a Ru polypyridine-based reduction. Additional features at –0.6 V and –1 V vs NHE are tentatively assigned to Ru-polypyridine-based reductions (Figure 2.4)
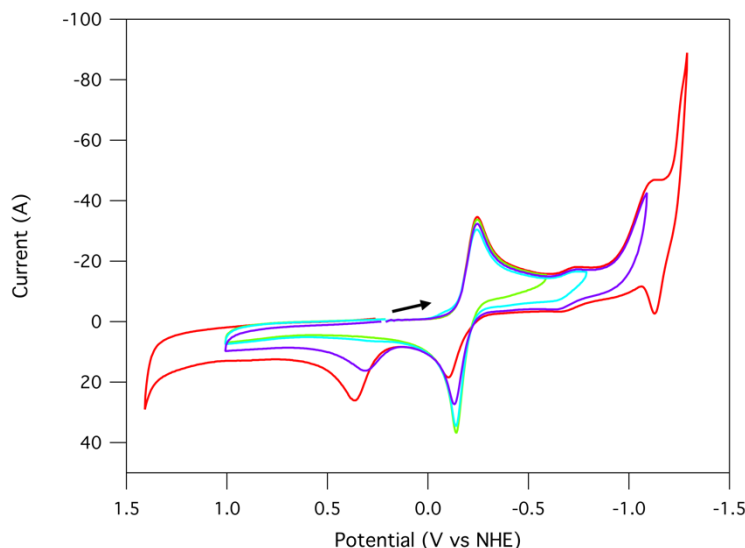
Figure 2.4. Cyclic voltammogram of **2-OH₂** in 0.1 M sodium phosphate adjusted to pH 5 using a glassy carbon working electrode, Ag/AgCl reference electrode, and Pt wire counter electrode. Different colored traces represent varying switching potentials. Scan rate is 250 mV s⁻¹. Arrow shows direction of scan.

2.2.2 Characterization of reduced species 3.

We set out to independently synthesize the reduced complex **3**, which had only been characterized by ¹H and ¹³C NMR spectroscopy and was implicated as an intermediate in the catalytic four electron reduction of O_2.[2] A biphasic reaction mixture containing the dark green aqua complex **2-OH₂** and formate in a pH 5 aqueous layer above a colorless CH_2Cl_2 organic

layer was stirred for 4 hours. Over the course of the reaction, the CH_2Cl_2 layer took on maroon

color (Scheme 2.2). Isolation of the organic layer provided pure **3** in 75% yield. The ^{1}H NMR

spectrum of **3** shows the anticipated increase in symmetry that would be accompanied by a

geometric rearrangement around iridium that places the bipyrimidine ring perpendicular to the

Cp* ring. Along with the change in symmetry, a dramatic upfield shift of the bipyrimidine

resonances to δ 6.0 is diagnostic of formation of **3**.

Scheme 2.2. Synthesis of 3 from 2-OH$_2$.
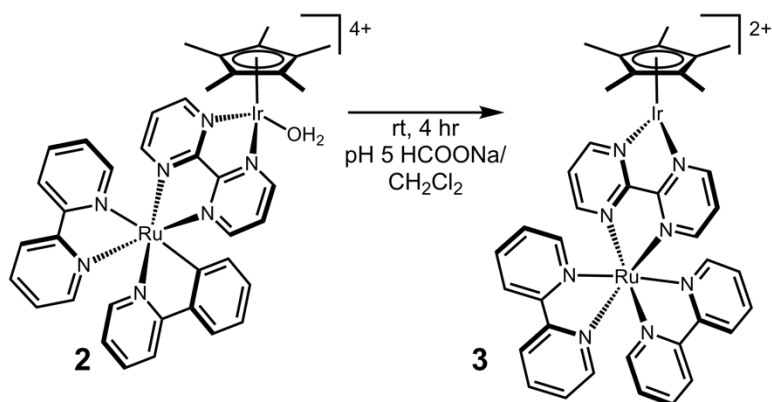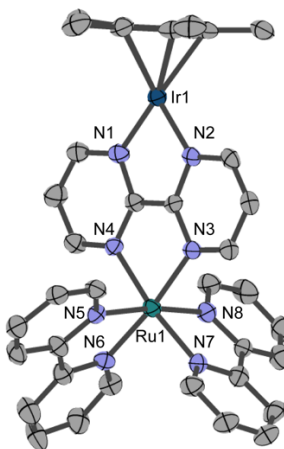
Figure 2.5. Structural representation of **3** with ellipsoids drawn at the 50% probability level. The asymmetric unit contains another molecule of **3** and four triflate ions that are not shown, along with Et$_2$O and CH$_3$CN solvent. Hydrogen atoms omitted for clarity. Selected distances (Å): Ir1−N1 1.998(6), Ir1−N2 1.989(6), Ru1−N3 2.089(6), Ru1−N4 2.081(6), Ru1−N5 2.061(6), Ru1−N6 2.052(6), Ru1−N7 2.050(6), Ru1−N8 2.056(6).

Table 2.1. Summary of crystal data, data collection parameters, and structure refinement for **3**.

Empirical formula	$C_{88}H_{90}F_{12}Ir_2N_{18}O_{13}Ru_2S_4$
Formula weight	2550.55
Temperature/K	100
Crystal system	monoclinic
Space group	$P2_1/c$
a/Å	20.0146(7)
b/Å	20.9174(8)
c/Å	23.3149(9)
$\alpha/°$	90
$\beta/°$	103.633(2)
$\gamma/°$	90
Volume/Å^3	9485.9(6)
Z	4
$\rho_{calc}g/cm^3$	1.786
μ/mm^{-1}	9.475
F(000)	5048.0
Crystal size/mm^3	$0.214 \times 0.053 \times 0.042$
Radiation	CuKα ($\lambda = 1.54178$)
2Θ range for data collection/°	4.542 to 140.382
Index ranges	$-23 \leq h \leq 24, -25 \leq k \leq 25, -24 \leq l \leq 27$
Reflections collected	101444
Independent reflections	17696 [$R_{int} = 0.0695, R_{sigma} = 0.0532$]

Purple crystalline needles suitable for X-ray diffraction were grown by vapor diffusion of diethyl ether into an acetonitrile solution of **3**. The molecular structure is pseudo-C_2 symmetric, with a C_2 plane of symmetry bisecting the C-C bond of bipyrimidine consistent with other low valent Cp*M(bpy) complexes (Figure 2.5).[29–31]

The absorption spectrum of **3** features a structured band in the long wavelength region of the UV-vis spectrum (Figure 2.6A) attributed to partial diimine ligand reduction.[32,33,34] These broad structured absorbance features are common among reduced polypyridyl Ru and Ir complexes.[10,20,32,35–37] To probe the electronic structure of this reduced catalytic intermediate,

Density Dunctional Theory (DFT) and Time-Dependent Density Functional Theory (TD-DFT) calculations were performed on **3**.

The singlet ground state (S$_0$) structure of **3** was optimized using the PBE, M06, and B3LYP functionals (LANL2DZ ECP basis set for Ir and Ru and 6-31G* for all other atoms), modeling water solvation with a polarized continuum model (PCM). A high degree of delocalization is observed in the HOMO, LUMO, and LUMO+2 orbitals (Figure 2.6B). The extensive orbital mixing of the LUMO is consistent with delocalization of the reduction across both the metal and ligand, somewhere intermediate between the formal extremes of Ir^I(bpm) and Ir^{II}(bpm$^{\bullet-}$).[32]
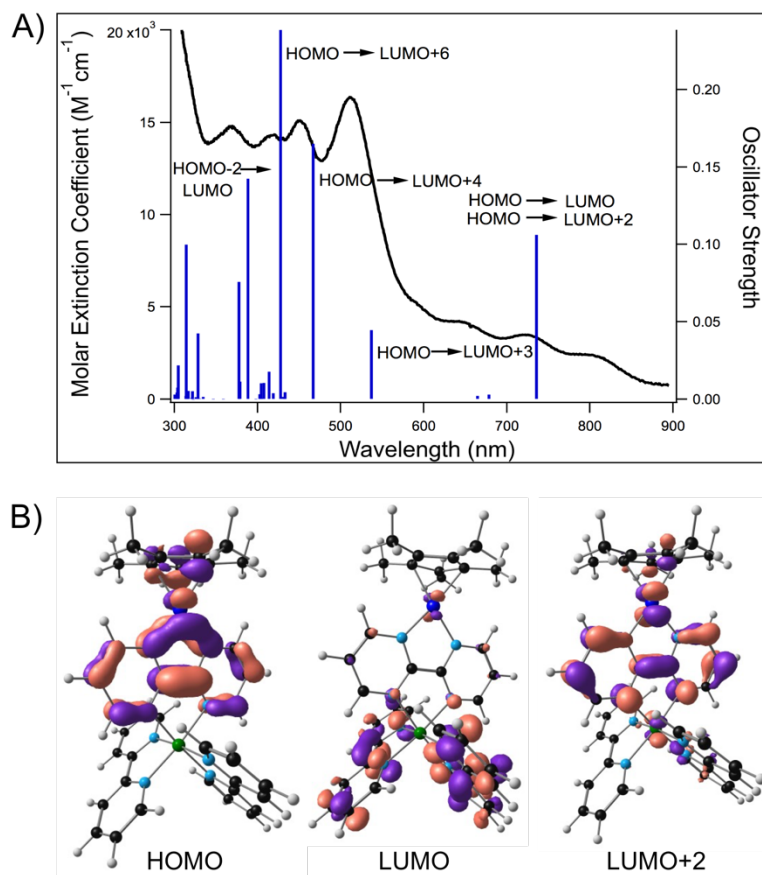
Figure 2.6. A) Experimental UV-Vis spectrum (black line) and calculated (PBE functional) excitations (blue lines) from **3** with described orbital involvement. B) Orbitals involved in lowest energy transition at 735 nm.

From the optimized ground state geometry, the absorption properties and excited states in water were explored by TD-DFT. The first 50 excitations of **3** were calculated using the same three hybrid functionals with implicit water solvation (see experimental section for comparison of all three functionals), following similar methods used to explore [Cp*M(diimine)] complexes (M = Co, Rh, Ir).[38,39] Good agreement was observed between the electronic transitions predicted by all three functionals, with the PBE functional providing the best correlation to the experimentally obtained UV-Vis spectrum (Figure 2.6A). The molecular orbitals involved in all excitations calculated using the PBE functional are outlined in the experimental section.

The transition at 735 nm is assigned to an excitation from the HOMO to a mixed state featuring LUMO and LUMO+2 character. Computational and spectroscopic studies have confirmed that monometallic Cp*Ir(bpy)-based complexes feature bipyridine-centered π–π* transitions.[38] For **3**, contributions from both the bipyrimidine and bipyridine ligands are observed. All functionals show mixed contributions from both HOMO to LUMO and HOMO to LUMO+2 (LUMO+1 is also Ru and bpy π* based).

Moving to higher energy, the transitions available to **3** at $\lambda <$ 500 nm with the highest oscillator strengths originate from either the HOMO or from Ru d-orbitals accessing the π* system of the diimine rings. The calculations indicate a high degree of orbital mixing between the iridium and ruthenium centers, supporting potential cooperative involvement between both metal centers upon photoexcitation.

2.2.3 Hydricity determination of 1 in water.

The conjugate acid of complex **3**, iridium hydride **1**, was targeted via several synthetic procedures. Treatment of **2-OH₂** with formate in acidic aqueous solutions[1] led to decomposition. Reduction with NaBH₄ in acidic aqueous solutions or methanol yielded similar results. Access to the desired hydride was finally obtained by dissolution of isolated samples of the reduced complex **3** in acidic, buffered solutions (pH 2 - 3). Protonation yielded **1**, as evidenced by a diagnostic ^{1}H NMR hydride resonance (δ −11.4 in D_2O). In acetonitrile, a similar strategy was employed: protonation of **3** with protonated dimethylformamide, [HDMF][SO_3CF_3] (pK_a = 6.1 in CH_3CN),[40] yielded hydride **1** (δ −11.8 in CD_3CN) along with DMF.
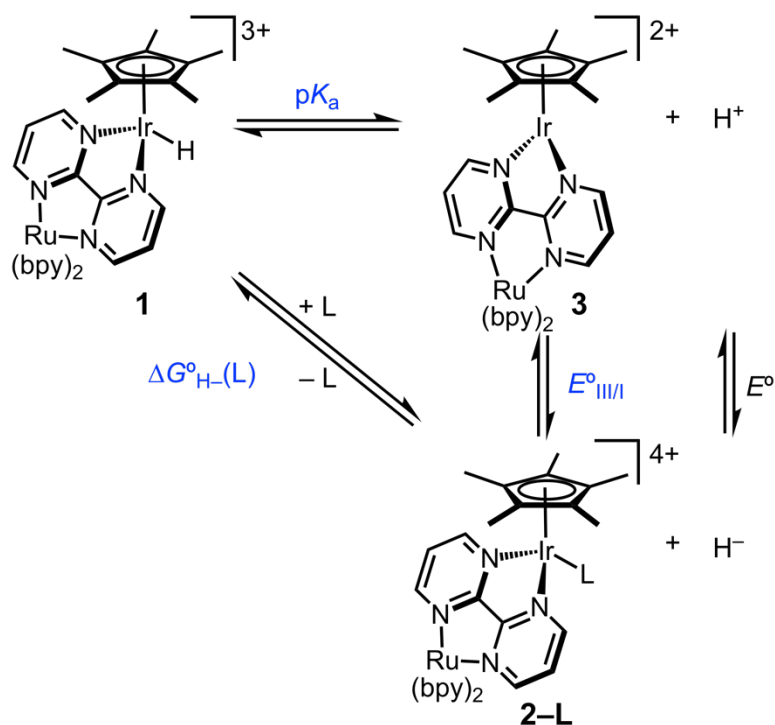
Figure 2.7. Thermochemical cycle used to determine the hydricity of **1** (L = water or acetonitrile).

To obtain the aqueous hydricity of **1**, the potential–pK_a thermochemical cycle of Figure 2.7 was employed, using the previously determined reduction potential $E^o = -0.19$ V vs. NHE. The pK_a of **1** in water was determined by spectrophotometric titration.

Initial experiments titrating conjugate base **3** with dilute triflic or phosphoric acid led to the disappearance of the features assigned to **3**, however the addition of base to the solution did not restore the original spectrum of **3**. We hypothesize that the addition of strong acid to solutions of **3** generates a high enough local pH that initially-formed **1** undergoes further irreversible protonation to generate H_2 and aqua complex **2-OH₂** (Scheme 2.3), consistent with independent reports that **1** is an intermediate in catalytic H_2 evolution activity.[1,3]

Scheme 2.3. Equilibrium protonation of **3** followed by hydrogen production by **1** to form **2-OH₂** irreversibly.
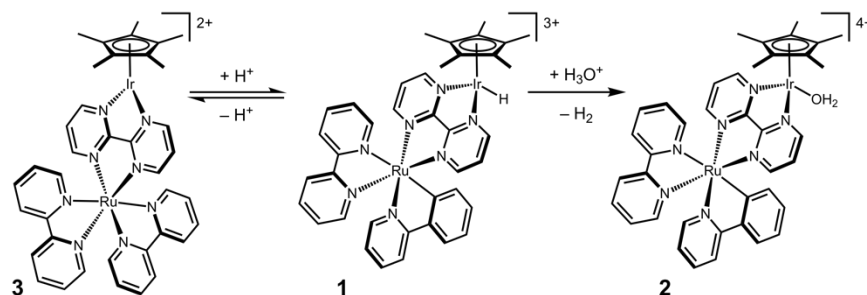
To avoid over-protonation, the titration was performed by dissolving **3** in acidic solutions (pH 2 - 3), then titrating the formed mixture of hydride and conjugate base (confirmed by ^{1}H NMR spectroscopy) with NaOH. A representative titration adding hydroxide to a pH 2.6 starting solution is shown in Figure 2.8. Fitting the absorbance at three wavelengths (511, 720, 800 nm) from titrations beginning at pH 2.5 and pH 3 gave an average pK_a of 3.1 ± 0.2. (Figure 2.8, inset). This value is slightly lower than the pK_a of 3.9 reported by Fukuzumi *et al.* for the sulfate salt.[1]
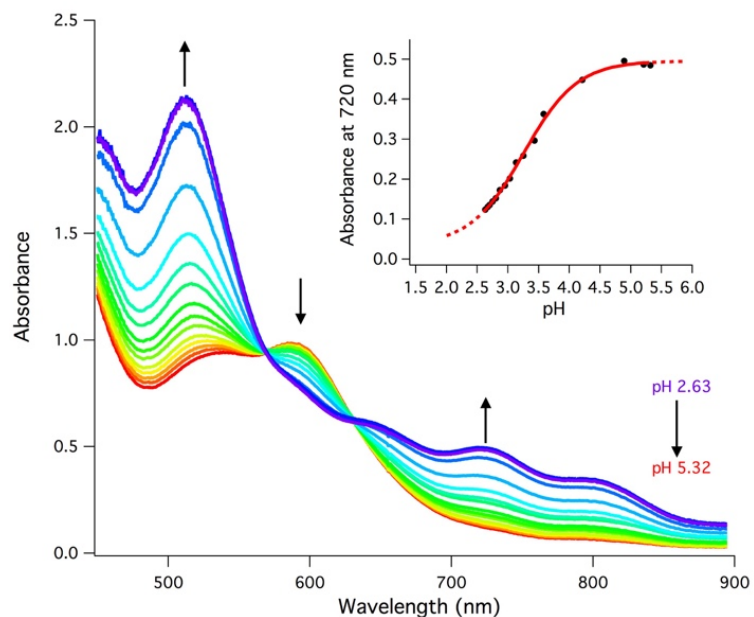
Figure 2.8. Spectrophotometric titration of **1** with NaOH to form **3**. Inset shows fitting of the absorbance at 720 nm to the Henderson-Hasselbalch equation.

Hydride complex **1** is surprisingly acidic for a transition metal complex.[41,42] Whereas the aqua complex **2-OH₂** has a pK_a value similar to the monometallic species [Cp*Ir(bpy-COO)(OH₂)], hydride **1** is 9 orders of magnitude more acidic than the corresponding monometallic hydride [Cp*Ir(bpy-COO)(H)]⁻ (Table 2.2).

Table 2.2. Comparison of thermochemical parameters of [Cp*Ir(bpy-COO)]$^{2-}$ and [Cp*Ir(μ-bpm)Ru(bpy)$_2$]$^{2+}$.

	[Cp*Ir(μ–bpm)Ru(bpy)$_2$]$^{2+}$	[Cp*Ir(bpy-COO)]$^{2-,a}$
E^o (V vs NHE) [M^{III}(OH$_2$)] + 2e$^-$ $\leftrightarrows$ [M^I] + H$_2$O	–0.19	–0.19
pK_a of aqua [M^{III}(OH$_2$)] $\leftrightarrows$ [M^{III}(OH)] + H$^+$	7.0	7.6
pK_a of hydride [M^{III}(H)] $\leftrightarrows$ [M^I] + H$^+$	3.1	12.4
ΔG^o_{H-} (kcal mol^{-1}) [M^{III}(H)] $\leftrightarrows$ [M^{III}(OH$_2$)] + H$^-$	29.7	32.0

[a]ref 20

Complex **1** is among the most acidic metal hydrides reported in water, with a pK_a comparable to Mo, Re, and W carbonyl hydrides.[12,43,44] We attribute the dramatic increase in acidity of the hydride, but not the aqua (relative to monometallic species), to formation of a highly stabilized conjugate base. As described above, DFT calculations suggest that electron density in the reduced complex **3** can be stabilized by delocalization through the bipyrimidine and bipyridine π systems.

The thermodynamic hydricity of **1** in water can be calculated based on the reduction potential and acidity data described above. Utilizing eq. 1-4, which employs a newly standardized value for the reduction of H$^+$ to H$^-$,[12,24] the aqueous hydricity of **1** was determined to be ΔG^o_{H-}(H$_2$O) = 29.7 kcal mol^{-1}. This hydricity represents the free energy of hydride release, and in water includes thermodynamic consideration for the addition of water as a ligand following hydride transfer (denoted by the parenthetical H$_2$O in the free energy expression). Hydride **1** is a stronger hydride donor (smaller ΔG^o_{H-}(H$_2$O) value) than the monometallic hydride [Cp*Ir(bpy)(H)]$^+$ (ΔG^o_{H-}(H$_2$O) = 31.5 kcal mol^{-1}), despite being tricationic.

Scheme 2.4. Relevant thermochemical values of proposed catalytic intermediates.
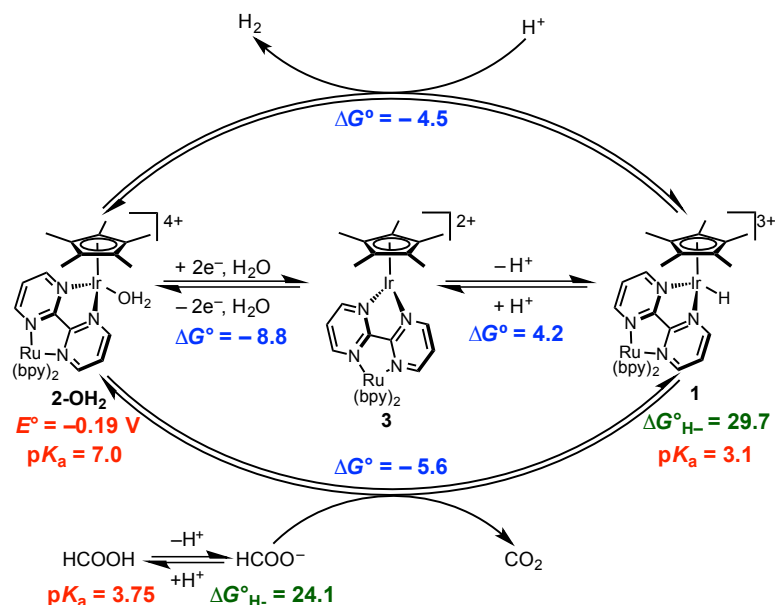
2.2.4 Relating Thermochemistry to Catalysis.

Proposed intermediates in H_2 evolution catalysis are depicted in Scheme 2.4 along with our newly collected thermochemical data. In Scheme 2.4, hydricities are shown in green, measured acidities and reduction potentials are shown in red, and the free energies at standard state conditions for the transformations depicted are shown in blue. Each step of a formic acid dehydrogenation cycle can be described thermochemically. After proton dissociation from formic acid ($pK_a = 3.75$), thermodynamically favorable hydride transfer occurs from formate to **2-OH₂** ($\Delta G = -5.6$ kcal mol^{-1}). Hydride **1** then reacts with a proton to release H_2 and regenerate **2-OH₂**. The driving force for H_2 evolution from **1** can be estimated using a thermochemical cycle based on Equations 5 - 7.[12]

$$
\begin{array}{lcr}
\mathbf{1} + H_2O \leftrightarrows \mathbf{2} + H^- & \Delta G^{\circ}_{H^-}(H_2O) \text{ of } \mathbf{1} & (5) \\
H_2 \leftrightarrows H^+ + H^- & 34.2 \text{ kcal mol}^{-1} & (6) \\
\mathbf{1} + H^+ + H_2O \leftrightarrows \mathbf{2} + H_2 & \Delta G^{\circ}_{rxn} & (7)
\end{array}
$$

Using the calculated hydricity of **1** and the accepted estimate for the heterolytic cleavage of H_2 in water (34.2 kcal/mol),[12,24] H_2 evolution is thermodynamically favorable (by 4.5 kcal mol^{-1}) at standard states (pH 0). These thermochemical predictions assume that the Ir center is ligated only by the solvent water after H_2 release. If salts or buffer components bind Ir after hydride transfer, their metal binding strengths can contribute to the overall free energy.[20] An NMR titration assessed the influence of the sulfate salts used in catalysis (see Figure 2.1). Taking into account the free energy of sulfate substitution ($\Delta G^{\circ}_{OH_2 \to SO_4} = -0.4$ kcal mol^{-1}) provides an effective hydricity of **1** to generate the sulfate complex **2-SO₄**, $\Delta G^{\circ}_{H-}(SO_4) = 29.3$ kcal mol^{-1}. As is optimal for catalysis, no intermediates in Scheme 2.4 are prohibitively high in energy or so stable as to prevent further reactivity.

The thermochemical values given in Scheme 2.4 are at the chosen standard state of pH 0, however the catalytic performance of **1** is optimal over a relatively narrow range of pH 3.5-4.5.[1,3] With the well-defined equilibrium reactions of Scheme 2.4, the concentrations of key species can be tracked as a function of pH. Below pH 3, the rate-determining step is hydride transfer from formate to form **1**. As the solution pH drops below the pK_a of formic acid, the amount of formate available for metal binding and hydride transfer diminishes. For example, at pH 2, formic acid will undergo only 2% proton dissociation, leaving little formate to drive the hydride transfer reaction towards products. A large excess of formic acid relative to the catalyst can mitigate this effect.

At higher pH (pH > 5), the large concentration of formate relative to **1** leads to the rate-determining step becoming the protonation of **1** to release H_2.[1] In the H_2 evolution step, the concentrations of **1** and **2** will be equal at pH 3.3.[12,24,45] As the pH increases, however, the equilibrium concentrations redistributes increasing the concentration of **2** relative to **1**, hindering

H$_2$ release. Furthermore, hydride **1** (pK_a = 3.1) will be deprotonated to form **3** as the pH increases, further hindering H$_2$ release. At pH 3, the system reaches an idealized balance of acidity and hydricity parameters relative to H$_2$ evolution.

Photochemical H$_2$ production in water exhibits similar behavior, with the highest quantum yield obtained at pH 3.6.[3] A balance is again required in the system between the range of hydride stability and deprotonation of ascorbic acid (pK_a = 4.0) providing ascorbate (which is responsible for quenching the excited state of [Ru(bpy)$_3$]$^{2+}$). Reductive quenching will be best at pH > 5, where ascorbate concentration is maximal, but the pK_a of the hydride (pK_a = 3.1) requires more acidic conditions. The reduced chromophore [Ru(bpy)$_3$]$^+$ is a strong reductant, capable of reducing **2-OH$_2$** to **3** (thermodynamically favorable by 25 kcal mol^{-1}).[46] Near pH 3, the bimetallic species is protonated to form hydride **1**, which releases H$_2$ in the same manner as described above.

2.2.5 Hydricity Determination in Acetonitrile.

Hydricity is most commonly determined in acetonitrile solution. To date, only a few complexes have well-defined hydricity values in both water and acetonitrile.[10,12,18–20,23,47] To better compare our thermochemical data with other metal hydrides, and to more fully develop the connection between the aqueous and acetonitrile hydricity scales, we set out to determine hydricity of **1** in acetonitrile. As with water, we chose to build a potential–pK_a thermodynamic cycle with the reduction potential of [Cp*Ir(NCCH$_3$)(μ-bpm)Ru(bpy)$_2$]$^{4+}$ (**2-MeCN)** and the pK_a of **1** in order to determine the hydricity in acetonitrile. In acetonitrile, a different constant for the reduction of H$^+$ is also used.[21]
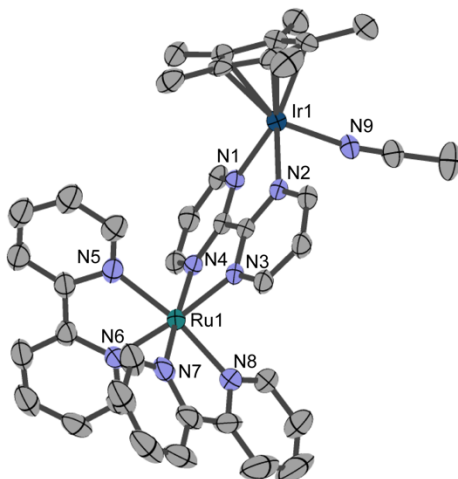
Figure 2.9. Structural representation of **2-MeCN** with ellipsoids drawn at the 50% probability level. The asymmetric unit contains four triflate ions that are not shown, along with CH_3CN and THF solvent. Hydrogen atoms omitted for clarity. Selected distances (Å): Ir1-N9 2.063(4), Ir1−N2 2.135(4), Ir1−N9 2.063(4), Ru1−N3 2.059(4), Ru1−N4 2.088(4), Ru1−N5 2.072(4), Ru1−N6 2.063(4), Ru1−N7 2.061(5), Ru1-N8 2.064(4).

Table 2.3. Summary of crystal data, data collection parameters, and structure refinement for **2-MeCN**

Empirical formula	$C_{46}H_{43}F_{12}IrN_{10}O_{12}RuS_4$
Formula weight	1577.41
Temperature/K	100
Crystal system	triclinic
Space group	P-1
a/Å	14.8260(3)
b/Å	15.0728(3)
c/Å	17.1738(4)
α/°	91.6565(12)
β/°	103.3523(11)
γ/°	119.0556(10)
Volume/Å^3	3218.93(12)
Z	2
ρ_{calc}g/cm^3	1.627
μ/mm^{-1}	7.909
F(000)	1556.0
Crystal size/mm^3	0.324 × 0.163 × 0.092
Radiation	CuKα (λ = 1.54178)
2Θ range for data collection/°	5.362 to 133.18
Index ranges	-17 ≤ h ≤ 17, -17 ≤ k ≤ 17, -20 ≤ l ≤ 20
Reflections collected	35171
Independent reflections	11013 [R_{int} = 0.0355, R_{sigma} = 0.0340]

Upon dissolution in acetonitrile, the aqua ligand of **2-OH₂** is readily displaced to form **2-MeCN**. Large green block-shaped crystals of **2-MeCN** were grown by slow evaporation of an acetonitrile/tetrahydrofuran solution (Figure 2.9). Structural comparisons between oxidized and reduced complexes containing bipyridyl-type ligands have been used to gain insight into differences in the nature of the bipyridine based reduction.[48] Figure 2.10 compares the bond lengths in bipyrimidine between the two complexes and the contraction or elongation upon reduction.
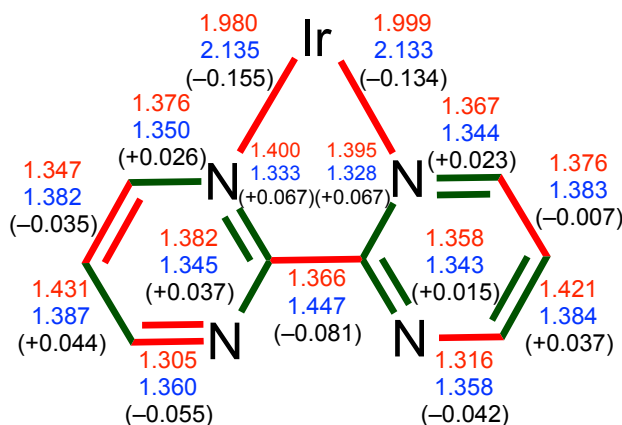
Figure 2.10. Bond length comparison between **2-MeCN** (blue) and **3** (red) with difference in length upon reduction (**black**). Bonds that contract upon reduction are shown in red and bonds that lengthen are shown in green.

We observed contracted bonds upon reduction, consistent with observations for free bipyridine[48] as well as Cp*Rh(bpy).[49,50] For unsubstituted bipyridine, the length of the bridging C–C bond between the two pyridyl rings is the best indicator of ligand reduction, with a contraction from 1.490 to 1.431 Å upon 1e⁻ reduction of the ligand. An even more dramatic contraction of 0.081 Å is seen upon reduction of **2-MeCN** to **3**. The other changes in distal bond lengths are also consistent with both Cp*Rh(bpy) and with free bipyrimidine.[48–50]
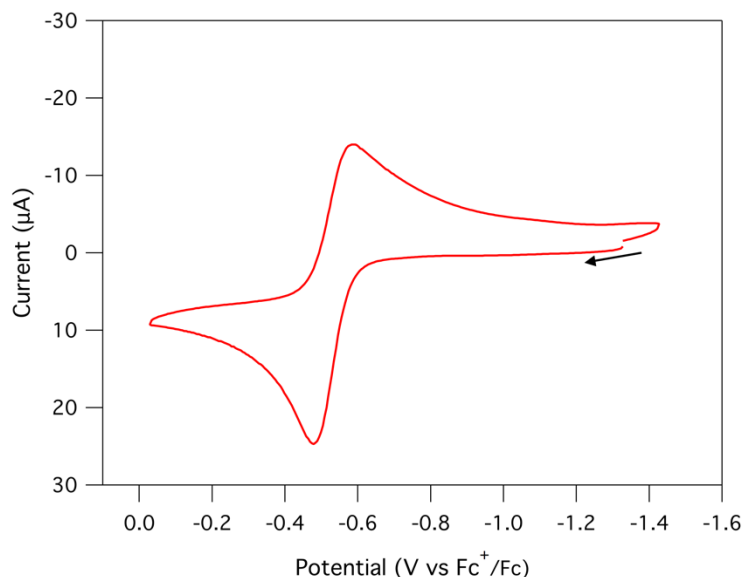
Figure 2.11. Cyclic voltammogram of **3** referenced to Fc$^+$/Fc in 0.1 M [Bu$_4$N][PF$_6$] in acetonitrile using a glassy carbon working electrode, Ag/Ag$^+$ pseudo reference electrode, and a platinum wire counter electrode. Scan rate is 100 mV s^{-1}. Arrow indicates direction of scan.

Cyclic voltammetry was used to obtain the reduction potential in acetonitrile. The reduced species **3** exhibited a two-electron oxidation at −0.52 V vs Fc$^{+/0}$ in 0.1 M [Bu$_4$N][PF$_6$] in acetonitrile, with a ΔE_p of 76 mV (Figure 2.11). The pK_a of the hydride was determined using ^{1}H NMR spectroscopy. Addition of varying amounts of [HDMF][SO$_3$CF$_3$] (pK_a = 6.1 in MeCN)[40] to CD$_3$CN solutions of **3,** produced equilibrium mixtures of **3** and hydride **1**. The relative concentrations in four separate experiments with varying amounts of acid provides a calculated pK_a of 5.5 ± 0.5 (Figure 2.12).
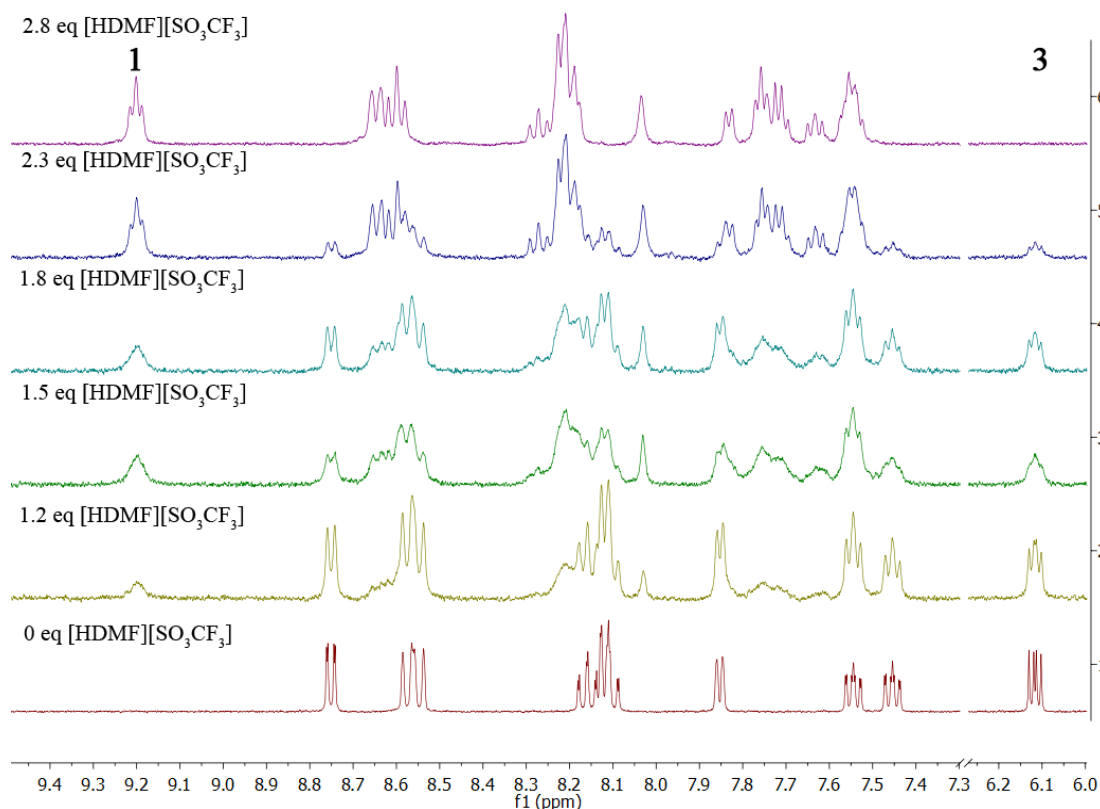
Figure 2.12. ^{1}H NMR spectra of solutions of **3** with 0-3 equivalents of [HDMF][SO₃CF₃] in CD₃CN.

*Hydride **1** is almost 20 orders of magnitude more acidic than [Cp*Ir(bpy)(H)]⁺ in MeCN (pK$_a$ = 23.3).*[10] Furthermore, the acidity of hydride **1** only changes about two pK$_a$ units upon moving from water to acetonitrile. A more typical shift for organometallic complexes is 6-8 pK$_a$ units when comparing water and acetonitrile.[43,44] Even organic compounds, typically exhibit pK$_a$ value shifts of at 5 pK$_a$ units or more.[51–53]

Examining various predictive models helps to explain the unexpectedly small solvent dependence of the pK$_a$. The pK$_a$ in MeCN is related to the pK$_a$ in H$_2$O by the solvent transfer free energies of each species, as depicted in Figure 2.13 and written in eq 8.

$$pK_a(\text{MeCN}) = pK_a(\text{H}_2\text{O}) + \frac{\Delta G°_{tr(\text{H}_2\text{O}\rightarrow\text{MeCN})}(\text{H}^+)}{1.364} + \frac{\Delta G°_{tr(\text{H}_2\text{O}\rightarrow\text{MeCN})}(\mathbf{3})}{1.364} - \frac{\Delta G°_{tr(\text{H}_2\text{O}\rightarrow\text{MeCN})}(\mathbf{1})}{1.364} \qquad (8)$$
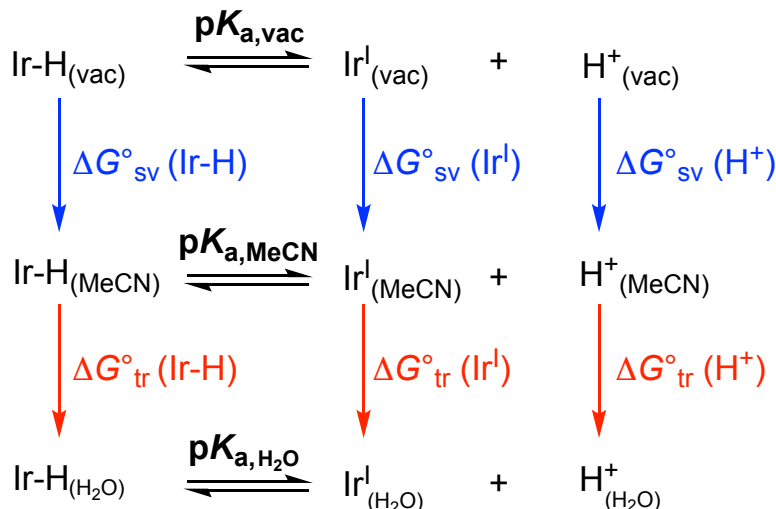
Figure 2.13. Square scheme depicting the energies necessary to determine the pK_a of an iridium hydride (Ir-H) in different solvents. The free energy of solvation ($\Delta G°_{sv}$) corresponds to the solvation of a species from the gas phase into a solvent (acetonitrile in this figure) and the free energy of transfer ($\Delta G°_{tr}$) from one solvent to another (acetonitrile to water).

Where $\Delta G°_{tr}$ is the free energy corresponding to the transfer of a species from water into acetonitrile solvent. If one assumes that the solvent transfer free energies of **1** and **3** are the same, the difference in acidity between solvents is solely dependent on the difference in solvation energy of a proton for the two solvents. Kolthoff estimated the proton acceptor ability of water to exceed that of acetonitrile by 7.7 pK_a units.[54] Using this estimate, and the average ΔpK_a for four transition metal hydride complexes[43], eq 9 was proposed to adequately approximate the change in acidity with an error of ±1 pK_a unit.

$$pK_a(\text{MeCN}) = pK_a(\text{H}_2\text{O}) + 7.5 \qquad (9)$$

For complex **1**, equation 9 overestimates the pK_a in MeCN substantially (predicted to be 10.6, found to be 5.5).

Cases where the $\Delta G°_{tr}$ terms for the hydride and its conjugate base cannot be neglected, they can be calculated by determining the solvation energies of each of the components into each solvent (Figure 2.13). The free energy of solvation, $\Delta G°_{sv}$, can be estimated semi-empirically via eq 10.

$$\Delta G°_{sv} = \frac{-N_A z^2 e^2}{4\pi\varepsilon_0 2(r + \delta_s)}\left(1 - \frac{1}{\varepsilon_r}\right) \tag{10}$$

In eq 10, N_A is Avogadro's number, z is the charge of the species being solvated, e is the charge of an electron, r is the ionic radius of the species, ε_o is the permittivity of a vacuum, ε_r is the relative permittivity of the solvent, and $\delta_s = r_s/\lambda_s$ where r_s is the ionic radius of the solvent and λ_s is the Wertheim polarization factor. Estimating the ionic radii of **1** and **3** from the average of several distances in the crystal structures of **1** and **2-MeCN**, allows $\Delta G°_{sv}$ to be calculated for each species. The energy of transfer between solvents ($\Delta G°_{tr}(H_2O{\rightarrow}MeCN)$) was then determined as the difference between $\Delta G°_{sv}$ for each solvent (Eq 11).[55] The pK_a of **1** in MeCN can then be predicted based on its pK_a in water using Eq 8.[56] This method estimates the pK_a in acetonitrile to be 8.7, still a substantial overestimate.

$$\Delta G°_{tr(H_2O{\rightarrow}MeCN)} = \Delta G°_{sv}(MeCN) - \Delta G°_{sv}(H_2O) \tag{11}$$

We finally turned to DFT to better predict the effects of solvation on **1** and **3**. Geometry optimization was performed in vacuum, with implicit water solvation, and with implicit acetonitrile solvation. The free energy of solvation ($\Delta G°_{sv}$) and the free energy of transfer from water to acetonitrile ($\Delta G°_{tr}$) were determined from the data. Using computed values of $\Delta G°_{tr}$ in equation 8 provided pK_a = 5.1 in MeCN, which is in almost perfect agreement with the experimentally determined value. At least for this system, we have demonstrated that a continuum solvation method is a better predictive model than semi-empirical calculations.

Combining the reduction potential and acidity data, and adjusting for the 2e⁻ reduction of a proton (79.6 kcal mol^{-1})[21] gives a hydricity of 63.1 kcal mol^{-1} in acetonitrile. This value is 1 kcal mol^{-1} greater than the reported hydricity for [Cp*Ir(bpy)(H)]$^+$ of 62 kcal mol^{-1}.[10] Typically transition metal hydricity correlates strongly with the reduction potential of the conjugate hydride acceptor (MeCN complex), with more negative potentials leading to strong hydride donors.[57]

Kubiak *et al.* reported a strong correlation between reduction potential and hydricity in acetonitrile.[58] The reduction potential of **2-MeCN**, suggests that bimetallic hydride **1** would be expected to be a very weak hydride donor, in the range of 68 kcal mol^{-1}. However, the pK_a of **1** is much more acidic than typical Ir hydrides, and this has an opposing effect on the hydricity (Eqs. 1 - 4). Thus, although the relevant reduction potential and pK_a values are not similar, the bimetallic and monometallic hydrides end up with very similar hydricity values. Table 2.4 highlights the thermochemical parameters measured in both solvents. It is noteworthy that hydride transfer from formate is thermodynamically much more favorable in acetonitrile (~20 kcal mol^{-1}) than in water (~5 kcal mol^{-1}). This additional driving force could lead to more efficient catalytic routes to formate dehydrogenation.

Table 2.4. Comparison of thermochemical values in acetonitrile and aqueous solvent.

	Water	Acetonitrile
$E°$ of **2**	–0.19 V vs NHE	–0.52 V vs Fc$^+$/Fc
pK_a of **1**	3.1	5.5
$\Delta G°_{H-}$ of **1** (kcal mol^{-1})	29.7	63.1

Figure 2.14 shows how experimental hydricity changes in moving from acetonitrile and water for **1** and several other complexes. All of the hydrides are more hydridic (better hydride donors, lower $\Delta G°_{H-}$) in water than in acetonitrile, due in part to the different constant for the

H$^+$/H$^-$ reduction in each solvent, which is reflected in the hydricity of H$_2$ (Figure 2.14).

However, if this was the only factor contributing to the differences in hydricities, there would be

a systematic difference of 41.8 kcal mol^{-1} for each species. The charged species released upon

hydride donation are better stabilized in water ($\varepsilon = 78.4$)[55] than in acetonitrile ($\varepsilon = 35.9$)[55] and

additional factors such as hydrogen bonding interactions can also influence the experimentally

observed difference.[47] The largest values of $\Delta\Delta G°_{H-}$ are in the range 33-35 kcal mol^{-1}, for **1**,

[HFe$_4$N(CO)$_{12}$]$^-$,[19] and [HNi(dmpe)$_2$]$^+$.[26] Two of these complexes are large multimetallic species

capable of efficient delocalization, however more detailed studies are required in order to

elucidate factors that influence the magnitude of $\Delta\Delta G°_{H-}$ between the two solvents.
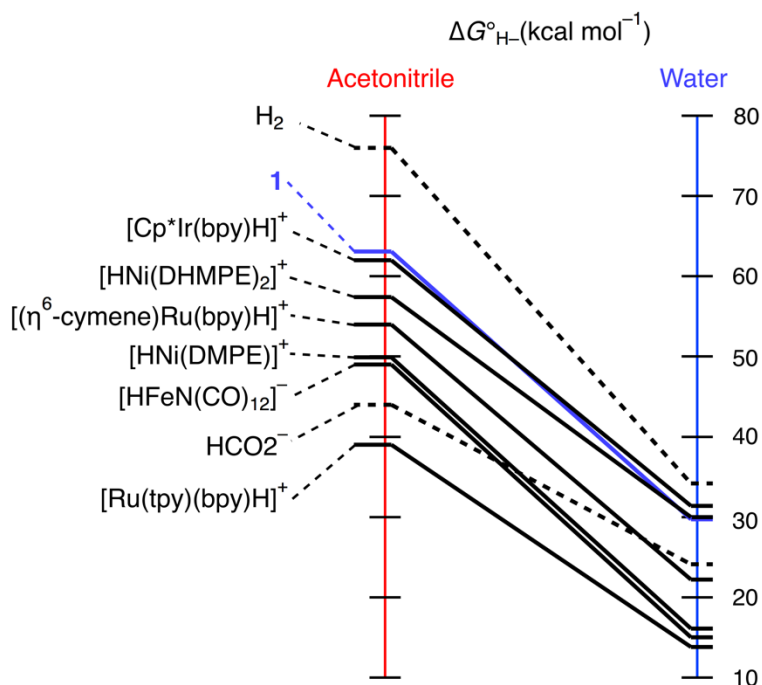
Figure 2.14. Comparison of complexes with reported hydricities in acetonitrile and water (tpy is
2,2':6',2"-terpyridine; DHMPE is 1,2-bis(bis(hydroxymethyl)-phosphino)ethane); DMPE
is 1,2-bis(dimethylphosphino)ethane).[10,18,20,23,26,47]

2.3   Conclusions

Several heterobimetallic catalytic intermediates have been isolated and characterized in solution using electrochemical methods, UV-Vis spectroscopy, and NMR spectroscopy. Complexes **2-MeCN** and **3** were structurally characterized by X-ray crystallography. The electronic structure of the reduced species **3** was investigated by DFT and TD-DFT, revealing a significant degree of metal-ligand delocalization. The stability afforded by delocalization is responsible for the surprisingly strong acidity of **1**. Solvation energies approximated using continuum solvation models in DFT calculations accurately predicted the subtle change in pK_a upon moving from water to acetonitrile.

This work includes the first reported structural, electrochemical, and thermodynamic characterization of heterobimetallic Cp*Ir/Ru complexes. The doubly-charged Ru center provides good solubility in both polar organic solvents and water, enabling the determination of hydricity using a potential–pK_a thermodynamic cycle in both water and acetonitrile. While the acidity of **1** remains relatively constant between solvents, the hydricity values are quite different in water and acetonitrile. The catalytic activity of **1** towards photochemical hydrogen evolution and formate dehydrogenation was considered in the context of the newly available thermochemical values. The large difference in the hydricity of **1** between water and acetonitrile has the potential for use as a catalytic tool to modulate hydride reactivity in different solvent environments.

2.4   Experimental and Supplementary Details

2.4.1   General Considerations.

All synthetic procedures were carried out using a nitrogen-filled glove box or a nitrogen Schlenk line unless otherwise noted. Water was thoroughly degassed with nitrogen prior to use.

Organic solvents were dried and degassed with argon using a Pure Process Technology solvent system. D_2O and CD_3CN were purchased from Cambridge Isotope Laboratories, Inc. and used as received for air-stable samples. Dissolved oxygen was removed by sparging with nitrogen (D_2O) or through three freeze–pump–thaw cycles (CD_3CN) before being stored in a glovebox. $[Cp*Ir(Cl)_2]_2$,[59] $[Ru(bpy)_2(Cl)_2]$,[60] $[Ru(bpy)_2(OH_2)_2][SO_3CF_3]_2$,[61] and $[Cp*Ir(OH_2)_3][SO_3CF_3]_2$[62] were synthesized according to literature procedures.

^{1}H NMR spectra were recorded on either a 400 or 600 MHz spectrometer at 25 °C. Chemical shifts are reported with respect to residual organic solvents[63] or a dioxane internal standard in D_2O. UV-Vis spectra were obtained with either a Cary 60 spectrophotometer or an Ocean Optics USB2000+ spectrometer with a DT-MINI-2GS deuterium/tungsten halogen light source controlled by OceanView software. Solution pH was recorded with either an OrionStar A111 pH meter with a Beckman-Coulter pH probe or a Hach PHW47-SS ISFET probe and Hach H170 portable meter.

Inductively coupled plasma-mass spectrometry (ICP-MS) using an Agilent Technologies 7500x series ICP-MS at the UNC Biomarker Mass Spectrometry Facility and was employed to determine iridium and ruthenium concentrations for UV-Vis. A calibration curve of iridium and ruthenium from 10-500 ppb was generated and used to determine the concentrations of the UV-Vis samples.

Mass spectrometry was carried out with a LTQ FT (ICR 7T) (ThermoFisher, Bremen, Germany) mass spectrometer. Samples (in H_2O/MeOH solution) were introduced via a micro-electrospray source at a flow rate of 3 µL/min. Xcalibur (ThermoFisher, Breman, Germany) was used to analyze the data. Molecular formula assignments were determined with Molecular Formula Calculator (v 1.2.3).

Single-crystal X-ray diffraction data was collected on a Bruker APEX-II CCD diffractometer at 100 K with Cu Kα radiation (λ = 1.54175 Å). The structures were solved with the olex2.solve structure solution program using charge flipping and refined with the XL refinement program using least-squares minimization. See SI section I for additional details.

2.4.2 Electrochemistry.

Electrochemical studies were performed using a Pine WaveNow potentiostat or WaveDriver bipotentiostat controlled with Aftermath software. For cyclic voltammetry, an undivided 3-electrode cell with a 3-mm diameter glassy carbon electrode that was polished between scans with 0.05-micron alumina powder was used. Controlled potential electrolysis studies were performed in a pressure-bridged divided H-cell. A reticulated vitreous carbon electrode (RVC) impaled on a graphite rod was utilized as the working electrode. For both experiments, a platinum wire counter electrode, and a Ag/AgCl (3M NaCl) reference electrode were used. All potentials are reported versus NHE by adding +0.21 V to potentials measured versus Ag/AgCl.[64]

A 1.3 mg (1.17 μmol) sample of **2-OH₂** was dissolved in 2.5 mL 0.1 M sodium phosphate electrolyte adjusted to pH 7 and transferred to one compartment of an electrochemical H-cell equipped with a reticulated vitreous carbon (RVC) working electrode, a Ag/AgCl reference electrode, and a platinum wire auxiliary electrode. Under N_2, the sample was electrolyzed at -0.54 V vs NHE for 90 minutes. During electrolysis, -174.9 mC of current was passed which corresponds to 1.55 e⁻ per molecule of complex.

2.4.3 Determination of pK_a in Water and Aceonitrile.

The spectrophotometric titration of [Cp*Ir(OH$_2$)(μ-bpm)Ru(bpy)$_2$][SO$_3$CF$_3$]$_4$ (**2-OH$_2$**) was performed starting from a solution of **2-OH$_2$** in 0.1 M phosphate buffer (pH 11.06). An initial absorbance spectrum of the complex was taken and the initial pH of the solution was recorded with a glass body pH probe. The metal complex concentration was determined by ICP-MS. Aliquots of dilute triflic acid were added, with absorbance spectra and solution pH measured after each addition. The pK_a was determined by least squares fitting of the data to the Henderson-Hasselbalch equation. After the titration, addition of dilute sodium hydroxide reformed [Cp*Ir(OH)(μ-bpm)Ru(bpy)$_2$][SO$_3$CF$_3$]$_3$, confirming that no complex decomposition had occurred. An analogous titration of **2-OH$_2$** in 0.1 M sodium triflate was consistent with the value measured in phosphate buffer, suggesting that phosphate binding does not occur to a significant extent.

Spectrophotometric titrations of [Cp*Ir(μ-bpm)Ru(bpy)$_2$][SO$_3$CF$_3$]$_2$ (**3**) were performed in a nitrogen glovebox. The complex was dissolved in 0.1 M sodium phosphate (2.5 < pH < 3.5) to form hydride [Cp*Ir(H)(μ-bpm)Ru(bpy)$_2$][SO$_3$CF$_3$]$_3$ (**1**) *in situ*. Aliquots of dilute sodium hydroxide were added, with absorbance spectra and solution pH measured after each addition. The pK_a was determined by least squares fitting of the data to the Henderson-Hasselbalch equation.

The pK_a of [Cp*Ir(H)(μ-bpm)Ru(bpy)$_2$][SO$_3$CF$_3$]$_3$ in acetonitrile was determined by NMR spectroscopy. Six different solutions of **3** were prepared in NMR tubes and to each was added varying equivalents of [HDMF][SO$_3$CF$_3$] in CD$_3$CN (Figure S13). The concentrations of **1** and **3** were determined relative to a mesitylene internal standard and used to calculate and average pK_a of 5.5 in acetonitrile.

2.4.4 Synthetic Procedures.

Synthesis of [Ru(bpy)₂(bpm)][SO₃CF₃]₂. Bipyrimidine (43 mg, 0.272 mmol) was dissolved in water (5 mL) and added to a solution of $[Ru(bpy)_2(H_2O)_2][SO_3CF_3]_2$ (200 mg, 0.268 mmol) in water (5 mL) with stirring in a 20 mL scintillation vial. The mixture was stirred at room temperature for 5 hours and a brown-orange powder was isolated *in vacuo*. Excess bipyrimidine was removed by dissolving the crude product mixture in methanol and isolating the desired solid upon addition of diethyl ether in 92% yield. ^{1}H NMR (400 MHz, D$_2$O) δ 9.07 (d, J = 5.0 Hz, 2H), 8.55 (dd, J = 8.3, 3.7 Hz, 4H), 8.22 (d, J = 6.1 Hz, 2H), 8.08 (q, J = 8.5 Hz, 4H), 7.93 (d, J = 5.6 Hz, 2H), 7.78 (d, J = 5.7 Hz, 2H), 7.58 (t, J = 5.3 Hz, 2H), 7.41 (dt, J = 18.4, 6.6 Hz, 4H).

Synthesis of [Cp*Ir(OH₂)(μ-bpm)Ru(bpy)₂][SO₃CF₃]₄ (**2-OH₂**). Based on a previous preparation in neutral water,[1] $[Cp*Ir(OH_2)_3][SO_3CF_3]_2$ (150 mg, 0.221 mmol) was dissolved in pH 2 H$_2$O adjusted with triflic acid and added to a Schlenk flask. [Ru(bpy)₂(bpm)][SO₃CF₃]₂ (192 mg, 0.221 mmol) was then added to the flask with stirring. The mixture was stirred in pH 2 H$_2$O (35 mL) for 2 hours at room temperature. A dark green crystalline solid was isolated *in vacuo* in 94% yield. Reactions run at pH > 3[62] resulted in formation of $[(Cp*Ir)_2(\mu-OH)_3][SO_3CF_3]$ and incomplete conversion to the product. ^{1}H NMR (600 MHz, D$_2$O) δ 9.49 (dd, J = 19.2, 5.6 Hz, 2H), 8.60 (dt, J = 24.1, 8.1 Hz, 6H), 8.27 (d, J = 5.6 Hz, 1H), 8.21 (t, J = 7.9 Hz, 1H), 8.19 – 8.08 (m, 3H), 8.03 (dt, J = 11.0, 5.7 Hz, 2H), 7.75 (dd, J = 32.0, 5.7 Hz, 2H), 7.62 – 7.53 (m, 2H), 7.51 – 7.39 (m, 3H) 1.79 (s, 15H). ^{13}C{^{1}H} NMR (151 MHz, D$_2$O) δ 167.15, 163.48, 163.25, 157.64, 157.46, 157.42, 157.29, 153.70, 152.59, 152.19, 151.80, 140.09, 140.02, 139.85, 139.83, 128.51, 128.45, 128.42, 128.33, 128.26, 128.16, 125.42, 125.32, 125.27, 92.00, 8.78. HRMS (ESI$^+$) *m/z* [Cp*Ir(OH)(μ-bpm)Ru(bpy)₂][Cl₂] + MeOH calcd, 1019.15; found, 1018.95.

Synthesis of [Cp*Ir(μ-bpm)Ru(bpy)₂][SO₃CF₃]₂ (**3**) Aqua complex **2-OH₂** (50 mg, 0.033 mmol) was dissolved in 2 mL water and a 5 M pH 5 formate solution (52.8 µL, 0.264 mmol) was added with stirring. Dichloromethane (4 mL) was added to the reaction mixture. The biphasic reaction mixture was stirred at room temperature for 4 hours. After color transfer from the water layer to the dichloromethane layer was observed, the bright violet organic layer was separated from the water layer. The pure product was isolated *in vacuo* in 75% yield. ^{1}H NMR (600 MHz, D₂O) δ 8.79 (d, J = 6.7 Hz, 2H), 8.48 (t, J = 8.5 Hz, 4H), 8.09 – 7.94 (m, 6H), 7.86 (d, J = 5.6 Hz, 2H), 7.32 (q, J = 7.3 Hz, 4H), 7.07 (d, J = 4.6 Hz, 2H), 6.09 (dd, J = 6.8, 4.5 Hz, 2H), 2.02 (s, 15H). ^{13}C{^{1}H} NMR (101 MHz, D₂O) δ 158.07, 157.62, 155.05, 152.61, 152.47, 148.60, 143.00, 137.96, 127.54, 127.22, 124.21, 108.49, 88.27, 9.33.

Synthesis of [Cp*Ir(H)(μ-bpm)Ru(bpy)₂][SO₃CF₃]₃ (1) The hydride was prepared *in situ* using 2.8 equivalents of [HDMF][SO₃CF₃] to protonate **3** in acetonitrile and generate [Cp*Ir(H)(μ-bpm)Ru(bpy)₂][SO₃CF₃]₃ (**1**). ^{1}H NMR (400 MHz, CD₃CN) δ 9.13 (t, J = 5.6 Hz, 2H), 8.57 (d, J = 8.4 Hz, 2H), 8.53 (t, J = 7.7 Hz, 2H), 8.20 (t, J = 8.1 Hz, 1H), 8.17 – 8.09 (m, 7H), 7.76 (d, J = 5.7 Hz, 1H), 7.68 (t, J = 5.6 Hz, 2H), 7.66 – 7.61 (m, 1H), 7.56 (t, J = 6.6 Hz, 1H), 7.47 (d, J = 6.6 Hz, 3H), 1.95 (s, 15H), −11.81 (s, 1H).

2.4.5 Computational Methods and Results.

All calculations were done using Gaussian 09[65]. Calculations of solvation energies were done through geometry optimization/frequency calculations of complexes **1** and **3** in the gas phase and using the SMD solvation model for water and acetonitrile. Calculation were done using the unrestricted B3LYP functional and the LANL2DZ[66,67] basis set for Ir and the 6-311G*

basis set for all other atoms. The absence of any negative frequencies confirmed that the calculated structures were minima for the complexes. This computational protocol was used in order to using the calculated free energy of H^+ at the same level of theory.[56]

Electronic structure calculations for complex **3** were done using a different computational protocol based on agreement with experimental UV-Vis spectra. The geometry of complex **3** was optimized using the M06, B3LYP, and PBE functionals and the LANL2DZ ECP basis set[66,67] for Ir and Ru and 6-31G* for all other atoms. Aqueous solvation was modeled using the PCM solvation model. The first 50 excitations from the optimized geometric structure of **3** were calculated with each functional. Calculations were analyzed using the Chemcraft suite with orbitals depicted with a contour value of 0.045. Table 2.5 provides the excitations using the PBE functional (see main text for comparison with experimental UV-vis spectrum and orbitals involved in lowest energy transition). Figure 2.15 and Figure 2.17 show the comparison of calculated transitions and experimental spectra using the M06 and B3LYP functionals, respectively. Figure 2.16 and Figure 2.18show the molecular orbitals involved in the lowest energy transition calculated using the M06 and B3LYP functionals, respectively.

Table 2.5. Characterizations of the excitations of **3** calculated using the PBE functional. Wavelength is reported in nm, f is the oscillator strength of the transition, 1e is the highest percentage one-electron transition, and CT describes the location of electron density in the two MOs involved in the highest percentage one-electron transition.

Transition	λ (nm)	f	1e	CT
1	736	1.1E-01	HOMO → LUMO+2	Cp* +Ir$_{d\pi}$ + bpm(π) → Ir$_{d\pi}$ +bpm(π) +Ru$_{d\pi}$
2	678	3.1E-03	HOMO → LUMO	Cp* +Ir$_{d\pi}$ + bpm(π) → Ir$_{d\pi}$ + bpy(π*)
3	665	2.1E-03	HOMO → LUMO+1	Cp* +Ir$_{d\pi}$ + bpm(π) → Ru$_{d\pi}$ + bpy(π*)
4	537	4.5E-02	HOMO → LUMO+3	Cp* +Ir$_{d\pi}$ + bpm(π) → bpm(π*)
5	467	1.7E-01	HOMO → LUMO+4	Cp* +Ir$_{d\pi}$ + bpm(π) → Ir$_{d\pi}$ + bpy(π*) + p orbitals on bpm-N
6	433	4.5E-03	HOMO-1 → LUMO+1	Ru$_{d\pi}$ → Ru$_{d\pi}$ + bpy(π*)
7	433	1.2E-03	HOMO-1 → LUMO	Ru$_{d\pi}$ → Ir$_{d\pi}$ + bpy(π*)
8	431	1.5E-03	HOMO → LUMO+5	Cp* +Ir$_{d\pi}$ + bpm(π) → bpy(π)
9	428	2.4E-01	HOMO → LUMO+6	Cp* +Ir$_{d\pi}$ + bpm(π) → Ir$_{d\pi}$ + Cp* + bpm(π*) + bpy(π*)
10	419	3.8E-03	HOMO-1 → LUMO+2	Ru$_{d\pi}$ → Ir$_{d\pi}$ +bpm(π) +Ru$_{d\pi}$ + bpy(π)
11	414	1.8E-02	HOMO-4 → LUMO+2	Ir$_{d\pi}$ + bpm(π) + Ru$_{d\pi}$ → Ir$_{d\pi}$ +bpm(π) +Ru$_{d\pi}$ + bpy(π)
12	408	1.1E-02	HOMO → LUMO+9	Cp* +Ir$_{d\pi}$ + bpm(π) → Ir$_{d\pi}$ + bpy(π*) + Ru$_{d\pi}$ + bpm(π*)
13	405	6.0E-04	HOMO → LUMO+8	Cp* +Ir$_{d\pi}$ + bpm(π) → Ir$_{d\pi}$ + bpy(π*)
14	405	1.0E-02	HOMO-1 → LUMO+2	Ru$_{d\pi}$ → Ir$_{d\pi}$ +bpm(π) +Ru$_{d\pi}$ + bpy(π)
15	403	3.2E-03	HOMO-3 → LUMO+1	Ru$_{d\pi}$ + bpy(π) → Ru$_{d\pi}$ + bpy(π*)
16	398	2.0E-04	HOMO-3 → LUMO	Ru$_{d\pi}$ + bpy(π) → Ir$_{d\pi}$ + bpy(π*)
17	388	1.4E-01	HOMO-2 → LUMO	Ir$_{d\pi}$ + Ru$_{d\pi}$ + bpy(π) → Ir$_{d\pi}$ + bpy(π*)
18	379	1.1E-02	HOMO-2 → LUMO+2	Ir$_{d\pi}$ + Ru$_{d\pi}$ + bpy(π) → Ir$_{d\pi}$ + bpm(π) +Ru$_{d\pi}$ + bpy(π)
19	378	7.6E-02	HOMO-2 → LUMO+1	Ir$_{d\pi}$ + Ru$_{d\pi}$ + bpy(π) → Ru$_{d\pi}$ + bpy(π*)

20	359	2.0E-04	HOMO-3 → LUMO+2	$Ru_{d\pi}$ + bpy(π) → $Ir_{d\pi}$ +bpm(π) +$Ru_{d\pi}$ + bpy(π)
21	347	3.0E-04	HOMO → LUMO+9	Cp* +$Ir_{d\pi}$+ bpm(π) → $Ir_{d\pi}$ + bpy(π*) + $Ru_{d\pi}$ + bpm(π*)
22	335	1.6E-03	HOMO-7 → LUMO+2	$Ir_{d\pi}$ + Cp* → $Ir_{d\pi}$ +bpm(π) +$Ru_{d\pi}$ + bpy(π)
23	331	4.0E-04	HOMO-4 → LUMO	$Ir_{d\pi}$ + bpm(π) + $Ru_{d\pi}$ → $Ir_{d\pi}$ + bpy(π*)
24	329	6.0E-04	HOMO-1 → LUMO+9	$Ru_{d\pi}$ → $Ir_{d\pi}$ + bpy(π*) + $Ru_{d\pi}$ + bpm(π*)
25	328	4.3E-02	HOMO-1 → LUMO+3	$Ru_{d\pi}$ → bpm(π*)
26	326	1.3E-03	HOMO-4 → LUMO+1	$Ir_{d\pi}$ + bpm(π) + $Ru_{d\pi}$ → $Ru_{d\pi}$ + bpy(π*)
27	322	0.0E+00	HOMO-1 → LUMO+11	$Ru_{d\pi}$ → Ru-N_{bpy} σ*
28	322	5.1E-03	HOMO-1 → LUMO+4	$Ru_{d\pi}$ → $Ir_{d\pi}$ + bpy(π*) + p orbitals on bpm-N
29	321	8.0E-04	HOMO-5 → LUMO	$Ir_{d\pi}$ + Cp* + $Ru_{d\pi}$ → $Ir_{d\pi}$ + bpy(π*)
30	317	5.3E-03	HOMO-5 → LUMO+1	$Ir_{d\pi}$ + Cp* + $Ru_{d\pi}$ → $Ru_{d\pi}$ + bpy(π*)
31	316	2.6E-03	HOMO-3 → LUMO+3	$Ru_{d\pi}$ + bpy(π) → bpm(π*)
32	314	1.0E-01	HOMO-2 → LUMO+3	$Ir_{d\pi}$ + $Ru_{d\pi}$ + bpy(π) → bpm(π*)
33	314	2.1E-03	HOMO-3 → LUMO+3	$Ru_{d\pi}$ + bpy(π) → bpm(π*)
34	305	2.2E-02	HOMO-3 → LUMO+3	$Ru_{d\pi}$ + bpy(π) → bpm(π*)
35	304	1.0E-03	HOMO-1 → LUMO+5	$Ru_{d\pi}$ → bpy(π)
36	304	7.5E-03	HOMO-3 → LUMO+4	$Ru_{d\pi}$ + bpy(π) → $Ir_{d\pi}$ + bpy(π*) + p orbitals on bpm-N
37	304	1.3E-03	HOMO-4 → LUMO+6	$Ir_{d\pi}$ + bpm(π) + $Ru_{d\pi}$ → $Ir_{d\pi}$ + Cp* + bpm(π*) + bpy(π*)
38	303	4.4E-03	HOMO-5 → LUMO+3	$Ir_{d\pi}$ + Cp* + $Ru_{d\pi}$ → bpm(π*)
39	301	2.1E-03	HOMO-6 → LUMO+2	$Ir_{d\pi}$ + p orbitals on bpy-N +Cp* → $Ir_{d\pi}$ +bpm(π) +$Ru_{d\pi}$ + bpy(π)
40	300	3.0E-03	HOMO → LUMO+14	Cp* +$Ir_{d\pi}$+ bpm(π) →
41	300	5.2E-03	HOMO-5 → LUMO+6	$Ir_{d\pi}$ + Cp* + $Ru_{d\pi}$ → $Ir_{d\pi}$ + Cp* + bpm(π*) + bpy(π*)

42	298	2.0E-04	HOMO → LUMO+11	Cp* + $Ir_{d\pi}$ + bpm(π) → Cp* + $Ir_{d\pi}$ + p orbitals on bpm-N + $Ru_{d\pi}$ + p orbitals on bpy-N
43	297	2.0E-01	HOMO-4 → LUMO+3	$Ir_{d\pi}$ + bpm(π) + $Ru_{d\pi}$ → bpm(π*)
44	297	5.0E-02	HOMO-1 → LUMO+8	$Ru_{d\pi}$ → $Ir_{d\pi}$ + bpy(π*)
45	295	4.7E-02	HOMO-1 → LUMO+7	$Ru_{d\pi}$ → $Ru_{d\pi}$ + bpy(π)
46	291	5.3E-03	HOMO-1 → LUMO+8	$Ru_{d\pi}$ → $Ir_{d\pi}$ + bpy(π*)
47	290	3.7E-02	HOMO-3 → LUMO+5	$Ru_{d\pi}$ + bpy(π) → bpy(π)
48	289	4.3E-03	HOMO-2 → LUMO+5	$Ir_{d\pi}$ + $Ru_{d\pi}$ + bpy(π) → bpy(π)
49	287	1.8E-02	HOMO-3 → LUMO+7	$Ru_{d\pi}$ + bpy(π) → $Ru_{d\pi}$ + bpy(π)
50	286	7E-03	HOMO-3 → LUMO+8	$Ru_{d\pi}$ + bpy(π) → $Ir_{d\pi}$ + bpy(π*)
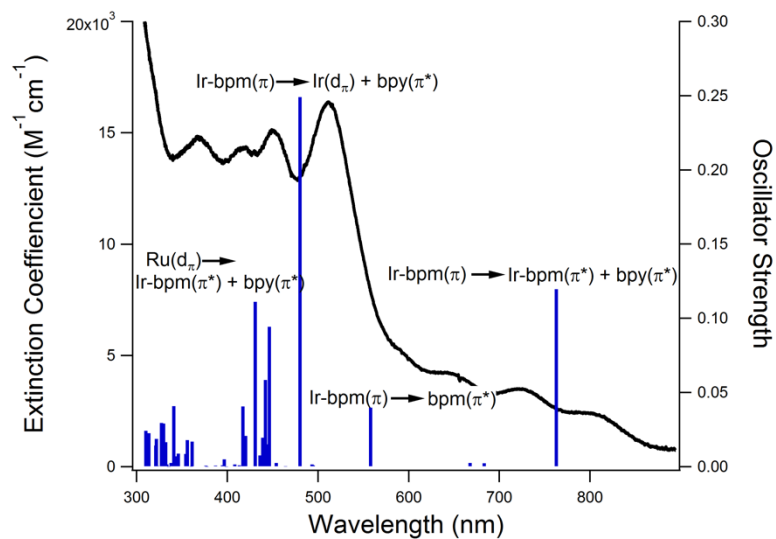
Figure 2.15. Experimental (black line) and calculated (vertical blue lines) UV-Vis spectrum using the M06 functional.
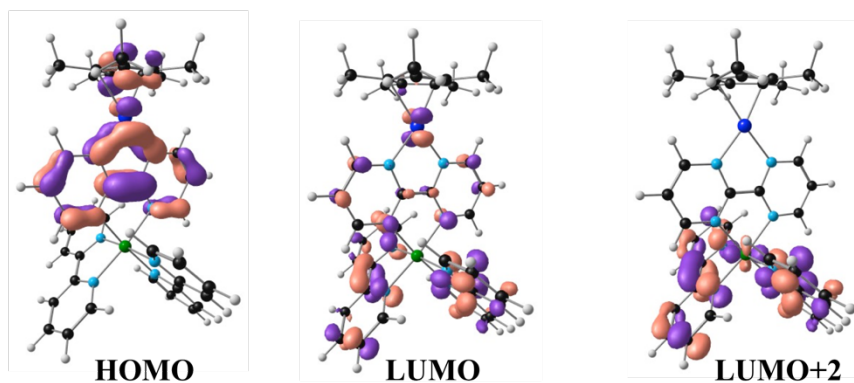
Figure 2.16. Molecular orbital depictions of the HOMO, LUMO, and LUMO+2 orbitals calculated using the M06 functional.
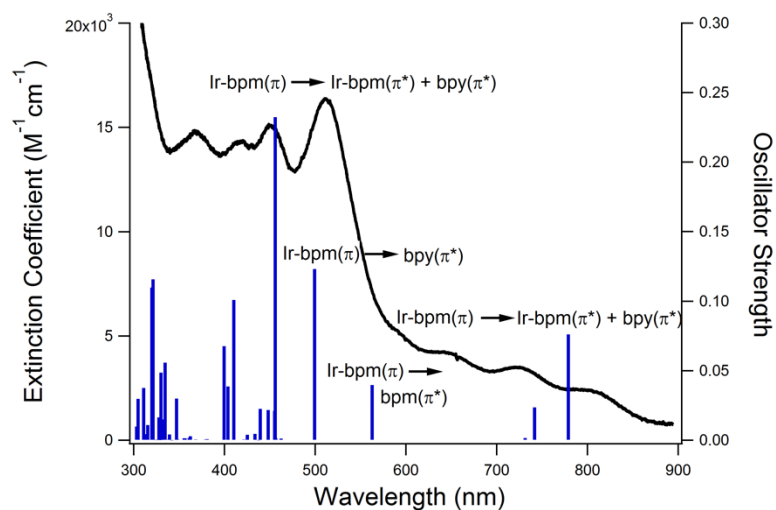
Figure 2.17. Experimental (black line) and calculated (vertical blue lines) UV-Vis spectrum using the B3LYP functional.
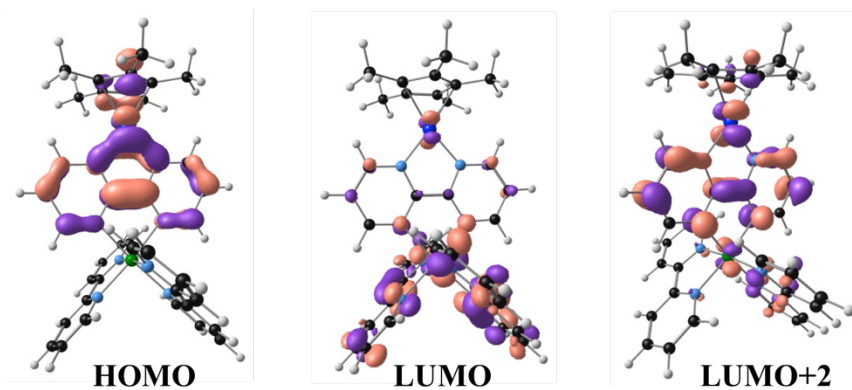
Figure 2.18. Molecular orbital depictions of the HOMO, LUMO, and LUMO+2 orbitals calculated using the B3LYP functional.

REFERENCES

(1)   Fukuzumi, S.; Kobayashi, T.; Suenobu, T. *J. Am. Chem. Soc.* **2010**, *132*, 1496–1497.

(2)   Fukuzumi, S.; Kobayashi, T.; Suenobu, T. *J. Am. Chem. Soc.* **2010**, *132*, 11866–11867.

(3)   Fukuzumi, S.; Kobayashi, T.; Suenobu, T. *Angew. Chem. Int. Ed.* **2011**, *50*, 728–731.

(4)   Kalyanasundaram, K. *Coord. Chem. Rev.* **1982**, *46*, 159–244.

(5)   Kalyanasundaram, K.; Grätzel, M. *Coord. Chem. Rev.* **1998**, *177*, 347–414.

(6)   Meyer, T. J. *Acc. Chem. Res.* **1989**, *22*, 163–170.

(7)   Juris, A.; Balzani, V.; Barigelletti, F.; Campagna, S.; Belser, P.; von Zelewsky, A. *Coord. Chem. Rev.* **1988**, *84*, 85–277.

(8)   Prier, C. K.; Rankic, D. A.; MacMillan, D. W. C. *Chem. Rev.* **2014**, *113*, 5322–5363.

(9)   Ziessel, R. *J. Am. Chem. Soc.* **1993**, *115*, 118–127.

(10)   Barrett, S. M.; Pitman, C. L.; Walden, A. G.; Miller, A. J. M. *J. Am. Chem. Soc.* **2014**, *136*, 14718–14721.

(11)   Barrett, S. M.; Slattery, S. A.; Miller, A. J. M. *ACS Catal.* **2015**, *5*, 6320–6327.

(12)   Wiedner, E. S.; Chambers, M. B.; Pitman, C. L.; Bullock, R. M.; Miller, A. J. M.; Appel, A. M. *Chem. Rev.* **2016**, *116*, 8655–8692.

(13)   Fraze, K.; Wilson, A. D.; Appel, A. M.; Rakowski DuBois, M.; DuBois, D. L. *Organometallics* **2007**, *26*, 3918–3924.

(14)   Rakowski DuBois, M.; DuBois, D. L. *Chem. Soc. Rev.* **2009**, *38*, 62–72.

(15)   Rakowski Dubois, M.; Dubois, D. L. *Acc. Chem. Res.* **2009**, *42*, 1974–1982.

(16)   Helm, M. L.; Stewart, M. P.; Bullock, R. M.; Rakowski Dubois, M.; Dubois, D. L. *Science* **2011**, *333*, 863–866.

(17)   Kang, P.; Meyer, T. J.; Brookhart, M. *Chem. Sci.* **2013**, *4*, 3497–3502.

(18)   Tsay, C.; Livesay, B. N.; Ruelas, S.; Yang, J. Y. *J. Am. Chem. Soc.* **2015**, *137*, 14114–14121.

(19)   Taheri, A.; Thompson, E. J.; Fettinger, J. C.; Berben, L. A. *ACS Catal.* **2015**, *5*, 7140–7151.

(20)   Pitman, C. L.; Brereton, K. R.; Miller, A. J. M. *J. Am. Chem. Soc.* **2016**, *138*, 2252–2260.

(21)   Berning, D. E.; Noll, B. C.; DuBois, D. L. *J. Am. Chem. Soc.* **1999**, *121*, 11432–11447.

(22)   Curtis, C. J.; Miedaner, A.; Ellis, W. W.; DuBois, D. L. *J. Am. Chem. Soc.* **2002**, *124*, 1918–1925.

(23)   Creutz, C.; Chou, M. H. *J. Am. Chem. Soc.* **2009**, *131*, 2794–2795.

(24) Connelly, S. J.; Wiedner, E. S.; Appel, A. M. *Dalton Trans.* **2015**, *44*, 5933–5938.

(25) Matsubara, Y.; Fujita, E.; Doherty, M. D.; Muckerman, J. T.; Creutz, C. *J. Am. Chem. Soc.* **2012**, *134*, 15743–15757.

(26) Connelly Robinson, S. J.; Zall, C. M.; Miller, D. L.; Linehan, J. C.; Appel, A. M. *Dalton Trans.* **2016**, *45*, 10017–10023.

(27) Ogo, S.; Kabe, R.; Hayashi, H.; Harada, R.; Fukuzumi, S. *Dalton Trans.* **2006**, 4657–4663.

(28) Liu, Z.; Habtemariam, A.; Pizarro, A. M.; Fletcher, S. A.; Kisova, A.; Vrana, O.; Salassa, L.; Bruijnincx, P. C. A.; Clarkson, G. J.; Brabec, V.; Sadler, P. J. *J. Med. Chem.* **2011**, *54*, 3011–3026.

(29) Ziessel, R.; Noblat-Chardon, S.; Deronzier, A.; Matt, D.; Toupet, L.; Balgroune, F.; Grandjean, D. *Acta Cryst* **1993**, *49*, 1–5.

(30) Mork, B. V; McMillan, A.; Yuen, H.; Tilley, T. D. *Organometallics* **2004**, *23*, 2855–2859.

(31) Nakai, H.; Jeong, K.; Matsumoto, T.; Ogo, S. *Organometallics* **2014**, *33*, 4349–4352.

(32) Ladwig, M.; Kaim, W. *J. Organomet. Chem.* **1992**, *439*, 79–90.

(33) Kaim, W.; Reinhardt, R.; Waldhör, E.; Fiedler, J. *J. Organomet. Chem.* **1996**, *524*, 195–202.

(34) Song, J. I.; Kohlmann, S.; Vogler, C.; Kaim, W. *J. Organomet. Chem.* **1991**, *411*, 207–213.

(35) Krejčik, M.; Zalis, S.; Ladwig, M.; Matheis, W.; Kaim, W. *J. Chem. Soc. Perkin Trans. 2* **1992**, 2007–2010.

(36) Kaim, W.; Ernst, S.; Kasack, V. *J. Am. Chem. Soc.* **1990**, *112*, 173–178.

(37) Zalis, S.; Krejčik, M.; Drchal, V.; Vlcek, A. A.; Zblis, S.; Drchal, M. K. V; Vleek, A. A. *Inorg. Chem.* **1995**, *34*, 6008–6014.

(38) Sieger, M.; Kaim, W.; Stufkens, D. J.; Snoeck, T. L.; Stanislav, Z. *Dalton Trans.* **2004**, 3815–3821.

(39) Hopmann, K. H. *Organometallics* **2016**, *35*, 3795–3807.

(40) Izutsu, K. *Acid-Base Dissociation Constants in Dipolar Aprotic Solvents; IUPAC Chemical Data Series*; Blackwell Science: Oxford, U.K., 1990.

(41) Morris, R. H. *J. Am. Chem. Soc.* **2014**, *136*, 1948–1959.

(42) Hu, Y.; Shaw, A. P.; Estes, D. P.; Norton, J. R. *Chem. Rev.* **2016**, *116*, 8427–8462.

(43) Dedieu, A. *Transition Metal Hydrides*; VCH Publishers: New York, 1992.

(44) Morris, R. H. *Chem. Rev.* **2016**, *116*, 8588–8654.

(45) Brereton, K. R.; Pitman, C. L.; Cundari, T. R.; Miller, A. J. M. *Inorg. Chem.* **2016**, *55*,

12042–12051.

(46) Sutin, N.; Creutz, C. *Properties and Reactivities of the Luminescent Excited States of Polypyridine Complexes of Ruthenium(II) and Osmium(II)*; 1978.

(47) Creutz, C.; Chou, M. H.; Hou, H.; Muckerman, J. T. *Inorg. Chem.* **2010**, *49*, 9809–9822.

(48) Scarborough, C. C.; Sproules, S.; Weyhermüller, T.; Debeer, S.; Wieghardt, K. E. *Inorg. Chem.* **2011**, *50*, 12446–12462.

(49) Nakai, H.; Jeong, K.; Matsumoto, T.; Ogo, S. *Organometallics* **2014**, *33*, 4349–4352.

(50) Ogo, S.; Hayashi, H.; Uehara, K.; Fukuzumi, S. *Appl. Organomet. Chem.* **2005**, *19*, 639–643.

(51) Kaupmees, K.; Trummal, A.; Leito, I. *Croat. Chem. Acta* **2014**, *87*, 385–395.

(52) Raamat, E.; Kaupmees, K.; Ovsjannikov, G.; Trummal, A.; Kütt, A.; Saame, J.; Koppel, I.; Kaljurand, I.; Lipping, L.; Rodima, T.; Pihl, V.; Koppel, I. A.; Leito, I. *J. Phys. Org. Chem.* **2013**, *26*, 162–170.

(53) Leito, I.; Kaljurand, I.; Koppel, J.; Pihl, V.; Koppel, I.; Röschenthaler, V.; Koppel, I. A.; Kolomeitsev, A. A. *J. Org. Chem.* **2008**, *73*, 2607–2620.

(54) Kolthoff, I. M.; Chantooni, M. K.; Bhowmik, S. *J. Am. Chem. Soc.* **1968**, *90*, 23–28.

(55) Izutsu, K. *Electrochemistry in Nonaqueous Solutions*; Wiley-VCH: Weinheim, 2002.

(56) Muckerman, J. T.; Skone, J. H.; Ning, M.; Wasada-Tsutsui, Y. *Biochim. Biophys. Acta* **2013**, *1827*, 882–891.

(57) Berning, D. E.; Miedaner, A.; Curtis, C. J.; Noll, B. C.; Rakowski DuBois, M. C.; DuBois, D. L. *Organometallics* **2001**, *20*, 1832–1839.

(58) Waldie, K. M.; Ostericher, A. L.; Reineke, M. H.; Sasayama, A. F.; Kubiak, C. P. *ACS Catal.* **2018**, 1313–1324.

(59) White, C.; Yates, A.; Maitlis, P. M. *Inorg. Synth.* **2007**, *29*, 228–234.

(60) Sullivan, B. P.; Salmon, D. J.; Meyer, T. J. *Inorg. Chem.* **1978**, *17*, 3334–3341.

(61) Taher, D.; Thibault, M. E.; Di Mondo, D.; Jennings, M.; Schlaf, M. *Chem. Eur. J.* **2009**, *15*, 10132–10143.

(62) Cayemittes, S.; Poth, T.; Fernandez, M. J.; Lye, P. G.; Becker, M.; Elias, H.; Merbach, E. *Inorg. Chem.* **1999**, *38*, 4309–4316.

(63) G. R Fulmer, A. J. M. Miller, N. H. Sherden, H. E. Gottlieb, A. Nudelman, B. M. Stoltz, J. E. B. and K. I. G. *Organometallics* **2010**, *29*, 2176–2179.

(64) Smith, T. J.; Stevenson, K. J. In *Handbook of Electrochemistry*; Zoski, C. G., Ed.; Elsevier: Amsterdam; p 75.

(65) Frisch, M. J.; Trucks, G. W.; Schlegel, H. B.; Scuseria, G. E.; Robb, M. A.; Cheeseman, J. R.; Scalmani, G.; Barone, V.; Mennucci, B.; Petersson, G. A.; Nakatsuji, H.; Caricato, M.;

Li, X.; Hratchian, H. P.; Izmaylov, A. F.; Bloino, J.; Zheng, G.; Sonnenberg, J. L.; Hada, M.; Ehara, M.; Toyota, K.; Fukuda, R.; Hasegawa, J.; Ishida, M.; Nakajima, T.; Honda, Y.; Kitao, O.; Nakai, H.; Vreven, T.; Montgomery, J. A., J.; Peralta, J. E.; Ogliaro, F.; Bearpark, M.; Heyd, J. J.; Brothers, E.; Kudin, K. N.; Staroverov, V. N.; Kobayashi, R.; Normand, J.; Raghavachari, K.; Rendell, A.; Burant, J. C.; Iyengar, S. S.; Tomasi, J.; Cossi, M.; Rega, N.; Millam, J. M.; Klene, M.; Knox, J. E.; Cross, J. B.; Bakken, V.; Adamo, C.; Jaramillo, J.; Gomperts, R.; Stratmann, R. E.; Yazyev, O.; Austin, A. J.; Cammi, R.; Pomelli, C.; Ochterski, J. W.; Martin, R. L.; Morokuma, K.; Zakrzewski, V. G.; Voth, G. A.; Salvador, P.; Dannenberg, J. J.; Dapprich, S.; Daniels, A. D.; Farkas, Ö.; Foresman, J. B.; Ortiz, J. V.; Cioslowski, J.; Fox, D. J. 9th ed. Gaussian, Inc.: Wallingford, CT 2009.

(66)   Schuchardt, K. L.; Elsethagen, T.; Sun, L.; Gurumoorthi, V.; Chase, J.; Li, J.; Windus, T. L. *J. Chem. Inf. Model. Inf. Model.* **2007**, *47*, 1045–1052.

(67)   Feller, D. J. *Compuational Chem.* **1996**, *17*, 1571–1586.

Chapter 3: Aqueous Hydricity from Calculations of Reduction Potential and Acidity in Water

3.1   Introduction

Thermodynamic hydricity (ΔG°_{H-}), or hydride donating ability, is the free energy required to heterolytically cleave a metal hydride bond to generate a hydride (H^-).[1–6] Transition metal hydrides are key intermediates in many catalytic transformations and, as described in Chapter 2, hydricity can be used to rationalize the reactivity of these complexes.[1,3–5,7–11] The majority of hydricity values have been determined in acetonitrile, but there is a growing interest in understanding transition metal hydricity in water.[3–6,8,12–15] The demonstrated utility of hydricity for catalyst design in acetonitrile[10,16] motivates expansion into aqueous media, where many catalytic transformations relevant to energy storage technologies occur.[17–21]

Experimental determination of aqueous hydricity is fraught with challenges relative to similar measurements in acetonitrile. For example, one can construct a pK_a – potential thermodynamic cycles[22] to determine the hydricity of a species through measurement of the acidity of the hydride and the reduction potential of its conjugate base (eq 1).

$$\Delta G^{\circ}_{H-}(M-H^+) = 1.364(pK_a) - (-46.12)(E^{\circ}_{(III/I)}) + 34.2 \tag{1}$$

However, the insolubility of the neutral conjugate base of the hydride (or other species involved) in water can inhibit electrochemical and acidity measurements.[5] Equilibria with species of known hydricity can be used to avoid these challenges by avoiding problematic intermediates, but different complexities arise. In the seminal report of Creutz and coworkers on aqueous hydricity, a series of complicated approach-to-equilibrium kinetic measurements with CO_2 were carried out to determine the needed equilibrium constants.[14,15] Equilibria with H_2 can also be used to measure a relative hydricity value, but these experiments must overcome the relative insolubility of H_2 in water (eq 2).[4]

$$[L_nM–H]^+ + H^+ \leftrightarrows [L_nM]^{2+} + H_2 \tag{2}$$

Considering the uncertainty and difficulty involved in experimental measurements in water, simple and straightforward computational methods to calculate the reduction potential and pK_a of a metal hydride would enable a more versatile and thorough understanding of the thermodynamics of the complex and would provide the hydricity value directly through eq 1. There have been a variety of computational approaches to hydricity in acetonitrile, including calculations of the free energy for heterolytic cleavage of H_2 to form the hydride complex (eq 2).[23,24] Direct calculations using an estimated value for the free energy of a solvated hydride have also been used (eq 3).[23,25]

$$[L_nM–H]^+ \leftrightarrows [L_nM]^{2+} + H^- \tag{3}$$

Finally, isodesmic reaction schemes, similar to equilibrium reaction used experimentally, can be used to avoid estimation of the energy of free H^-; these calculations are referenced to an

experimentally determined hydricity value (eq 4, where "ref–H" is a complex with a known hydricity).[26]

$$[L_nM\text{–}H]^+ + [ref]^{2+} \leftrightarrows [L_nM]^{2+} + [ref\text{–}H]^+ \tag{4}$$

In both acetonitrile and water, extensive efforts have been made to accurately calculate acidities and reduction potentials using Density Functional Theory (DFT).[26–31] However, to our knowledge, there is only one DFT calculation of aqueous hydricity (through reference to the H_2 couple, eq 2),[24] and there have been no calculations of pK_a – potential thermodynamic cycles in water despite the well-established methods for obtaining acidities and reduction potentials computationally. Capitalizing on these methods, we set out to build such cycles in order to determine aqueous hydricity.

The subjects of our study are structurally homologous iridium hydrides with well-defined hydricity values recently reported by our group[5] (complexes **1 - 7** in Figure 3.1, where the reduced form of **1** would be **1**[red], the hydride donor form is **1**[H] and the aquo acceptor is **1**[OH$_2$]), which provide direct comparisons between experimentally determined and computational hydricities. Through the development of appropriate training sets for aqueous reduction potentials and pK_a values, accurate computational models have been developed. Combining these thermodynamic parameters provides aqueous hydricity values that show good numerical agreement with experiment and also correctly predict the trend of shifting hydricity upon electronic perturbations of the bipyridine supporting ligand.
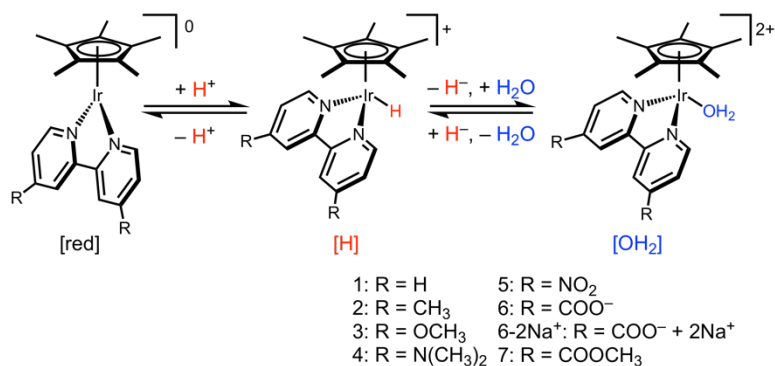
Figure 3.1. [Cp*Ir(bpy)] complexes under study. [red] refers to the 2e⁻ reduced complex, [H]
refers to the Ir–H, and [OH₂] refers to the oxidized complex which is coordinated by an aqua
ligand in aqueous solvent.

3.2 Computational Protocol

All calculations were performed using the Gaussian09[32] package. The valence basis set

LANL2DZ was used for the metal and the Pople triple-ζ basis set 6-311G* was used on

remaining atoms with use of the B3LYP, M11, or B3P86 functionals. B3LYP is a frequently

employed functional for calculations involving transition metal complexes, including reduction

potentials.[23,25,27] The M11 functional was efficiently utilized for the construction of Pourbaix

diagrams in water for ruthenium-based water oxidation catalysts.[28] The B3P86 functional was

utilized to calculate reduction potentials, acidities, and hydricities of Ni, Pt, Co, Pd, and Rh

diphosphine complexes.[26] The success of these functionals in calculations involving transition

metal redox chemistry motivated our choice to include them in the present tests.

On the basis of preliminary calculations (*vide infra*), it was deemed prudent to do all

geometry optimizations using the Solvation Model based on Density (SMD). Free energies are

reported in kcal mol⁻¹ at STP and 1 M concentrations. Reduction potentials ($E°$) were determined

from the calculated free energy of the reaction using equation 5 where *n* is the number of

electrons involved in the reduction, F is Faraday's constant (23.06 kcal V^{-1} mol^{-1}) and E° is the reduction potential versus vacuum. The potential vs. vacuum was converted to the experimentally relevant Normal Hydrogen Electrode (NHE) reference electrode by subtracting 4.28 V.[27]

$$E^{\circ} = \frac{-nF}{\Delta G^{\circ}{}_{calc}} \qquad (5)$$

Acidity was calculated according to the method of Muckerman *et. al.*[30] A training set was constructed consisting of monocationic organic acids and their conjugate bases that were optimized using the B3LYP functional and 6-311G* basis set in SMD-water. The calculated pK_a values were obtained using the literature value for the free energy of a proton in aqueous solution (-272.2 kcal mol^{-1}).[30]

3.3   Results and Discussion

3.3.1   Comparison of Computational Methods in the Reduction of an Iridium Complex.

As the 1e$^-$ reduction potential of tris(phenylpyridine)iridium(IV), [Ir(ppy)$_3$]$^+$ (**8**) is firmly established by experiment,[33] preliminary calculations using several functionals and solvation models were evaluated in order to select an appropriate method for this work. The aqueous reduction potential of complex **8** was first calculated using the B3LYP, M11, and B3P86 functionals by performing a gas-phase geometry optimization and frequency calculation, followed by a single-point energy calculation of the gas-phase optimized structure in the SMD solvent model of water. The B3LYP functional accurately reproduced the experimental potential (Table 3.1, $E^{\circ}{}_{calc} = 4.96$ V, $E^{\circ}{}_{exp} = 4.94$ V), whereas the other functionals were incorrect by 300 – 700 mV.[33]

Table 3.1. Optimal computational protocol screen for the reduction potential of complex **8** in water.
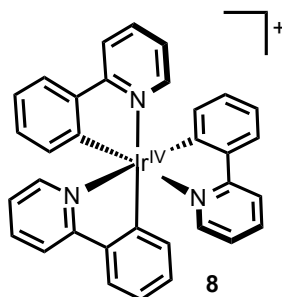
Optimization method	E° (V vs vacuum)			
	B3LYP	B3P86	M11	exp[33]
Gas phase	4.96	5.21	5.64	
SMD-water	4.96	5.31	5.59	4.94
Explicit water	5.31	5.47	5.77	

To explore the influence of optimization with an implicit solvent model on the performance of the functionals, the geometry was re-optimized in water using the SMD solvent model. For the case of complex **8** using B3LYP, the calculated reduction potential did not change, and B3LYP still best reproduces the experimental potential (Table 3.1).

The role of explicit water molecules was also probed using the B3LYP functional. Water molecules were added above and below the plane of each aromatic ligand to model potential $\pi \bullet \bullet \bullet H_2O$ interactions similar to those seen in calculations of benzene-water azeotropes.[34] The thermodynamics of water interactions in the secondary coordination sphere were explored further and these interactions are entropically unfavorable, but enthalpically favorable. Optimization of complex **8** with six explicit water molecules in conjunction the SMD-water solvent model provided $E^\circ_{calc} = 5.31$ V for the B3LYP functional, which is a greater deviation from the reported potential (Table 3.1) than calculations without explicit waters included in the model.

In summary, this preliminary screen clearly shows that optimizations using the SMD solvent model and the B3LYP functional provided the best agreement for an iridium complex that is relatively similar in structure to the iridium complexes of interest in this study.

3.3.2 Reduction Potential Correction Factor from a 1e⁻ Inorganic Training Set.

With a computational strategy in place, we set out to calculate aqueous reduction potentials. As is common in the development of a suitable training set for calculations, a series of complexes structurally similar to those of interest with known aqueous reduction potentials was first pursued. Muckerman *et al.* effectively demonstrated how the correlation between calculated and experimental values for a training set of species can be used to calculate pK_a values[30] as well as directly calculate hydricity in acetonitrile.[25] The initial training set investigated was comprised of a series of octahedral iridium and ruthenium complexes with 1e⁻ reduction potentials reported in water (Chart 3.1).

Chart 3.1. Water-soluble cyclometallated iridium complexes used as training set for calculation of reduction potentials.
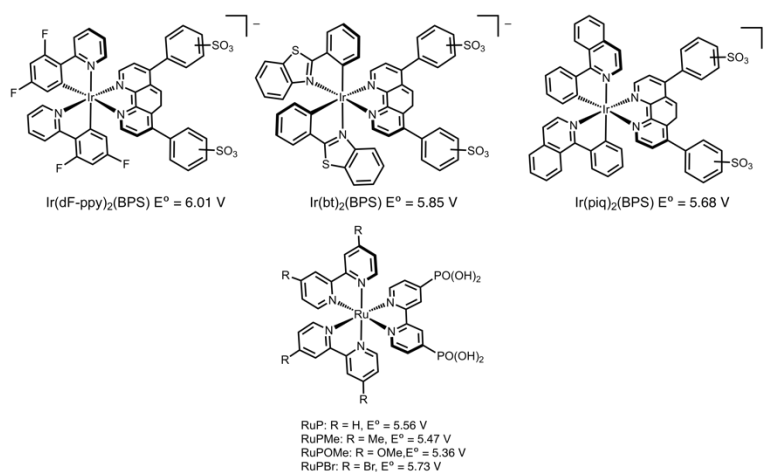
Some of the complexes in the training set contain sulfonate or phosphonate anions on the periphery of the ligand, which impart improved solubility in water and thus allow experimental

determination of reduction potentials. However, we found these substituents to complicate

computational determination of reduction potentials. Gas phase geometry optimizations yielded

structures with significant spin density on these anionic functional groups, so the computational

methods were re-investigated for this specific subset, with each complex optimized with the

SMD-water solvation model and the B3LYP, M11, and B3P86 functionals. These simulations

resulted in ~50:50 spin delocalization on the Ir^{IV} metal and the two phenylpyridine ligands only

for geometry optimizatons performed with the implicit solvation model. The Ru^{III} complexes

have the unpaired electron density almost entirely localized on the metal in all calculations.

Owing to the charge localized on the functional groups, the geometry optimization of

complexes containing sulfonate groups is greatly impacted by implicit solvation. The high polarity

of these substituents, their location on the periphery of the complexes, and the large dielectric

constant of water ($\varepsilon = 78.4$)[35] all contribute to the placement of spin density. For $Ir(dfppy)_2(BPS)$

(dfppy = 2-(2,4-difluorophenyl); BPS = bathophenanthroline disulfonate) the single-point SMD

solvation model gave $E^o_{calc} = 5.32$ V, whereas optimization using the SMD model gave $E^o_{calc} =$

5.53. The latter value is in better agreement with the experimental value of 6.02 V.[36] These results,

in conjunction with those discussed in the previous section, indicate that geometry optimization in

water is superior to gas-phase optimization in the accurate determination of the redox site of the

molecule, and should be considered essential to computational protocols for calculation of E^o and

hydricity (using eq 1).

Using the best-performing computational methods identified, reduction potentials for the

Ir and Ru complexes in the training set were calculated with implicit water solvation. The

resulting data shown in Figure 3.2 exhibits a very weak correlation between experimental and

calculated reduction potentials. This lack of correlation precludes the determination of a

correction factor derived from the linear fit of the data in Figure 3.2. This weak correlation

highlights the difficulty in determining aqueous reduction potentials for transition metal

complexes. The outliers ($\Delta G^{\circ}_{calc} \sim -127$ kcal mol^{-1}) in Figure 3.2 are both iridium and ruthenium

complexes and possess no similarities that might account for their deviation from the trend

produced by the rest of the training set. The uncertainty inherent in calculations of this type led

to the pursuit of more electrochemically similar reductions to compose the training set for the

calculation of aqueous reduction potentials.
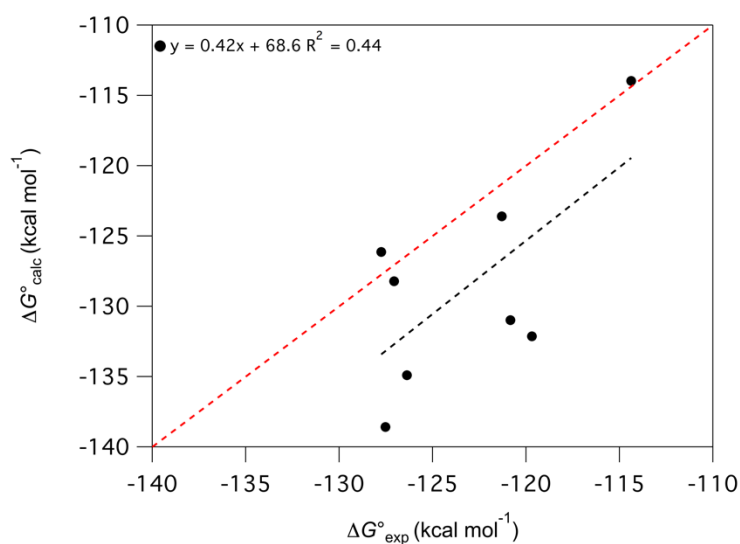
Figure 3.2. Training set of 1e$^-$ reduction potentials in water for a series of cyclometallated Ir and Ru complexes. The red dashed line represents an ideal correlation between calculated and experimental values. The black dashed line represents the best linear fit to the black data points.

3.3.3   Reduction Potentials from 2e$^-$ Organic Training Set.

The lack of correlation when pursuing a structurally homologous approach, Figure 3.2,

led us to pursue a more electrochemically homologous method. It was hypothesized that a

training set featuring 2e$^-$/2H$^+$ reduction events would better approximate the 2e$^-$ potentials of the

complexes of interest. Unfortunately, there is not a large enough set of fully reversible 2e$^-$

69

reduction potentials for transition metal complexes, even when one allows for processes with

chemical steps (EEC or ECE). Therefore, we attempted to build a 2e⁻ reduction training set using

quinone/hydroquinone potentials. Although not metal-based, the $2e^-/2H^+$ reduction of quinones

(Chart 3.2A) provides a more electrochemically similar model for the 2e⁻ reduction of complexes

1 - 7. Additionally, a large amount of accurate electrochemical data is available for structurally

similar quinones.[37] The structures and reduction potentials of the quinones chosen for the

training set are shown in Chart 3.2B.

Chart 3.2. A) $2e^-/2H^+$ reduction calculated for training set. B) Series of quinone derivatives and experimental aqueous reduction potentials (in V vs. NHE) used for training set.
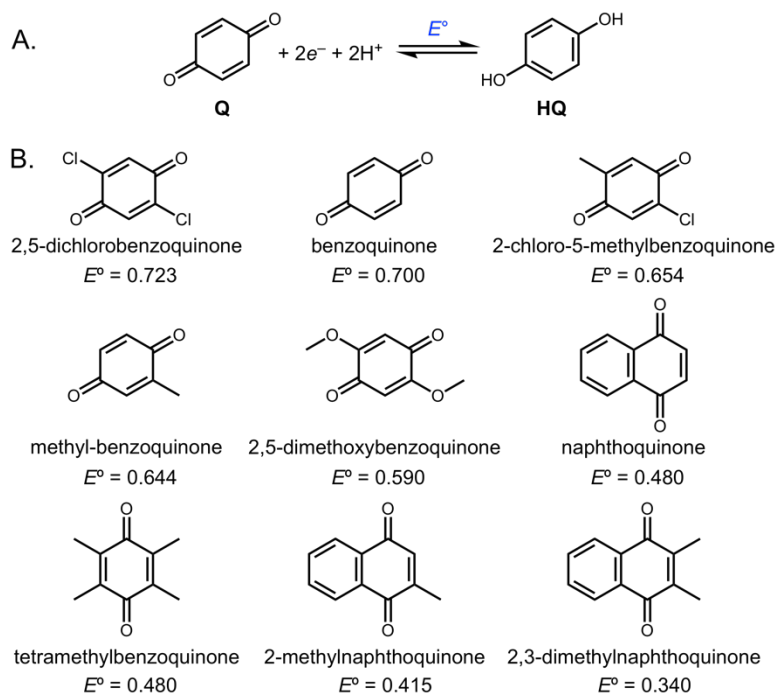
Using the B3LYP functional and optimization the implicit SMD solvation model for

water, the free energy of a modified reduction half-reaction was calculated. Equation 6 shows the

half-reaction represented by ΔG°_{calc}.

$$\Delta G^\circ_{calc} = G^\circ(\textbf{HQ}) - G^\circ(\textbf{Q}) - 2G^\circ(\text{H}^+) \tag{6}$$

In eq 6, HQ is the hydroquinone, Q is the quinone, and H^+ is the literature value for the calculated free energy of a proton in aqueous solution, -272.2 kcal mol^{-1}.[30] Equation 6 differs from a traditional reduction half-reaction because the energy of the free electrons is not considered.
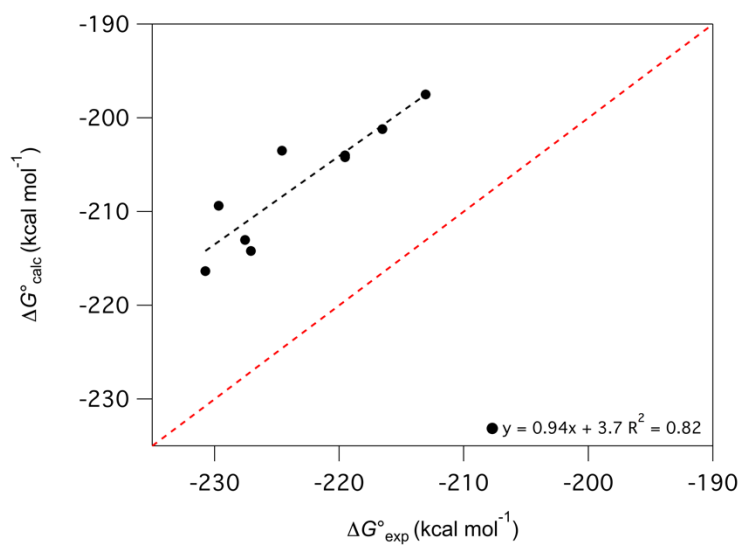
Figure 3.3. Training set of 2e$^-$ reduction potentials for a series of quinone derivatives in aqueous solution. The red dashed line represents an ideal correlation between calculated and experimental values. The black dashed line represents the best linear fit to the black data points.

Figure 3.3 compares the calculated free energy from eq 6 with the experimental values for the quinone 2e$^-$/2H$^+$ reduction training set. The correlation between calculated and experimental free energies of reduction in Figure 3.3 shows a dramatic improvement upon the training set utilizing the 1e$^-$ reduction of transition metal complexes (Figure 3.2). A linear fit of the data revealed a slope close to 1, suggesting that a systematic linear correction would be unnecessary.

Another way to investigate the manner in which the calculated reduction potential differs from experiment across the training set involves plotting the deviation from experiment (ΔG°_{corr}, eq 7) versus the experimental free energy (ΔG°_{exp}) (Figure 3.4).

$$\Delta G^{\circ}_{corr} = \Delta G^{\circ}_{calc} - \Delta G^{\circ}_{exp} \tag{7}$$

The horizontal line with a non-zero intercept of Figure 3.4 suggests that the deviation between experimental and calculated values is off by a constant value. To mitigate this difference between theory and experiment, the calculated reduction potentials can be corrected by adding the y intercept of Figure 3.4 to the calculated free energy. Because the line is not perfectly horizontal, however, the significant extrapolation needed to reach the intercept can introduce substantial uncertainty. An alternative strategy would assume a slope of 0 for the linear fit in Figure 3.4 and add the average value of ΔG°_{corr} across the range of potentials in the training set. We selected the method of extrapolation based on the experimental iridium potential available (*vide infra*). The quinone-based training set demonstrated that the computational method and implicit solvation model is satisfactory for the calculation of reduction potentials.
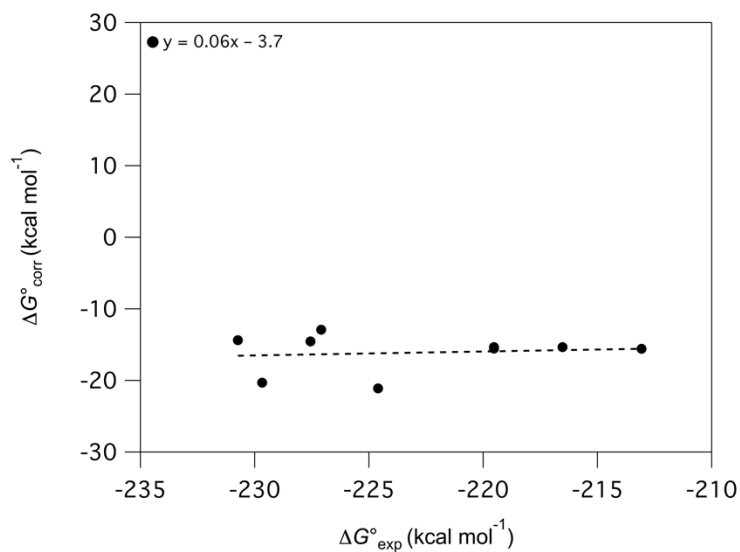
Figure 3.4. $\Delta G°_{corr}$ vs $\Delta G°_{exp}$ for the training set of quinones in water.

3.3.4 Calculation of Reduction Potentials for Cp*Ir(bpy) complexes.

The reduction potential needed for the calculation of $\Delta G°_{H-}(H_2O)$ is shown in Scheme 3.1. Two-electron reduction calculated for the determination of aqueous hydricity. The Cp*Ir complexes undergo a $2e^-$ reduction with dissociation of H_2O.

Scheme 3.1. Two-electron reduction calculated for the determination of aqueous hydricity.
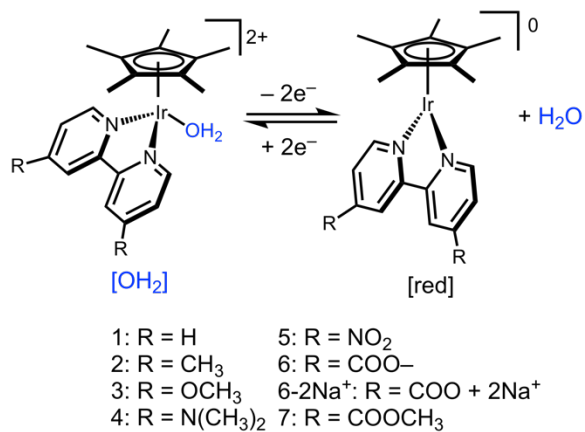
The free energy of the reaction shown in Scheme 3.1 was calculated according to eq 8 using the computational methods described above.

$$\Delta G°_{rxn} = G°_{red} + G°_{OH_2} - G°_{H_2O} \tag{8}$$

In eq 8, $G°_{red}$ corresponds to the calculated energy of the reduced species (**1**[red] in Scheme 3.1), $G°_{OH_2}$ corresponds to the energy of the oxidized complex (**1**[OH₂] in Scheme 3.1), and $G°_{H_2O}$ is the calculated energy for a water molecule at this level of theory. From the calculated free energies, the reduction potential ($E°_{corr}$, Table 3.1) was obtained using the extrapolation method of correction, which agreed best with the experimentally determined potential of **6**[OH₂] ($E°_{exp} = -0.62$ V vs. NHE).

Table 3.2. Calculated aqueous reduction potentials for complexes **1 - 7**.

species	$E°_{corr}$ (V vs. NHE)
1[OH₂]	− 0.52
2[OH₂]	− 0.53
3[OH₂]	− 0.66
4[OH₂]	− 0.86
5[OH₂]	0.16
6[OH₂]	− 0.52
6-2Na⁺[OH₂]	− 0.35
7[OH₂]	− 0.17

The complexes bearing carboxylate substituents (**6** and **6-2Na⁺**) were modeled in two different manners. Complex **6**[OH₂] was modeled as a net neutral zwitterion, without any explicit ion pairing of the carboxylate groups. Complex **6-2Na⁺**[OH₂] introduces one sodium ion per substituent to balance the charge of the carboxylate ligand, leading to an overall 2+ charge on the complex. Accurate modeling of this complex is important because it is the only species in the

series with reduction potential and pK_a values reported in water.[5] The experimentally measured reduction potential is –0.62 V vs. NHE, suggesting that complex **6**[OH$_2$] ($E°_{calc}$ = –0.52 V) is a better model than **6-2Na$^+$**[OH$_2$] ($E°_{calc}$ = –0.35 V) for the system. As a hydrogen bond donor and acceptor, water is excellent at supporting free ions in solution.
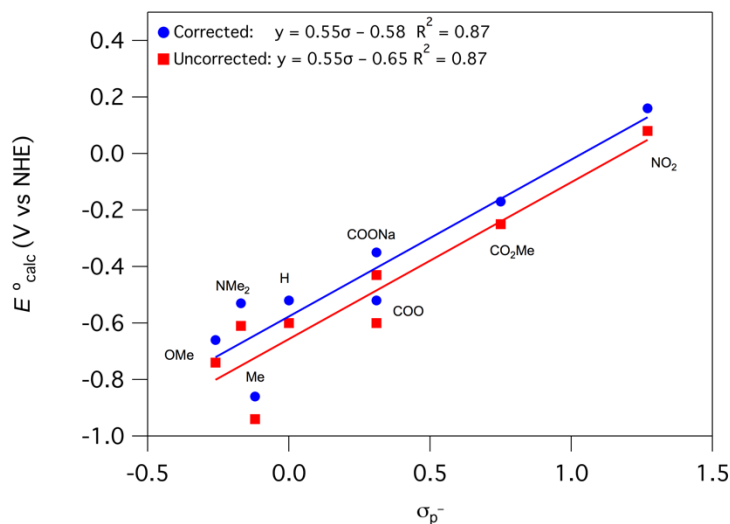
Figure 3.5. Calculated reduction potentials for complexes **1 - 7** in water (red) and potentials resulting from the application of a correction factor (blue).

Figure 3.5 shows the correlation between the uncorrected and corrected reduction potentials and the Hammett parameter, σ_p^-.[38] The σ_p^- Hammett parameter accounts for resonance stabilization of negative charges by substituents in the *para* positions, and was selected due to its excellent correlation with the experimentally measured aqueous hydricities.[5] A linear correlation with σ_p^- is observed, following the expected trend of more electron-donating ligands supporting complexes with more negative reduction potentials. The influence of ligand substitution on the measured thermodynamic parameter in a Hammett plot is defined as the slope of the linear fit (ρ).

Although comprised of organic molecules, the 2e⁻ quinone training set was found to be superior to the 1e⁻ reduction training set comprised of transition metal complexes. By using 2e⁻/2H⁺ reduction potentials, the 2e⁻ reduction potentials of complexes **1 - 7** were easily calculated and corrected using a scalar correction factor.

The acidities of iridium hydride complexes **1 - 7** were calculated using the same computational methods employed for reduction potentials and using the literature value for the energy of a proton in aqueous solution (-272.2 kcal mol^{-1}).[30] These uncorrected acidities were then corrected by application of an empirical correction factor, following the method of Muckerman.[30] For the training set (Chart 3.3B for structures), a series of organic acid/base pairs was optimized. The calculated pK_a values (Chart 3.3A) of acids in the training set showed a strong linear correlation with the experimental pK_a values, but it is also evident from Figure 3.6 that there is a systematic error leading to a slope well above unity and a large negative intercept.

Chart 3.3. A. Acidity equation for organic acid calculations. B. Training set of organic, monocationic acids for determination of acidity correction factor in water.
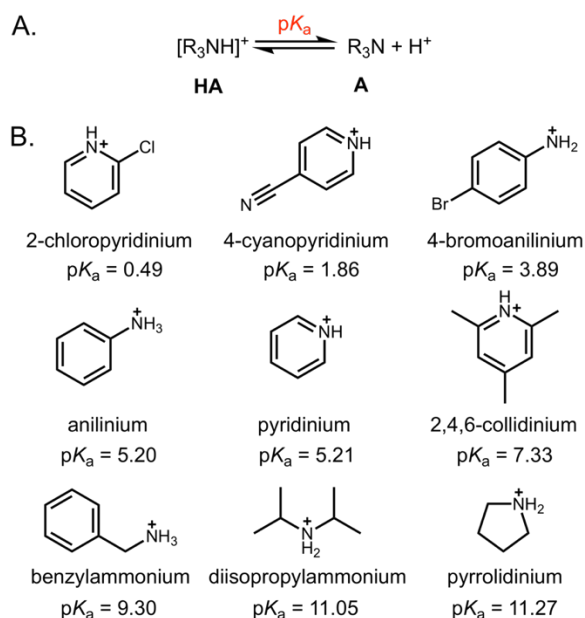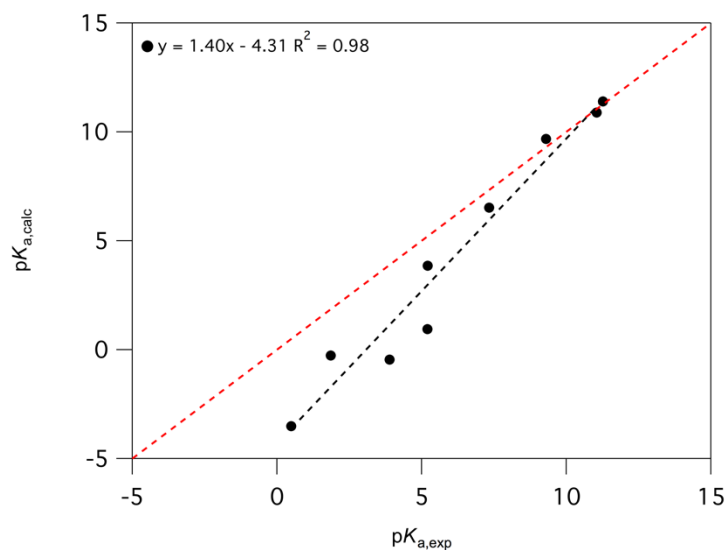
Figure 3.6. Experimental and calculated pK_a values of a training set of organic acids optimized in water with an implicit solvation model. The black dashed line represents the best linear fit to the black data points.

The deviation from the experimental pK_a values on a free energy scale (eq 7) was plotted against the experimental pK_a in order to determine the nature of the error between calculated and experimental acidities (Figure 3.7). Whereas the $\Delta G°_{corr}$ term for the 2e$^-$ reduction potentials was a horizontal line (Figure 3.4), the $\Delta G°_{corr}$ term for acidity shows a linear relationship with a negative slope. The trend is consistent with what has been previously observed,[30] and suggests that the computational methods underestimate the pK_a for strong acids in water and overestimate the pK_a for weak acids.
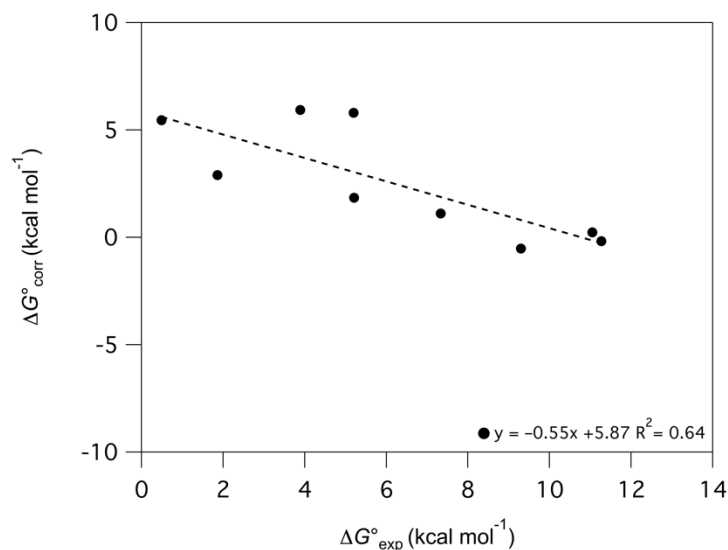
Figure 3.7. $\Delta G°_{corr}$ vs experimental pK_a for the organic acids in water.

The sloped relationship of Figure 3.7 implies that a linear empirical correction factor will be effective for the calculated acidity values. By solving for x in the linear fit of Figure 3.7, the correction factor for calculated pK_a values was determined (eq 9).

$$pK_{a,lfit} = 3.08 + 0.71(pK_{a,calc}) \tag{9}$$

Acidities for complexes **1-7** were calculated via equation 10 and then corrected according to (eq 9).

$$G°_{rxn} = G°_{red} + G°_{H^+} - G°_{[H]} \tag{10}$$

Table 3.3 contains the raw calculated acidity ($pK_{a,raw}$) and the corrected values based on the linear fit ($pK_{a,lfit}$) for the Cp*Ir-based complexes (**1 - 7**).

Table 3.3. Calculated and corrected acidities in water for hydrides 1 - 7.

complex	$pK_{a,raw}$	$pK_{a,lfit}$
1[H]	18.31	16.16
2[H]	20.41	17.66
3[H]	23.46	19.84
4[H]	26.70	22.16
5[H]	– 0.47	2.74
6[H]	18.37	16.21
6-2Na$^+$[H]	14.51	13.45
7[H]	9.72	10.02

An experimental acidity measurement is available for hydride complex **6**[H], pK_a = 12.4.[5]

Both models overestimate the pK_a for this complex, but complex **6-2Na$^+$**[H] is most consistent

with experiment. By applying a linear correction, which would correct for any inconsistencies in

the solvation model, the pK_a values were corrected and agree with the available experimental

data and more closely follow expected electronic trends.
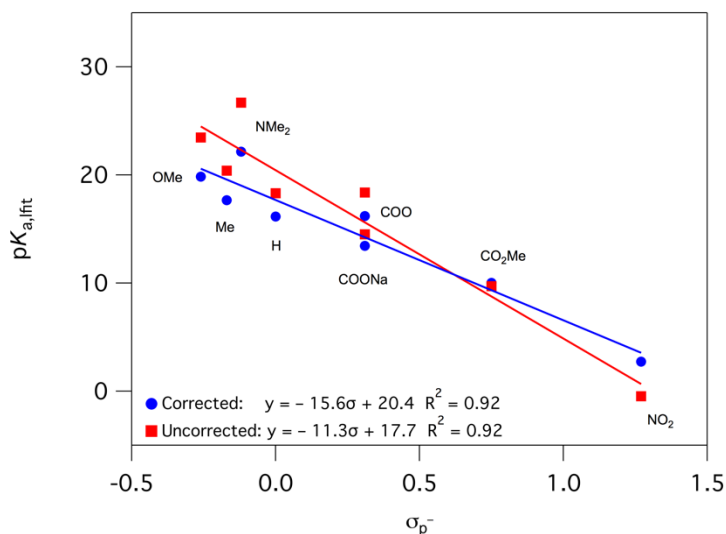
Figure 3.8. Calculated acidities of hydride complexes **1 - 7** (red) and acidities after the application of a linear correction factor (blue).

Figure 3.8 shows the correlation between the corrected pK_a values and the Hammett parameter, σ_p^-. Hydride complexes **1 - 7** are predicted to become stronger acids when substituted with electron-withdrawing groups, in line with electronic trends for phenols[39,40] and benzoic acids.[40] The transition metal complexes ($\rho = 11.1$) are predicted to be much more sensitive to substituent effects than phenols ($\rho = 2.1$ in water).[40]

3.3.5 Hydricity Determination.

The thermodynamic hydricity of iridium hydrides **1-7** is determined according to eq 1, using the calculated reduction potentials and acidity values. The values 1.364 and –46.12 in eq 1 convert the pK_a and reduction potential into kcal mol^{-1}, respectively, and 34.2 is the free energy required to reduce H$^+$ to H$^-$.[1,2] Table 3.4 shows the uncorrected hydricity values calculated from the raw reduction potentials and acidities (no correction) and the hydricity values obtained from calculation using the corrected potentials and pK_a values (Table 3.2 and Table 3.3). Reported experimental values are included where they are known.

Table 3.4. Aqueous hydricities for complexes **1 - 7** determined with uncorrected and corrected reduction potentials and acidities.

complex	$\Delta G°_{H^-}(H_2O)$ (kcal mol^{-1})		
	no correction	corrected	exp[5]
1[H]	31.68	32.44	31.5
2[H]	33.94	33.90	31.1
3[H]	32.05	30.82	30.8
4[H]	27.34	24.84	–
5[H]	37.20	45.28	–
6[H]	31.65	32.40	32.0
6-2Na$^+$[H]	34.01	36.26	32.0
7[H]	35.98	40.09	33.4

The calculated hydricity values agree with the experimental values. The directly calculated hydricity values, without taking any correction factors into account, show somewhat closer agreement with the experimental data than those obtained using empirical corrections. This was a surprising result in light of the improved apparent agreement between theory and experiment in the reduction potential and acidity calculations. Because hydricity is affected in opposing manners by the pK_a and reduction potential, it is possible to have an overestimated acidity and an underestimated reduction potential (or *vice versa*) — and yet still correctly predict the hydricity. After a thorough vetting of the method on different training sets, we believe that the individual corrected values are more accurate, even if the final hydricity value is not as consistent with experiment. However, the corrected values still show generally good agreement with experiment: all the calculated values are within 7 kcal mol^{-1} of experimental values, and three of the six values are within 1 kcal mol^{-1}. Perhaps more importantly for catalyst design, the trends in hydricity values are correctly predicted for the series of related complexes.

The importance of accuracy in the calculation of reduction potentials is illustrated by comparison of complexes **6**[H] and **6-2Na$^+$**[H]. Although the calculated acidity of complex **6-**

2Na⁺[H] is a closer match to the experimental value, the overall hydricity of complex **6**[H] is predicted to within 1 kcal mol^{-1} of the experimental value. For this reason, we believe that **6**[H] is a better model for experiment and use that value for the comparisons with experimental values.

Experimentally determined aqueous hydricity was found to have a positive correlation with the σ_p^- Hammett parameter in aqueous solution.[5] Electronic changes to the bipyridyl ligand were found to have a relatively small impact on hydricity, with the range of values only spanning 4 kcal mol^{-1} across the series. Figure 3.9 compares the trends observed experimentally with those predicted by DFT. Both uncorrected and corrected hydricity values show similar correlations to the electronic trend observed in experimental measurements. The narrow range of hydricity values poses a significant computational challenge, so the ability to reproduce the overall trend and magnitude of the experimental values is a substantial advance.
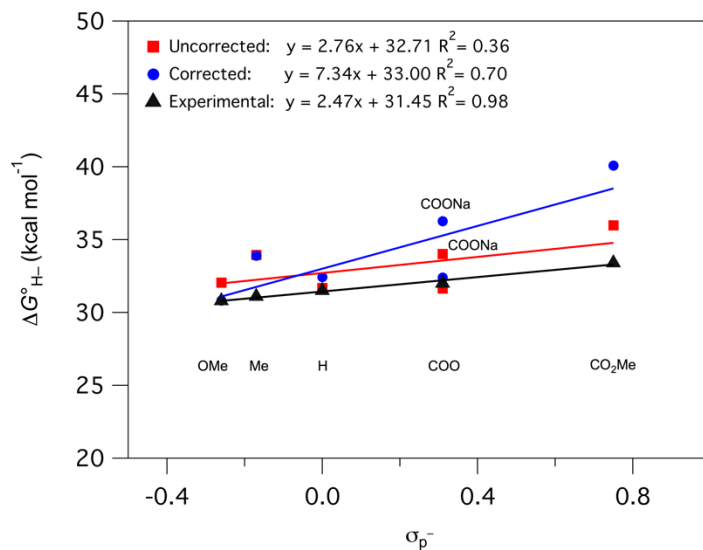
Figure 3.9. Comparison of corrected and uncorrected aqueous hydricities to experimentally determined values.

3.4 Conclusions

Thermodynamic hydricity values have been calculated in water using a pK_a – potential thermodynamic cycle. By employing both scalar and linear corrections, excellent agreement with predicted trends was observed for both aqueous reduction potentials and acidities for a series of iridium hydride complexes. The hydricity values obtained are in good agreement with experimental values. Fortunately, relatively accessible methods were sufficient to achieve good agreement. For example, explicit water solvation was not required.

The pK_a – potential thermodynamic cycle provides a wealth of thermochemical information, including reduction potentials, acidities, and hydricities. Whereas reduction potentials and acidity values for most Cp*Ir-based complexes could not be obtained experimentally due to limited solubility, predicted values are now available using this computational approach.

REFERENCES

(1)   Wiedner, E. S.; Chambers, M. B.; Pitman, C. L.; Bullock, R. M.; Miller, A. J. M.; Appel, A. M. *Chem. Rev.* **2016**, *116*, 8655–8692.

(2)   Connelly, S. J.; Wiedner, E. S.; Appel, A. M. *Dalton Trans.* **2015**, *44*, 5933–5938.

(3)   Taheri, A.; Thompson, E. J.; Fettinger, J. C.; Berben, L. A. *ACS Catal.* **2015**, *5*, 7140–7151.

(4)   Tsay, C.; Livesay, B. N.; Ruelas, S.; Yang, J. Y. *J. Am. Chem. Soc.* **2015**, *137*, 14114–14121.

(5)   Pitman, C. L.; Brereton, K. R.; Miller, A. J. M. *J. Am. Chem. Soc.* **2016**, *138*, 2252–2260.

(6)   Connelly Robinson, S. J.; Zall, C. M.; Miller, D. L.; Linehan, J. C.; Appel, A. M. *Dalton Trans.* **2016**, *45*, 10017–10023.

(7)   Fraze, K.; Wilson, A. D.; Appel, A. M.; Rakowski DuBois, M.; DuBois, D. L. *Organometallics* **2007**, *26*, 3918–3924.

(8)   Rakowski DuBois, M.; DuBois, D. L. *Chem. Soc. Rev.* **2009**, *38*, 62–72.

(9)   Rakowski DuBois, M.; DuBois, D. L. *Acc. Chem. Res.* **2009**, *42*, 1974–1982.

(10)   Helm, M. L.; Dubois, M. R.; Dubois, D. L. *Science* **2011**, *333*, 863–866.

(11)   Kang, P.; Meyer, T. J.; Brookhart, M. *Chem. Sci.* **2013**, *4*, 3497–3502.

(12)   DuBois, D. L.; Berning, D. E. *Appl. Organomet. Chem.* **2000**, *14*, 860–862.

(13)   Bullock, R. M.; Appel, A. M.; Helm, M. L. *Chem. Commun.* **2014**, *50*, 3125–3143.

(14)   Creutz, C.; Chou, M. H. *J. Am. Chem. Soc.* **2009**, *131*, 2794–2795.

(15)   Creutz, C.; Chou, M. H.; Hou, H.; Muckerman, J. T. *Inorg. Chem.* **2010**, *49*, 9809–9822.

(16)   Rodriguez-Maciá, P.; Dutta, A.; Lubitz, W.; Shaw, W. J.; Rüdiger, O. *Angew. Chem. Int. Ed.* **2015**, *54*, 12303–12307.

(17)   Gray, H. B. *Nat. Chem.* **2009**, *1*, 7.

(18)   Thoi, V. S.; Sun, Y.; Long, J. R.; Chang, C. J. *Chem. Soc. Rev.* **2013**, *42*, 2388–2400.

(19)   Mcdaniel, N. D.; Bernhard, S. *Dalton Trans.* **2010**, *39*, 10021–10030.

(20)   Teets, T. S.; Nocera, D. G. *Chem. Commun.* **2011**, *47*, 9268–9274.

(21)   Kirch, M.; Lehn, J.; Sauvage, J. *Helv. Chim. Acta* **1979**, *62*, 1345–1384.

(22)   Curtis, C. J.; Miedaner, A.; Ellis, W. W.; DuBois, D. L. *J. Am. Chem. Soc.* **2002**, *124*, 1918–1925.

(23)   Kovács, G.; Pápai, I. *Organometallics* **2006**, *25*, 820–825.

(24)   Johnson, S. I.; Nielsen, R. J.; Goddard III, W. A. *ACS Catal.* **2016**, *6*, 6362–6371.

(25) Muckerman, J. T.; Achord, P.; Creutz, C.; Polyansky, D. E.; Fujita, E. *Proc. Natl. Acad. Sci.* **2012**, *109*, 15657–15662.

(26) Qi, X. J.; Fu, Y.; Liu, L.; Guo, Q. X. *Organometallics* **2007**, *26*, 4197–4203.

(27) Marenich, A. V; Ho, J.; Coote, M. L.; Cramer, C. J.; Truhlar, D. G. *Phys. Chem. Chem. Phys.* **2014**, *16*, 15068–15106.

(28) Marenich, A. V.; Majumdar, A.; Lenz, M.; Cramer, C. J.; Truhlar, D. G. *Angew. Chem. Int. Ed.* **2012**, *51*, 12810–12814.

(29) Baik, M. H.; Friesner, R. A. *J. Phys. Chem. A* **2002**, *106*, 7407–7412.

(30) Muckerman, J. T.; Skone, J. H.; Ning, M.; Wasada-Tsutsui, Y. *Biochim. Biophys. Acta* **2013**, *1827*, 882–891.

(31) Qi, X.-J.; Liu, L.; Fu, Y.; Guo, Q.-X. *Organometallics* **2006**, *25*, 5879–5886.

(32) Frisch, M. J.; Trucks, G. W.; Schlegel, H. B.; Scuseria, G. E.; Robb, M. A.; Cheeseman, J. R.; Scalmani, G.; Barone, V.; Mennucci, B.; Petersson, G. A.; Nakatsuji, H.; Caricato, M.; Li, X.; Hratchian, H. P.; Izmaylov, A. F.; Bloino, J.; Zheng, G.; Sonnenberg, J. L.; Hada, M.; Ehara, M.; Toyota, K.; Fukuda, R.; Hasegawa, J.; Ishida, M.; Nakajima, T.; Honda, Y.; Kitao, O.; Nakai, H.; Vreven, T.; Montgomery, J. A., J.; Peralta, J. E.; Ogliaro, F.; Bearpark, M.; Heyd, J. J.; Brothers, E.; Kudin, K. N.; Staroverov, V. N.; Kobayashi, R.; Normand, J.; Raghavachari, K.; Rendell, A.; Burant, J. C.; Iyengar, S. S.; Tomasi, J.; Cossi, M.; Rega, N.; Millam, J. M.; Klene, M.; Knox, J. E.; Cross, J. B.; Bakken, V.; Adamo, C.; Jaramillo, J.; Gomperts, R.; Stratmann, R. E.; Yazyev, O.; Austin, A. J.; Cammi, R.; Pomelli, C.; Ochterski, J. W.; Martin, R. L.; Morokuma, K.; Zakrzewski, V. G.; Voth, G. A.; Salvador, P.; Dannenberg, J. J.; Dapprich, S.; Daniels, A. D.; Farkas, Ö.; Foresman, J. B.; Ortiz, J. V.; Cioslowski, J.; Fox, D. J. 9th ed. Gaussian, Inc.: Wallingford, CT 2009.

(33) Bruce, D.; Richter, M. M. *Anal. Chem.* **2002**, *74*, 1340–1342.

(34) Prakash, M.; Samy, K. G.; Subramanian, V. *J. Phys. Chem. A* **2009**, *113*, 13845–13852.

(35) Izutsu, K. *Electrochemistry in Nonaqueous Solutions*; Wiley-VCH: Weinheim, 2002.

(36) Kerr, E.; Doeven, E. H.; Barbante, G. J.; Connell, T. U.; Donnelly, P. S.; Wilson, D. J. D.; Ashton, T. D.; Pfeffer, F. M.; Francis, P. S. *Chem. Eur. J.* **2015**, *21*, 14987–14995.

(37) Warren, J. J.; Tronic, T. A.; Mayer, J. M. *Chem. Rev.* **2010**, *110*, 6961–7001.

(38) Hansch, C.; Leo, A.; Taft, R. W. *Chem. Rev.* **1991**, *91*, 165–195.

(39) Bordwell, F. G.; Mccallum, R. J.; Olmstead, W. N. *J. Org. Chem.* **1984**, *49*, 1424–1427.

(40) Chantooni, M. K.; Kolthoff, I. M. *J. Phys. Chem.* **1976**, *80*, 1306–1310.

Chapter 4: Interrogating the Connection Between Ligand Electronic Effects and Solvation in Thermodynamic Hydricity

4.1   Introduction

Transition metal hydrides are key intermediates in organometallic catalysis in a range of solvents, from non-polar aprotic, to polar aprotic, to protic and aqueous.[1–4] Switching solvents can have dramatic effects on the activity or mechanism of a catalytic reaction. For example, Wiedner *et al.* demonstrated a change in mechanism for CO_2 reduction by a cobalt hydride when switching from tetrahydrofuran (THF) to water.[5] In water, hydride transfer to CO_2 from a cobalt dihydride complex precedes coordination of H_2 and deprotonation by $NaHCO_3$. In THF, however, deprotonation with a strong base (Verkade's base) activates the complex for hydride transfer to CO_2. The improved thermodynamics for hydride donation in water allow for the use of $NaHCO_3$ rather than Verkade's base in THF. The identification of measurable parameters that can inform and guide catalyst design represents an ongoing challenge. The hydricity (ΔG^o_{H-}), or hydride donating ability, of a transition metal has emerged as a promising thermodynamic parameter in this regard (Figure 4.1).[6,7]

A. *Potential-pK_a* Thermodynamic Cycle

$$L_nM-H^+ \xrightleftharpoons{pK_a} L_nM \; + \; H^+$$

$$\Delta G^{\circ}_{H-} \qquad E^{\circ}_{(III/I)} \quad E^{\circ}_{(H+/H-)}$$

$$L_nM^{2+} \; + \; H^-$$
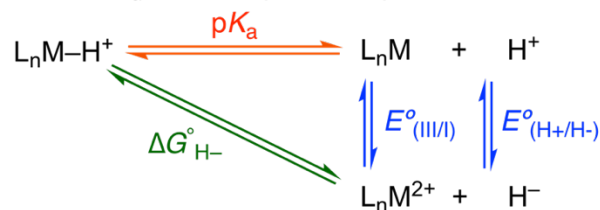
B. *Equilibria with Reference Compound*

$$L_nM-H^+ + ref^{2+} \xrightleftharpoons{K_{eq}} L_nM^{2+} + ref-H^+$$

C. *Hydrogen Cleavage*

$$L_nM^{2+} + B + H_2 \xrightleftharpoons{K_{eq}} L_nM-H^+ + HB^+$$

Figure 4.1. Methods for the experimental measurement of hydricity for a hydride L_nM-H^+. A. Construction of a thermodynamic cycle composed of the hydride acidity (pK_a), reduction potential (E°) and the solvent-dependent constant for the reduction of H^+ to H^-. B. Measurement of relative hydride donating ability through equilibration with a reference complex (ref–H^+). C. Measurement of hydricity relative to H_2 in the presence of a base (B is external base or water solvent).

The hydricities of over 100 transition metal hydride complexes are known in acetonitrile.[6] However, there is increasing interest in exploring how different solvents influence the thermodynamics of hydride transfer. Several studies have grappled with the difficulties inherent in the application of the methods shown in Figure 4.1 to the determination of hydricity in water.[6,8–11] When constructing a potential–pK_a thermodynamic cycle, the often water-insoluble conjugate base of the hydride (species L_nM in Figure 4.1A) inhibits the required electrochemical and acidity measurements. Attempts at equilibration of a hydride complex with H_2 in water (Figure 4.1C) must also overcome challenges of limited H_2 solubility.

Our group developed a general method for the measurement of aqueous hydricity through the utilization of an iridium hydride complex with a water-soluble conjugate base, [Cp*Ir(bpy-COO⁻)H]⁻ (Cp* = η^5–pentamethylcyclopentadienyl, bpy-COO⁻ = 4,4'-dicarboxylate-2,2'-

bipyridine), as a reference. Once the hydricity of a reference complex was known, hydride equilibration (Figure 4.1B) could be used to add four additional Ir hydrides and three Ru hydride complexes to the scale of known aqueous hydricities.[8]

Scheme 4.1. Effective hydricity as a sum of the hydricity (ΔG°_{H-}) and the free energy for association of solvent or an external ligand (ΔG°_{assoc}).
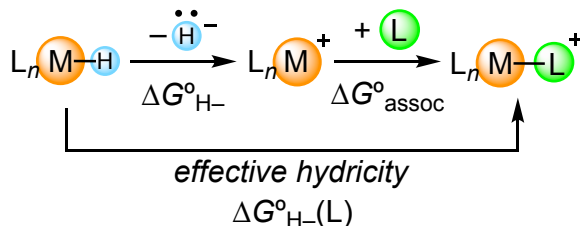
Our recent determination of the aqueous hydricity of five structurally homologous complexes provided a rare opportunity to correlate electronic parameters with thermodynamic hydricity values.[8] In water, changes to the supporting ligand influenced hydride donating ability by ~ 3 kcal mol^{-1}. This is a relatively modest span, considering the known range of hydricities between 14 and 42 kcal mol^{-1}. In fact, we observed that the ligand L in Scheme 4.1 can influence the favorability of hydride transfer by ~ 5 kcal mol^{-1} through the formation of a more stable complex after hydride transfer. This influence of an incoming ligand that coordinates to the iridium center is described as the *effective hydricity* of a complex.[6,8] Tuning the effective hydricity through changes to the medium (e.g. chloride addition) had a larger influence on the thermodynamics of hydride donation than bipyridine electronic tuning for this series.

A general method for the determination of aqueous hydricity, and a recognition of the importance of considering effective hydricity, provides new opportunities for comparing hydricity in water and organic solvents. Since the seminal reports on the hydricities of two Ru complexes by Creutz in acetonitrile and water,[12,13] the hydricity of only a handful of other complexes have been characterized in multiple solvents.[7–11] There is still limited understanding

of how different solvents affect the thermodynamics of hydride transfer and — importantly — whether the approaches to catalyst design and ligand tuning should vary depending on the solvent.

Of particular concern is how changing solvents will influence (a) the impact of tuning the ligand electronic structure and (b) the impact of ligand association after hydride release (effective hydricity). In moving to a less polar solvent, one might expect that the supporting ligands could have a greater role in the stabilization of the products of hydride transfer. Indeed, classic physical organic studies show a striking solvent effect on the degree of electronic influence on the ionization of organic acids, with the slopes (ρ) of Hammett correlation plots 2-4 times larger for organic solvents when compared with aqueous studies.[14,15] However, no studies of electronic trends in hydricity have been reported in two solvents. A change in solvent is also expected to have a significant impact on effective hydricity, with the Ir–L bond strengths formed after hydride transfer varying significantly for cases where L is the solvent itself or L is a charged additive.

Herein, we report the first comparison of a series of electronically tuned iridium hydrides in two solvents. The hydride complex $[Cp^*Ir(bpy)(H)]^+$ ($Cp^* = \eta^5$–pentamethylcyclopentadienyl and bpy = 2,2–bipyridine) and its analogs are frequently used catalysts for a variety of transformations due to their stability and acid tolerance.[16–19] Altering substitution at the 4 and 4' positions on bipyridine is a synthetically facile method to develop a library of complexes commonly used in catalyst screens.[20–24] Combined with our prior data set in water,[8] we can assess the magnitude of the difference in hydricity between acetonitrile and water, the relative influence of the supporting bipyridine ligand, and the role of external ligands that can coordinate after hydride release. With the aid of Density Functional Theory (DFT) and Natural Bond Orbital

(NBO) analysis, we draw a more complete picture of the influence of solvation on hydricity. The implications of solvent effects on approaches to tuning molecular catalysts are considered.

4.2   Results and Discussion

Scheme 4.2. Synthetic routes to iridium complexes under study.

1NCCH₃: R = H
2NCCH₃: R = CH₃
3NCCH₃: R = C(CH₃)₃
4NCCH₃: R = OCH₃
5NCCH₃: R = CO₂Me
6NCCH₃: R = CF₃

[1H]PF₆: R = H
[2H]PF₆: R = CH₃
[3H]PF₆: R = C(CH₃)₃
[4H]PF₆: R = OCH₃

[5H]OTf: R = CO₂Me
[6H]OTf: R = CF₃

[1H]Cl: R = H
[2H]Cl: R = CH₃
[3H]Cl: R = C(CH₃)₃
[4H]Cl: R = OCH₃
[5H]Cl: R = CO₂Me
[6H]Cl: R = CF₃

1Cl: R = H
2Cl: R = CH₃
3Cl: R = C(CH₃)₃
4Cl: R = OCH₃
5Cl: R = CO₂Me
6Cl: R = CF₃
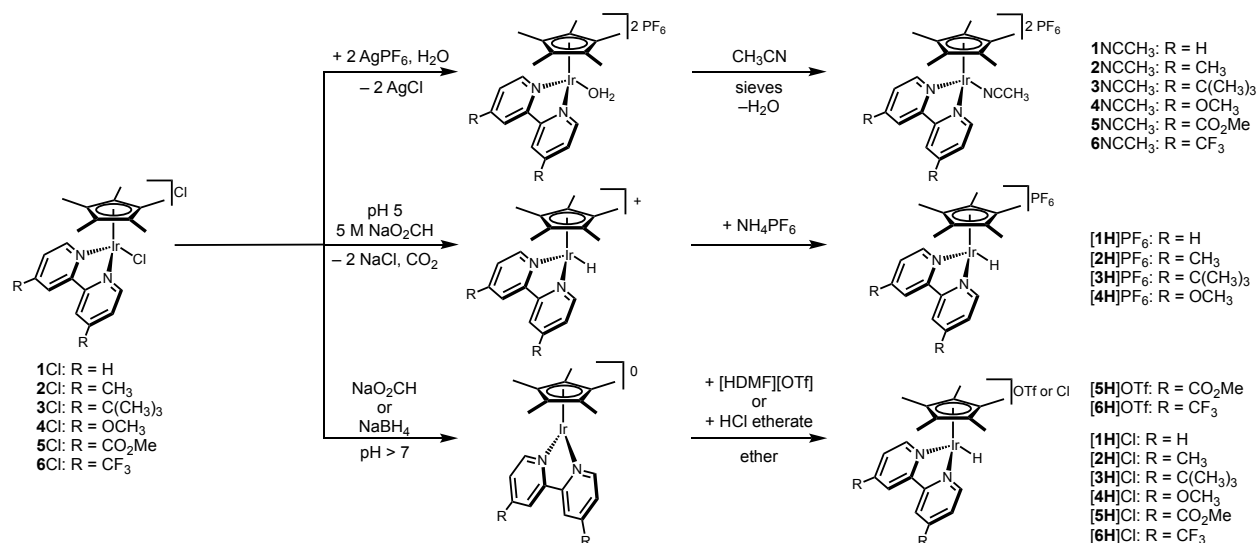
4.2.1   Synthesis of Iridium Complexes

A range of iridium hydride donor and acceptor pairs were needed for the targeted thermodynamic studies. The previously reported iridium chloride complexes, [Cp*Ir(bpy-X)(Cl)][Cl], (bpy-X = 2,2'-bipyridine where X indicates substituents at the 4 and 4' positions) were synthesized through the addition of 2 equiv of a bipyridine ligand to [Cp*Ir(Cl)₂]₂ in methanol.[25] The iridium acetonitrile complexes (top route in Scheme 4.2) were synthesized via chloride abstraction from [Cp*Ir(bpy-X)(Cl)][Cl], with 2 equiv AgPF₆ in water.[19] Removal of AgCl by filtration yielded a yellow solution of [Cp*Ir(bpy-X)(OH₂)][PF₆]₂ which was isolated as a pale yellow solid *in vacuo*. Extraction with MeCN displaced the aqua ligand and gave [Cp*Ir(bpy-X)(NCCH₃)][PF₆]₂ as confirmed by NMR spectroscopy. Vapor diffusion of Et₂O into a MeCN solution of [Cp*Ir(bpy-CF₃)(NCCH₃)][PF₆]₂ (**6NCCH₃**) formed pale yellow block-shaped single crystals. An X-ray diffraction study confirmed the expected "piano stool" iridium

90

dication with a bound acetonitrile ligand. Besides the bimetallic complex, [Cp*Ir(NCCH$_3$)(μ-bpm)Ru(bpy)$_2$]$^{4+}$ (bpm = 2,2-bipyrimidine) discussed in Chapter 2, no other [Cp*Ir(bpy-X)(NCCH$_3$)]$^{2+}$ crystal structures have been reported. Typical iridium-nitrile bond distances range from 1.994 Å for [Ir(Cl)$_3$(NCCH$_3$)$_3$][26] to 2.021 Å for an ethylene bridged bimetallic iridium complex, shorter than that observed in complex **6NCCH$_3$**.[27] The iridium-nitrogen bond length to the bipyridine ligand is identical to the bond length observed in [Cp*Ir(bpy-CF$_3$)(Cl)]$^+$ suggesting a weak, dative iridium-acetonitrile bond.[28]
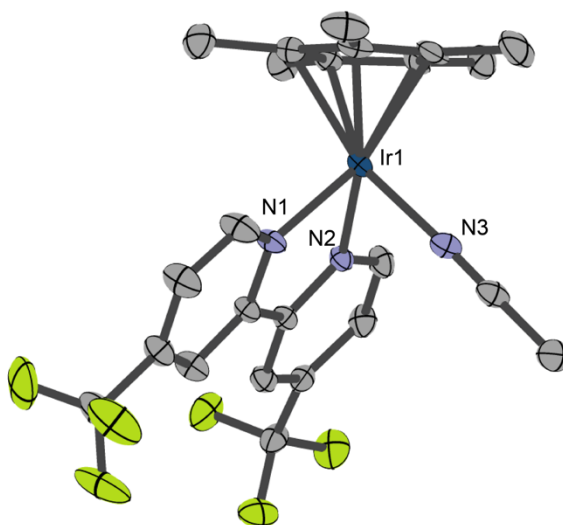
Figure 4.2. Structural representation of **6NCCH$_3$** with ellipsoids drawn at the 50% probability level. The asymmetric unit contains two hexafluorophosphate ions that are not shown. Hydrogen atoms are omitted for clarity. The major site of one disordered CF$_3$ subsituent is shown. Selected distances (Å): Ir1–N1 2.090(3), Ir–N2 2.103(3), Ir–N3 2.053 (4).

Iridium hydride complexes were prepared with either chloride, triflate, or hexafluorophosphate counter ions. The chloride counter ions are essential for aqueous studies, based on the improved water solubility. Hydrides of the type [Cp*Ir(bpy-X)(H)][Cl] were accessed by reduction of the corresponding Ir chloride complex with sodium borohydride or

sodium formate in 0.1 M NaOH, resulting in precipitation of the neutral conjugate base, Cp*Ir(bpy-X), as a dark solid. Protonation of the conjugate base in diethyl ether with HCl led to precipitation of [Cp*Ir(bpy-X)(H)][Cl].[8] To reach the hexafluorophosphate salt of the hydride, the use of formate in slightly acidic water (pH 3-5) generates aqueous solutions of [Cp*Ir(bpy-X)(H)]$^+$. Addition of 2 equiv NH$_4$PF$_6$ results in precipitation of the hydride as the hexafluorophosphate salt.[29]

To reach the triflate salts of the more acidic hydrides **5H** and **6H**, reduction of the iridium chloride complex to form the Ir^I complex followed by protonation with dimethylformamidium trifluoromethanesulfonate ([HDMF][OTf]).

4.2.2 Hydricity Determination in Water

Our general approach to determining hydricity values in water involves establishing a reference complex through a potential–pK_a thermodynamic cycle, followed by measuring relative hydricities for other complexes through equilibrium reactions. The reference complex, [Cp*Ir(bpy-COO$^-$)(H)]$^-$ was chosen because the charged carboxylate substituents on the bipyridine ligand impart water solubility to the conjugate base, allowing for determination of the hydricity of the complex according to Figure 4.1A (above). The acidity of [Cp*Ir(bpy-COO$^-$)(H)][Cl] was determined through a spectrophotometric titration. The reduction potential of [Cp*Ir(bpy-COO$^-$)(OH$_2$)]$^{2+}$ was determined uing redox potentiometry, allowing for the calculation of hydricity, $\Delta G^o_{H-}(OH_2) = 32.0$ kcal mol^{-1} in water. The parenthetical notation indicates the ligand that is bound to iridium after hydride transfer.

The influence of the "coordinating ligand" chloride on the effective hydricity could be assessed readily based on the partial ligand displacement that occurs in the aqueous medium. Upon dissolution in phosphate buffer, speciation of [Cp*Ir(bpy-COO$^-$)(Cl)]$^+$ is observed to form

the aqua complex, $[Cp*Ir(bpy\text{-}COO^-)(OH_2)]^{2+}$ and the phosphato complex. This dissociation

indicates that the binding strength for chloride association, $\Delta G°_{H_2O \to Cl}$ in water is weak enough to

be measured by ^{1}H NMR spectroscopy. $\Delta G°_{H_2O \to Cl}$ was determined through preparation of

solutions of each aquo complex with varying amounts of NaCl. After equilibrium had been

reached, the concentrations of each species were determined by ^{1}H NMR spectroscopy in order

to establish the free energy associated with chloride binding $\Delta G°_{H-}(Cl) = 27.6$ kcal mol^{-1} in

water. The chloride binding affinity for each species was determined in a similar manner and the

chloride complexes were found to be ~4.5 kcal mol^{-1} more stable than the aquo complexes in

water.

Using $[Cp*Ir(bpy\text{-}COO^-)(Cl)]^+$ as a reference, the relative hydricities for four other

iridium hydride complexes were determined through equilibrium reactions. In a representative

hydride equilibration (eq 1), a solution of [**4H**]Cl in 0.1 M sodium phosphate solution in D$_2$O

adjusted to pD 7 was mixed with the chloride complex of $[Cp*Ir(bpy)(Cl)][Cl]$ (**1Cl**).

$$[\textbf{4H}]Cl + \textbf{1Cl} \leftrightarrows \textbf{4Cl} + [\textbf{1H}]Cl \qquad\qquad \Delta\Delta G°(Cl) \qquad\qquad (1)$$
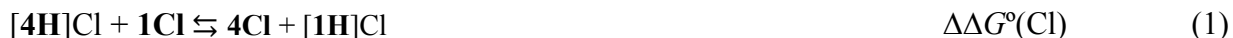
Equilibration was typically established within 10 minutes and the concentrations of all four

species were determined by ^{1}H NMR spectroscopy.

4.2.3 Hydricity Determination in Acetonitrile

Previous work from our lab has established the hydricity of $[Cp*Ir(bpy)(H)][OTf]$

through a potential–pK_a thermodynamic cycle in acetonitrile, $\Delta G°_{H-}(NCCH_3) = 62$ kcal mol^{-1}. To

determine the hydricity of the full family of substituted bipyridine complexes in acetonitrile,

various pairs of nitrile complexes and hydride complexes (each supported by a different

bipyridine ligand as the hexafluorophosphate, PF$_6^-$, salt) were allowed to reach equilibrium (an

example equilibration reaction is shown in eq 2).

$$[\mathbf{4H}]PF_6 + \mathbf{1NCCH_3} \leftrightharpoons \mathbf{4NCCH_3} + [\mathbf{1H}]PF_6 \qquad\qquad \Delta\Delta G^o(NCCH_3) \qquad (2)$$

While equilibrium was reached within minutes for aqueous reactions, reactions in acetonitrile took several days to equilibrate. This observation of slow kinetics is consistent with previous reports for Ru complexes investigated by Creutz.[30,31] Although the solvent dependence of *kinetic hydricity* is as yet unknown for transition metal hydrides, it has been observed that the addition of "hydride shuttles" (such as pendant boranes) can improve the kinetics of hydride transfers in organic solvents.[32,33] The faster kinetics in water could be resulting from the ability for water to stabilize the charged H^- ion or the $[Cp^*Ir(bpy)]^{2+}$ species resulting from hydride transfer which might accelerate ligand dissociation, but further work is needed.

For each reaction, the concentrations of all four species were determined by ^1H NMR spectroscopy through reference to a mesitylene internal standard in order to calculate an equilibrium constant for the reaction. The relative differences in hydricities for these complexes is shown in Figure 4.3. Each hydride complex was equilibrated with at least two other species to give $\Delta\Delta G^o(NCCH_3)$ values that are consistent within experimental uncertainty (± 0.1 kcal mol^{-1}).
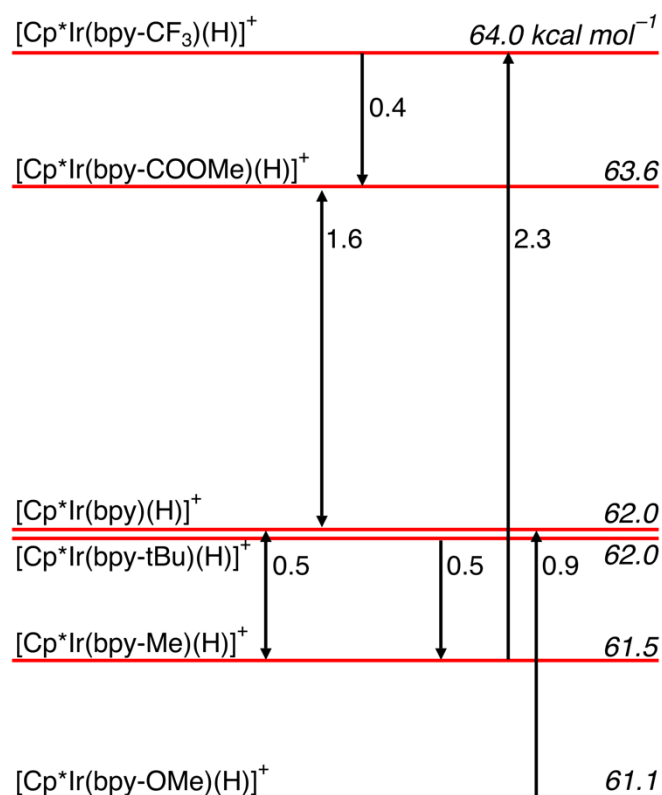
Figure 4.3. Relative hydricities measured in acetonitrile with values referenced to [Cp*Ir(bpy)(H)]$^+$ shown on right. Black arrows show relative equilibria with arrow pointing from the starting hydride complex towards the starting nitrile complex for the equilibrium.

4.2.4 Substituent Effects in Water and Acetonitrile: Tuning with the Supporting Ligand.

Using the measured hydricities, a Hammett plot can be constructed to measure the relative influence of substitution on the bipyridine ligand. In water, a strong correlation was observed between the Hammett parameter, σ_p^- (which accounts for resonance stabilization) and hydricity.[34,35] For these studies, we have used the sum of the σ_p^- values for each substituent ($\Sigma\sigma_p^-$), as suggested by Jaffé.[36]
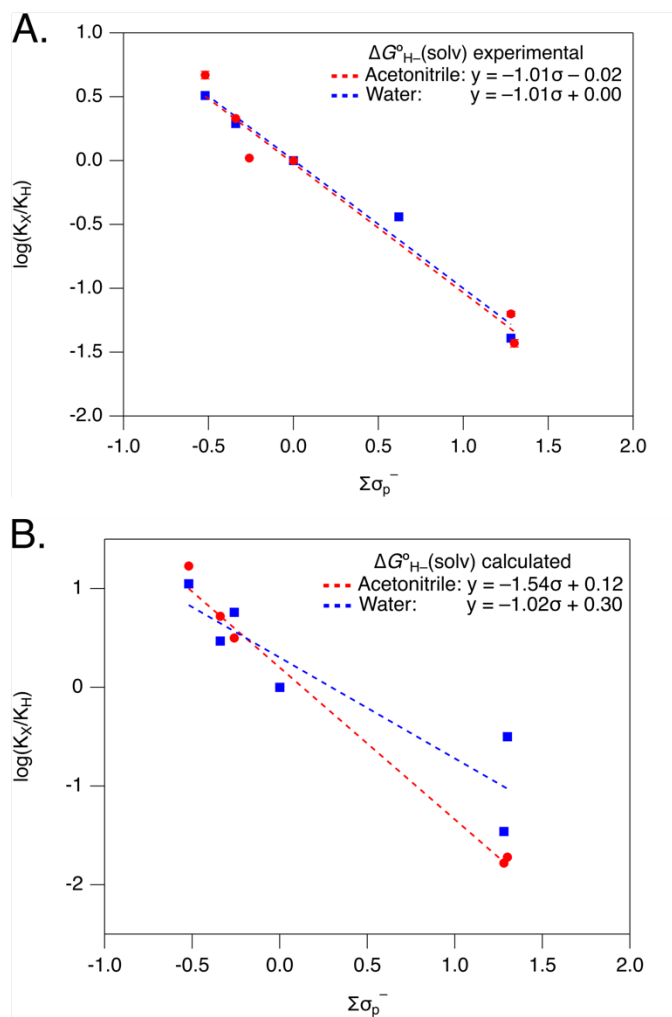
Figure 4.4. A. Hammett correlation of $\Sigma\sigma_p^-$ and $\log(K_X/K_H)$ as measured by hydride equilibration reactions. B. Hammett correlation of $\Sigma\sigma_p^-$ and $\log(K_X/K_H)$ as calculated by DFT. Dotted lines show best fit of data points.

96

A.

ΔG°_{H-}(solv) experimental
- - - Acetonitrile: y = −1.01σ − 0.02
- - - Water: y = −1.01σ + 0.00

B.

ΔG°_{H-}(solv) calculated
- - - Acetonitrile: y = −1.54σ + 0.12
- - - Water: y = −1.02σ + 0.30
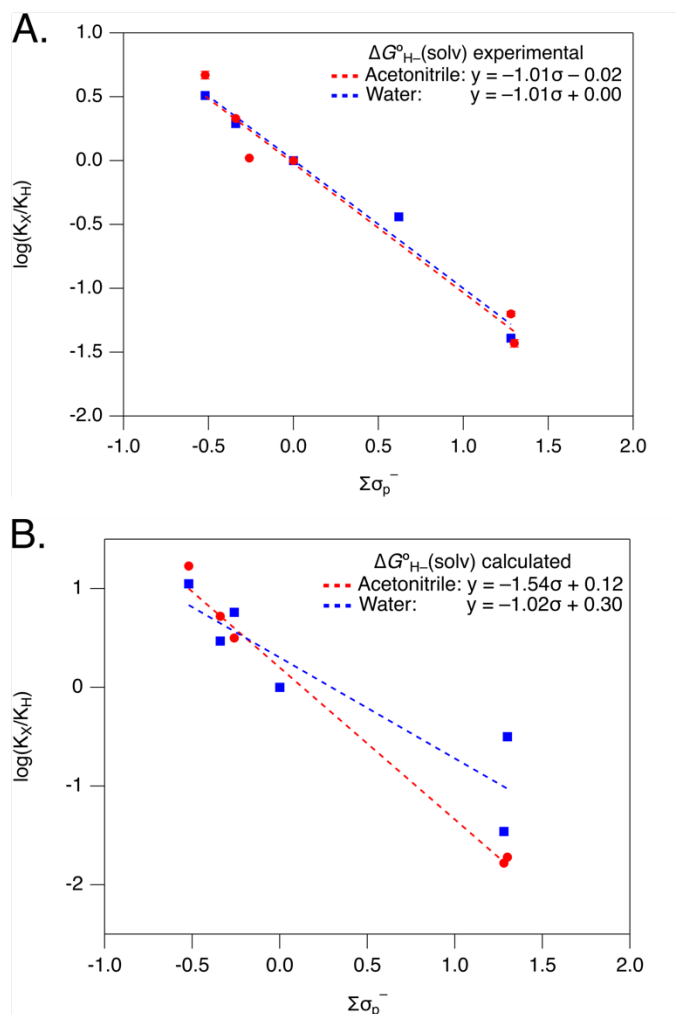
Figure 4.4A is a Hammett plot exhibiting a linear correlation between the relative hydricity (expressed as a ratio of equilibrium constants) and the sum of the σ_{p-} parameter values for each subsitutent[36,37] (that account for resonance stabilization) for both water and acetonitrile. Density functional theory (DFT) calculations of the relative hydricities for each complex were performed using isodesmic reactions (in direct analogy to the experimental measurements), Figure 4.4B. The small difference between ρ values is also predicted using DFT.

Traditional Hammett studies of the ionization of substituted benzoic acids and phenols show much greater difference in ρ between acetonitrile and water (1:2.4 for benzoic acids and 2.1:4.4 for phenols),[14] with both systems being more electronically responsive in

acetonitrile.[14,15,38] We hypothesize that the ability of the iridium complexes to effectively

delocalize charge over a large molecule (in contrast to the more localized charges in phenolate

and benzoate) may minimize the solvent influence on electronic trends of the supporting ligand.

NBO analysis of the iridium hydride bond across the series of complexes was used as a

tool to interrogate this hypothesis. NBO calculations were performed on the optimized structures

of the hydride complexes under study using the B3LYP functional. Using Natural Population

Analysis (NPA), the influence of substitution on the charge density at iridium and at the hydride

was investigated for each hydride complex (Figure 4.5). The overlay of the lines in Figure 4.5

reflect the experimental observation that solvation does not dramatically influence the electronic

nature of the metal hydride bond. In both water and acetonitrile, the iridium is equally involved

in the delocalization of charge for the complex. *The combined data suggest that, for this family*

of iridium hydrides, substituent tuning on the supporting ligand will change the hydricity by the

same amount in acetonitrile and water.
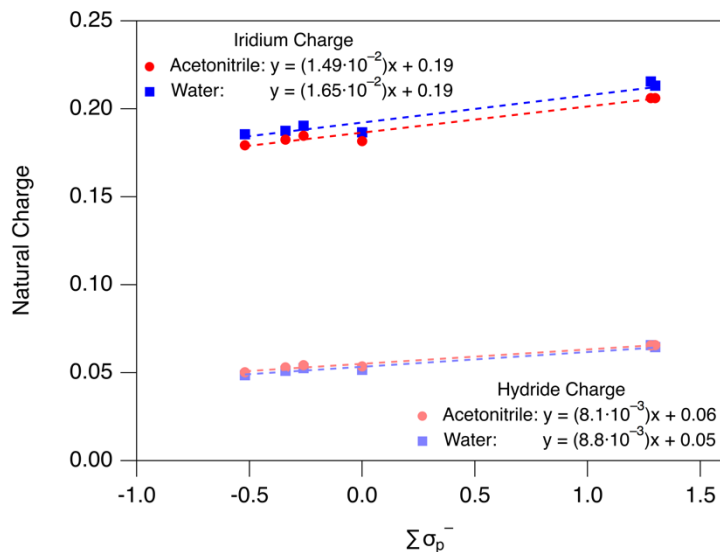
Figure 4.5. Correlation between the electron donating ability of the bipyridine substituents ($\Sigma\sigma_p^-$) and the natural charge of the iridium atom and hydride atom.

4.2.5   Origin of Changes in Hydricity Between Water and Acetonitrile.

Although the electronic trends in hydricity remain consistent across these two solvents, the *magnitude* of ΔG°_{H-} changes dramatically for all complexes with hydricities reported in multiple solvents — with an typical difference of a full 30 kcal mol^{-1}. The sources for this large difference between hydricity in water and acetonitrile are as yet unknown, and similar shifts are seen in the few other examples of hydricity values obtained in both solvents.[7–11,13,31,39]

Scheme 4.3. Overall reaction for effective hydricity composed of the elementary steps for metal-hydride bond scission and solvent coordination.

Overall Reaction:

$$[L_nM–H]^+ \xrightarrow[\text{solvent}]{\Delta G°_{H^-}\text{(solv)}} H^- + [L_nM–solv]^{2+}$$
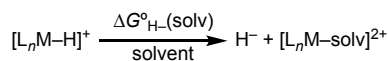
Elementary Steps:
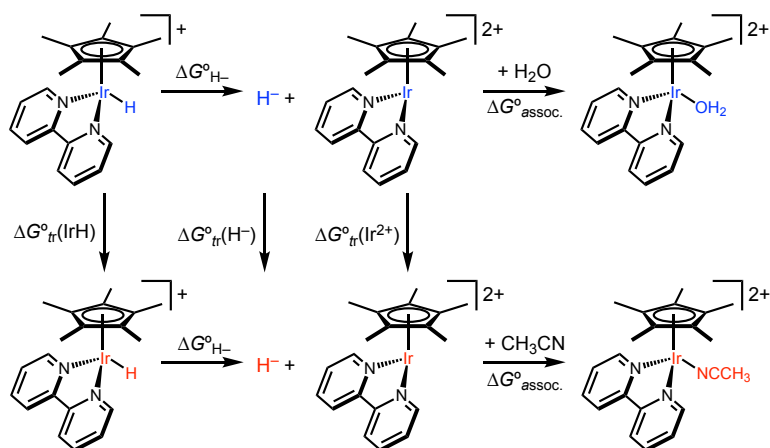
To better understand the origin of the difference in hydricity between solvents, we considered Scheme 4.3, which illustrates the key thermodynamic parameters that will influence hydricity when moving from one solvent to another. We hypothesized that two effects would dominate: first, the free energy of transfer from one solvent to another ($\Delta G°_{tr}$) for the iridium hydride, the dicationic iridium, and the hydride anion; and second, the free energy of solvent association ($\Delta G°_{assoc.}$) to the 16e$^-$ dicationic iridium complex to form the solvento complex.

Because the 16e$^-$ species is not experimentally accessible, we elected to assess this reaction scheme using DFT methods. The free energy of transfer for each species, X, was calculated using equation 3, where $\Delta G°_{sv}$ is the solvation energy for the species.

$$\Delta G°_{tr(aq\rightarrow MeCN)}(X) = \Delta G°_{sv(MeCN)}(X) - \Delta G°_{sv(aq)}(X) \tag{3}$$

Optimized geometries and free energy calculations were performed on each iridium species in both water and acetonitrile. Taking the difference in free energy provided the free

energy of transfer for each iridium species. The computed energies for the transfer of

[Cp*Ir(bpy)(H)]$^+$ and [Cp*Ir(bpy)]$^{2+}$ from water to acetonitrile are shown in **Table 4.1**.

Table 4.1. Transfer energies for iridium species involved in hydride donation.

Species	$\Delta G^{o}_{tr(aq \to MeCN)}$ kcal mol^{-1}
[Cp*Ir(bpy)(H)]$^+$	−10.8
[Cp*Ir(bpy)]$^{2+}$	−8.0

The free energy of H$^-$ ion transfer from acetonitrile to water, which has apparently not

been previously reported, was obtained using thermochemical cycles. Combining the free energy

for H$_2$ heterolysis in water and acetonitrile with the previously determined transfer free energy

for a proton (eq 4-6)[40] provides an approximation for the transfer energy of a hydride ion from

acetonitrile to water (eq 7). According to eq 7, it is 27.7 kcal mol^{-1} endergonic to transfer a

hydride ion from water to acetonitrile.

$$H_{2(g)} \leftrightarrows H^+_{(MeCN)} + H^-_{(MeCN)} \qquad 76.0 \text{ kcal mol}^{-1} \qquad (4)$$
$$H^+_{(aq)} + H^-_{(aq)} \leftrightarrows H_{2(g)} \qquad -34.2 \text{ kcal mol}^{-1} \qquad (5)$$
$$H^+_{(MeCN)} \leftrightarrows H^+_{(aq)} \qquad -14.1 \text{ kcal mol}^{-1} \qquad (6)$$
$$H^-_{(aq)} \leftrightarrows H^-_{(MeCN)} \qquad 27.7 \text{ kcal mol}^{-1} \qquad (7)$$
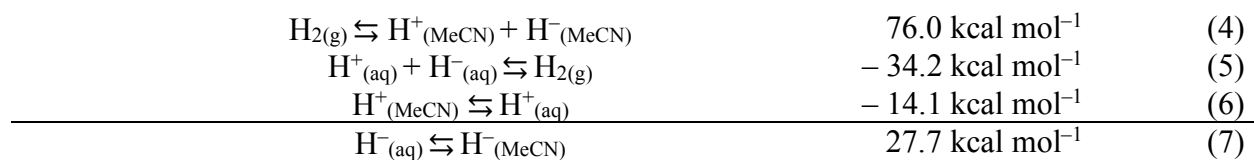
Considering the small transfer free energies associated with the iridium complexes, this

analysis suggests that the dominant contribution to the change in magnitude of hydricity is the

relative stability of the free hydride ion. In fact, the value from eq 7 is in good agreement with

the experimentally observed difference in hydricity for [Cp*Ir(bpy)(H)]$^+$.

This analysis should be general for any hydride donor, and not every hydride donor is

expected to be dominated by the free hydride ion. If that were the case, the difference in

hydricity would be constant, whereas experimental studies have observed significant differences

in the solvent effect. We expect that highly charged hydride donors, or pairs wherein the donor and acceptor have significantly different solvation energies due to structural reorganization or other changes, are most likely to show significant deviations 27.7 kcal mol^{-1}. Notable examples of large deviations from 27 kcal mol^{-1} include formate,[41–43] the bimetallic Ir-Ru catalyst examined in chapter 2 $\Delta G^{\circ}_{tr(MeCN \rightarrow aq)} = 33.4$ kcal mol$^{-1})$[7], and the polymetallic iron hydride reported by Berben et $al.$ ($\Delta G^{\circ}_{tr(MeCN \rightarrow aq)} = 34$ kcal mol^{-1}).[9]

Another significant factor in the solvent influence on hydricity values comes from the fact that experimental measurements are often measuring $effective$ $hydricity$ that includes ligation of solvent. Differences in binding affinity for water and nitrile could lead to a significant shift in hydricity between solvents. According to DFT calculations, association of acetonitrile ($\Delta G^{\circ}_{assoc}(NCCH_3) = 4.6$ kcal mol^{-1}) is slightly less uphill than the association of water ($\Delta G^{\circ}_{assoc}(H_2O) = 5.6$ kcal mol^{-1}). While similar in magnitude, the binding of solvent still comprises an important aspect of the thermodynamics of hydride donation for complexes such as these. This association energy can be expected to vary depending on the geometry of the complex after hydride donation. For example, DuBois et $al.$ investigated five-coordinate d^8 complexes which upon hydride donation generate square planar 16e$^-$ complexes which do not strongly bind solvents or other ligands.[30,41,44–46] For these complexes, the effective hydricity measured in experiment will more closely approximate the "true" hydride donating ability as the association energy will not contribute significantly to the overall thermodynamic driving force. In summary, the main factors contributing to the magnitude of the solvent dependence of hydricity are the difference in solvation of the hydride ion, the relative charge and charge delocalization of the hydride species, and the association energy for the coordination of solvent after hydride donation.

4.2.6 Solvent Dependence of Chloride Binding

In water, coordination of ligands such as chloride following hydride transfer was found to have a significant influence on the overall thermodynamics of hydride transfer, enhancing the hydricity.[8] This discovery suggests that hydricity can be tuned by external additives as well as through synthetic modification. Binding an added ligand after hydride release remains essentially unstudied in MeCN, apart from a few examples where formate adducts were observed after CO_2 reduction (the influence on hydricity was not quantified).[47] We were interested in how chloride ions would influence the effective hydricity in acetonitrile solvent, and how this influence compared with prior observations in water. Furthermore, we wondered if the change in overall charge of the product of hydride transfer would change the solvation processes, and thus the substituent effects across solvents.
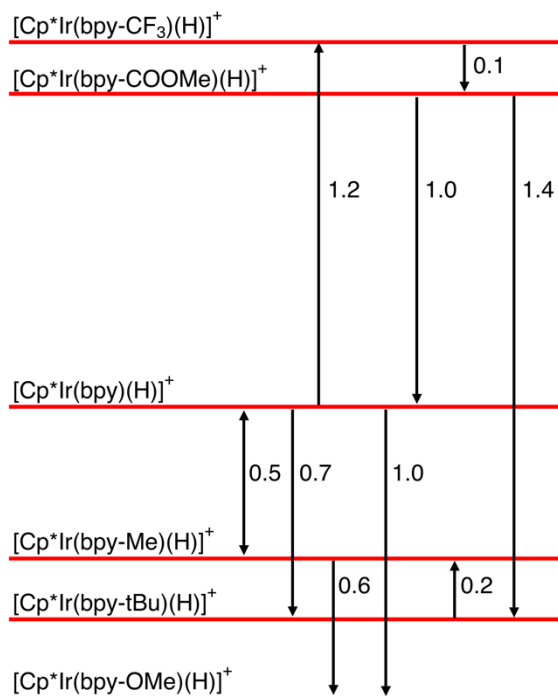
Figure 4.6. Relative hydricity values for hydrides under study in the presence of chloride. Black arrows show relative equilibria with arrow pointing from the starting hydride complex towards the starting nitrile complex for the equilibrium.

Values of relative hydricity to form the chloride are readily available by equilibrium reactions between pairs of iridium hydride and chloride complexes, providing a rapid method to establish the substituent effects in the presence of chloride. Solutions containing various iridium chloride and hydride complexes (as their chloride salts, eq 1) were monitored by ^{1}H NMR spectroscopy to obtain relative hydricities, as illustrated in Figure 4.6.
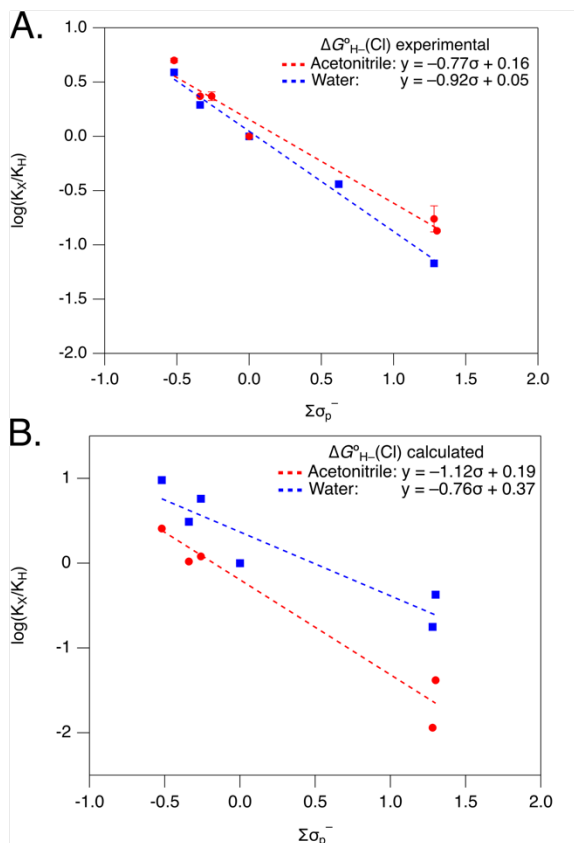
Figure 4.7 A. Hammett correlation of $\Sigma\sigma_p^-$ and $\log(K_X/K_H)$ as measured by hydride equilibration reactions in the presence of chloride. B. Hammett correlation of $\Sigma\sigma_p^-$ and $\log(K_X/K_H)$ as calculated by DFT. Dotted lines show best fit of data points.

Figure 4.7 shows the Hammett plots for $\Delta G^{\circ}_{H-}(Cl)$ in water and acetonitrile. Again, the influence of substitution on the bipyridine ligand on hydricity is relatively constant ($\rho = -0.8$-0.9) regardless of solvation. Relative hydricities calculated via DFT predict a slightly more dramatic effect of solvation on relative hydricities than is observed experimentally. The similar slopes in Figure 4.4 and Figure 4.7 suggests that the 1+/2+ charge difference between the hydride and nitrile complex does not have a significant impact on the solvent influence of electronic effects.

Only relative hydricity values including chloride binding were available from the preceding equilibrium reactions. To obtain effective hydricity values $\Delta G^{\circ}_{H-}(Cl)$ in acetonitrile, the thermodynamic binding affinity of the incoming chloride ligand, $\Delta G^{\circ}_{NCCH_3 \rightarrow Cl}$ was needed. DFT calculations predict binding strengths of $\Delta G^{\circ}_{NCCH_3 \rightarrow Cl} \sim -6$ kcal mol^{-1} for the series of complexes (Scheme 4.4).

Scheme 4.4. Methods used to estimate chloride binding affinity for complex **1NCCH$_3$**.

Estimation based on DFT

$$\Delta G_{rxn} = G(\mathbf{1Cl}) + G(CH_3CN) - G(\mathbf{1NCCH_3}) - G(Cl) \qquad = -6 \text{ kcal mol}^{-1}$$

Estimation based on UV-Vis spectroscopy

$$[\mathbf{1Cl}] \underset{CH_3CN}{\overset{K_d > 10^8 \text{ M}^{-1}}{\rightleftharpoons}} [\mathbf{1NCCH_3}] + [Cl^-] \qquad < -11 \text{ kcal mol}^{-1}$$

Estimation based on H$_2$ Production

$$[\mathbf{1H}]Cl + [HB] \overset{K_{eq}}{\rightleftharpoons} [\mathbf{1Cl}] + [B^-] + H_2$$

$$\Delta G^{\circ}_{H-}(Cl) = -1.364[pK_a(HB)] + 76.0 - RT\ln(K_{eq})$$

$$\Delta G^{\circ}_{NCCH3 \rightarrow Cl} = \Delta G^{\circ}_{H-}(Cl) - \Delta G^{\circ}_{H-}(NCCH_3) \qquad < -12 \text{ kcal mol}^{-1}$$
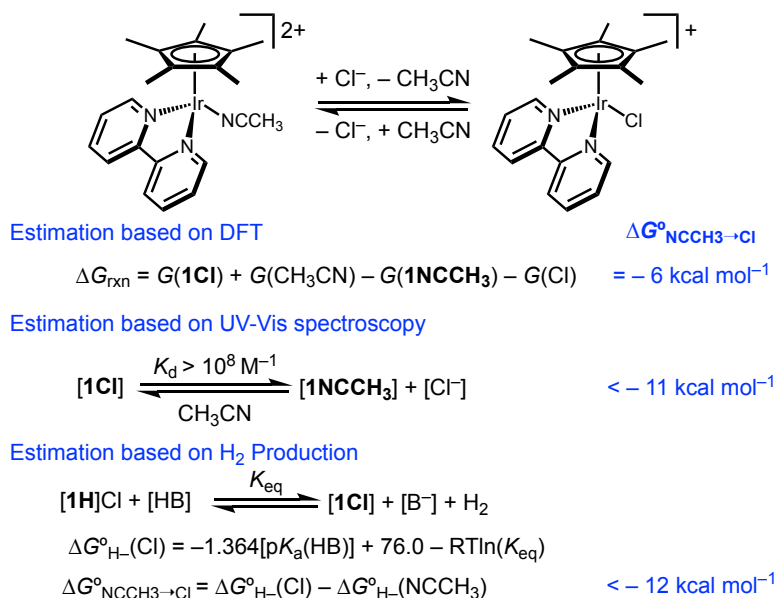
DFT estimates of chloride binding affinity suggested that the chloride binding should be observable by NMR spectroscopy. However, upon dissolution of **1Cl** in CD$_3$CN, no chloride ligand substitution to form the nitrile complex is observed. This indicates that chloride binding is stronger in CD$_3$CN than in D$_2$O, wherein significant amounts of the aquo complex were observed upon dissolution of the chloride complex, *vide supra*. Further confirmation of strong chloride binding was obtained by a titration adding varying concentrations of [PPN][Cl] (PPN = bis(triphenylphosphine)iminium) to a solution of **1NCCH$_3$**. Full conversion to **1Cl** was observed

upon the addition of 1.1 eq of chloride (eq 3), indicating that the Ir-Cl bond strength is too great

to be measured by NMR spectroscopy (Figure 4.8, $K_a > 10^5$ M^{-1}).[48,49]
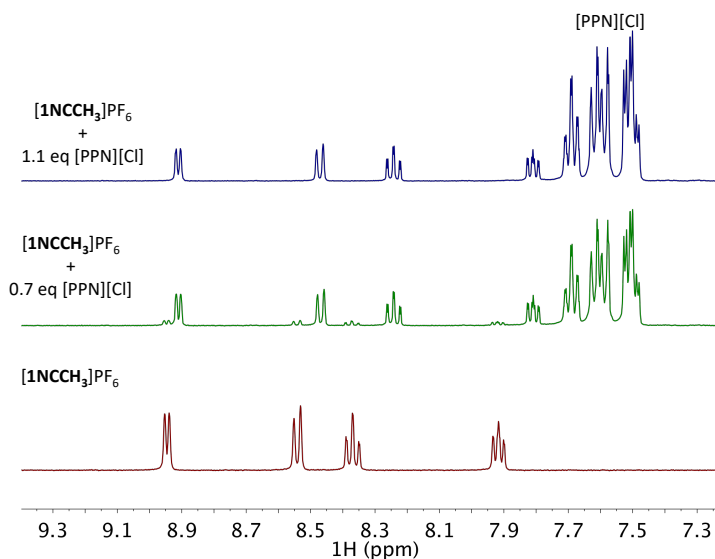
Figure 4.8. ^{1}H NMR spectra of CD$_3$CN solutions of [**1NCCH$_3$**]PF$_6$ with varying amounts of [PPN][Cl] showing complete chloride association at 1.1 eq Cl.

UV-Vis spectroscopy can be used to measure binding affinities where $10^5 < K_a < 10^9$ (−7 kcal mol^{-1} < $\Delta G°_{NCCH_3 \rightarrow Cl}$ < −12 kcal mol^{-1}).[48] Figure 4.9 shows the UV-Vis spectra of separate solutions of 2 μM **1NCCH$_3$** and **1Cl**. The nitrile complex has a diagnostic absorbance band at 320 nm while the chloride has a broad MLCT at 360 nm and structured features between 260 and 290 nm.
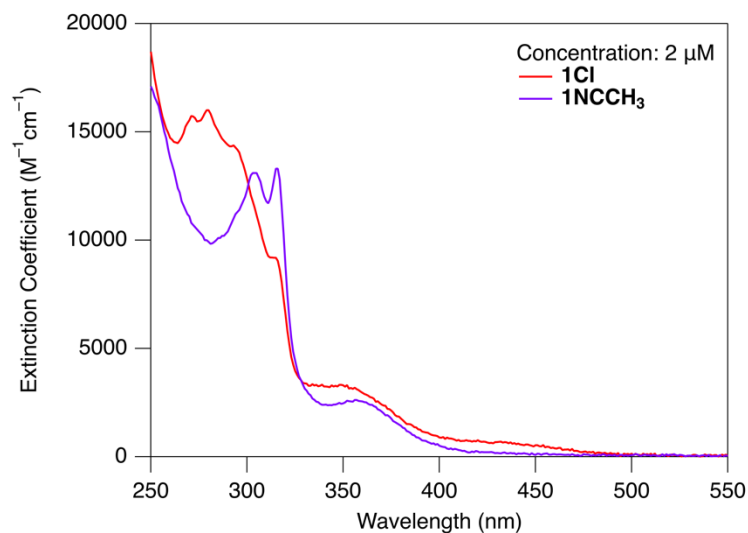
Figure 4.9. UV-Vis spectra of a 2 μM solution of **1NCMe** and **1Cl**. Arrows show changes in absorptivity upon chloride association.

In order to avoid potential complications with the outer-sphere chloride of complex **1Cl**, we sought to synthesize a complex with a non-coordinating outer-sphere anion. Halide abstraction with NaBAr$^F_4$ (Ar$^F_4$ is 3,5-bis-(trifluoromethyl)phenyl) in dichloromethane yielded a yellow solution of [**1Cl**]BAr$^F_4$ upon filtration. In order to determine whether chloride dissociation from the iridium center for this complex could be detected by UV-Vis spectroscopy, solutions of [**1Cl**]BAr$^F_4$ were diluted with acetonitrile. As the concentration of [**1Cl**]BAr$^F_4$ decreases, the mole fraction of [**1Cl**]BAr$^F_4$ also decreases. As seen in Figure 4.9, if chloride dissociates upon dilution, the absorptivity at 320 nm should increase, while the observed extinction coefficient at 360 nm should decrease. However, the observed extinction coefficient for chloride complex [**IrCl**]BAr$^F_4$ only deviated upon dilution to concentrations less than 2 μM, where the instrumental detection limits led to irreproducibility (Figure 4.10). If we assume 10% dissociation of chloride at 1 μM, the association constant for chloride association would be $K_d > 10^8$ M^{-1}, or $\Delta G^o_{NCCH_3 \rightarrow Cl} < -11$ kcal mol^{-1} (Scheme 4.4).
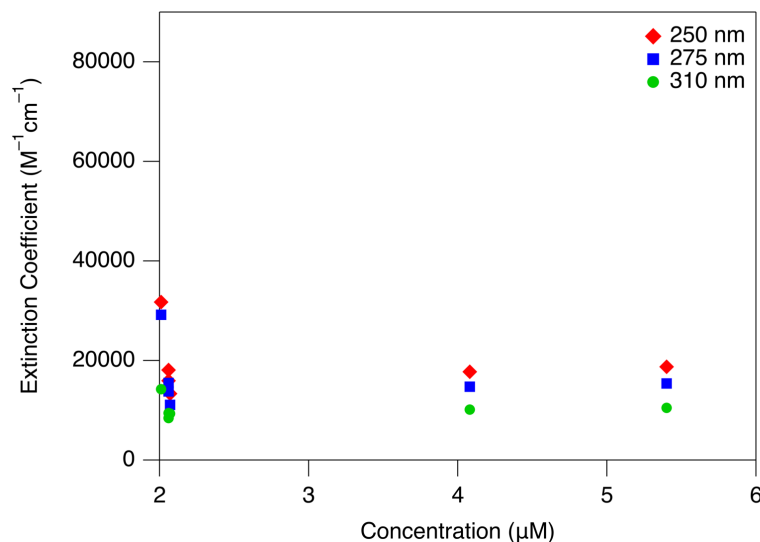
Figure 4.10. Extinction coefficients at three different wavelengths of solutions of [**1Cl**]BAr$^F_4$ upon dilution.

Another method to measure the binding affinity would be to measure the effective hydricity of [**1H**]Cl to form **1Cl** through equilibration with hydrogen and a base (Scheme 4.4). Hydrogen release from a hydride complex is predicted to be thermodynamically favorable in acetonitrile if the sum of the hydricity, $\Delta G°_{H-}$(Cl), and the free energy of proton loss from an acid (1.364pK_a) is < 76 kcal mol^{-1}. By using acids with known pK_a values in acetonitrile, the hydricity for [**1H**]Cl can be estimated. Mixtures of [**1H**]Cl and oxalic acid (pK_a = 14.5) showed partial conversion to the chloride and oxalate complexes after 15 days. However, no hydrogen release was observed when the hydride and triethylammonium tetrafluoroborate (pK_a = 18.82) were combined and monitored for several weeks. These two acids allow us to bracket the hydricity for [**1H**]Cl, 50 kcal mol^{-1}< $\Delta G°_{H-}$(Cl) < 56 kcal mol^{-1}. Using the known value for the hydricity of [**1H**]PF$_6$ ($\Delta G°_{H-}$(NCCH$_3$) = 62 kcal mol^{-1}), this confirms that the presence of chloride makes hydride donation from [**1H**] more favorable by ~ 6-12 kcal mol^{-1}. Taken in

conjunction with the UV-Vis titration studies, these results suggest $\Delta G^{\circ}_{\text{NCCH}_3 \to \text{Cl}} \sim -11$ kcal mol^{-1}.

4.2.7 Kinetic Influence of Chloride on H$_2$ Release

The iridium hydrides studies here have smaller effective hydricity values in the presence of chloride, indicating that they are thermodynamically more potent hydride donors under these conditions. The dramatic influence of the presence of chloride on the thermodynamics of hydride transfer in acetonitrile led us to investigate the kinetics of H$_2$ release in the presence of chloride. One might expect a general trend that stronger hydride donors support faster hydride transfer.

The kinetics of H$_2$ release from [**1H**]PF$_6$ and the relatively strong acid N,N-dimethylformamidium hexafluorophosphate ([HDMF][PF$_6$], pK_a = 6.1) were monitored by UV-vis absorbance spectroscopy. A 0.2 mM solution of [**1H**]PF6 was treated with 10 equiv [HDMF][PF$_6$] and the absorbance at 430 nm was monitored until the reaction had reached completion. The reaction with [HDMF][PF$_6$] was complete in under 200 s. A k$_{obs}$ value under pseudo-first order conditions was obtained from was obtained from a plot of the natural log of the iridium hydride concentration versus time. This value was then used to calculate a second order rate constant of 13.6 M^{-1} s^{-1}. (Figure 4.11).
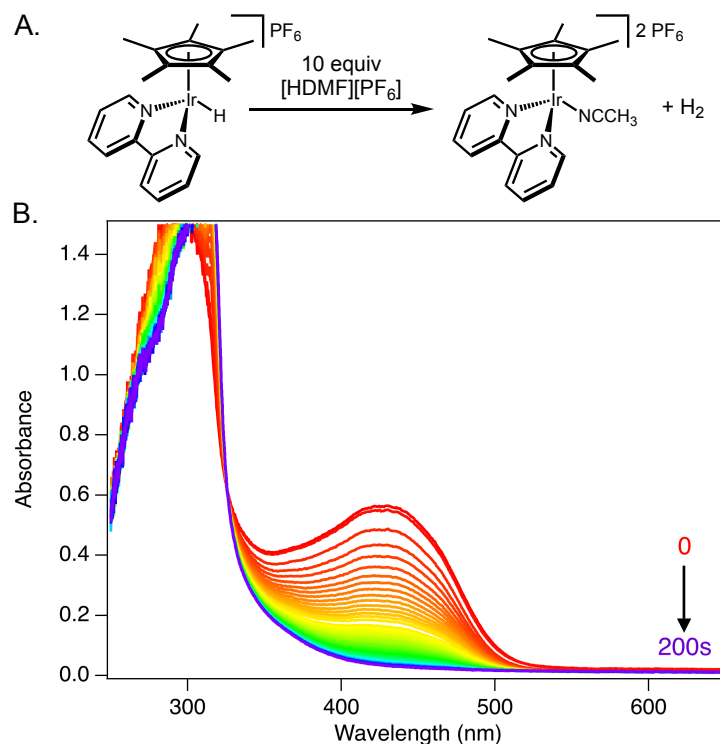
Figure 4.11. A. Reaction of [**1H**]PF$_6$ with 10 eq of [HDMF][PF$_6$] to release H$_2$ and form the nitrile complex [**1NCCH$_3$**][PF$_6$] B. Absorbance spectrum of H$_2$ production reaction over time.

When the same reaction was carried out treating [**1H**][PF$_6$] with 10 equiv [HDMF][PF$_6$] as well as 10 equiv [PPN][Cl], the reaction was dramatically inhibited, with H$_2$ release occurring with $k = 0.2$ M^{-1} s^{-1}). Interestingly, including 10 equiv of DMF in addition to 10 equiv [HDMF][PF$_6$] (without any chloride added) leads to a reaction of intermediate rate ($k = 2.7$ M^{-1} s^{-1}).
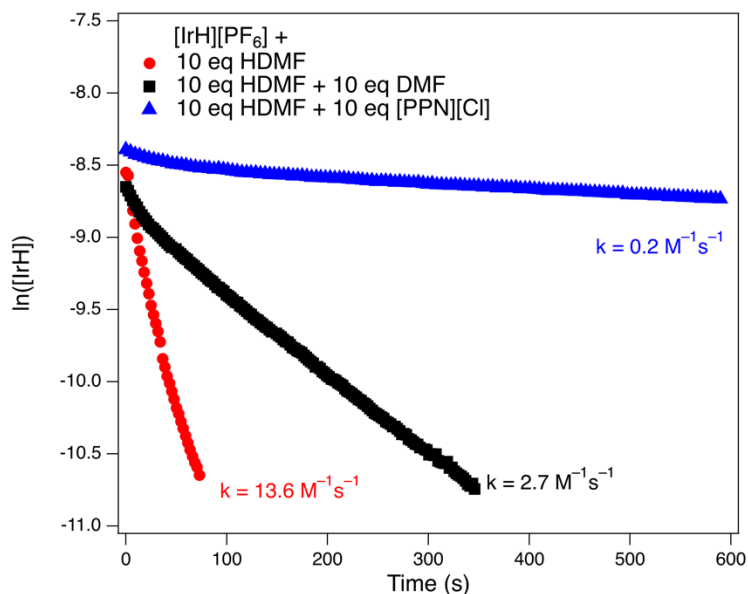
Figure 4.12. First order kinetic plot of the consumption of [**1H**]PF$_6$ over time in the presence of various additives.

We attribute the change in kinetics to Lewis acid/base chemistry involving the acid source [HDMF]$^+$. As shown in Figure 4.12, both DMF and chloride slow down the reaction. The homoconjugation constant for [HDMF]$^+$ is relatively high (K_{HC} = 49 M^{-1})[50], so we hypothesize that the addition of DMF has reduced the *effective acidity* of [HDMF]$^+$ in acetonitrile.[51] In a similar fashion, we propose that heteroconjugation between [HDMF]$^+$ and Cl$^-$ raises the effective pK_a of the acid, resulting in slower H$_2$ production rates. These ion-pairing interactions apparently have a larger effect on the H$_2$ release kinetics than any hydricity differences in this case.

4.3   Conclusions

Presented here is the first example of hydricities of a homologous set of transition metal hydride complexes studied in two solvents. This series of complexes allows us to examine the influence of solvent on (a) the magnitude of hydricity values, (b) electronic tuning through

112

bipyridine substituent effects, and (c) effective hydricity tuning by addition of external ligands, such as chloride, that bind after hydride transfer.
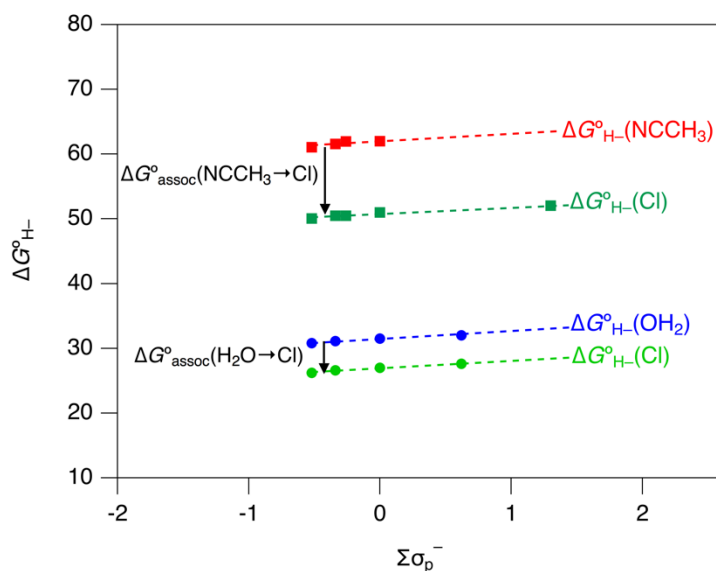
Figure 4.13. Influence of effective hydricity as a function of the sum of the Hammett parameters for each substituent ($\Sigma\sigma_p^-$). The black arrows reflect the various relationships measured in this work. The influence of chloride on effective hydricity within a given solvent is the difference in binding affinity for the complex ($\Delta G^{\circ}_{NCCH_3 \to Cl}$ for acetonitrile and $\Delta G^{\circ}_{H_2O \to Cl}$ for water).

Figure 4.13 gathers all of the thermochemistry measured through the course of this work. As observed in previous work, hydride donation becomes more favorable in water than in acetonitrile, due to the more favorable solvation of the hydride ion ($\Delta G^{\circ}_{tr}(H^-) = -27.7$ kcal mol^{-1} from acetonitrile to water) and the difference in binding affinity for each solvent by the complex. The relative hydricities between iridium complexes (regardless of the presence of chloride) within this series is relatively unchanged in water and acetonitrile, as evidenced by the similar slopes in the Hammett plots in Figure 4.4 and Figure 4.7. The binding affinity for chloride is greater than that for solvent in both water and acetonitrile, however the effect is much more

pronounced in acetonitrile. In acetonitrile, $\Delta G^{\circ}_{NCCH_3 \rightarrow Cl}$ is too strong for determination by both NMR and UV-Vis spectroscopic analysis, and has been estimated as ~ -11 kcal mol^{-1}

Not only are these same modes of catalyst tuning available in both water and acetonitrile, but the solvent itself can be used as an additional mode for catalyst tuning. The electronic influence of the supporting ligand is not strongly affected, such that relative hydricity trends are retained in both solvents. In this way, upon hydricity determination in one solvent across a series of similar complexes, these trends are expected to be conserved across solvent environments. For example, as hydricity determination in acetonitrile is typically more facile, ligand tuning can be explored in acetonitrile and then applied in aqueous media, where many energy-relevant transformations are targeted.

In stark contrast, effective hydricity, in which the thermodynamic parameter involves hydride release and binding of a ligand, such as chloride, is drastically affected by solvent. The relative instability of small anions like chloride in acetonitrile vs water leads to issues of both heteroconjugation or ligation, which influence the thermodynamics and kinetics of hydride transfer. These studies have illuminated a bright future for catalyst tuning using hydricity. Several different methods to tune hydricity have been proposed which have widely varied degrees of influence, allowing for a spectrum of hydricity available to each complex of interest.

4.4   Experimental Section

4.4.1   General Considerations

Procedures were carried out under nitrogen except where noted. All solutions containing metal hydride species were protected from ambient light to prevent photochemical H$_2$ release.[23,24,39] All reagents were commercially available and used without further purification. Organic solvents were dried and degassed with argon using a Pure Process Technology solvent

system. Deuterated solvents were purchased from Cambridge Isotope Laboratories, Inc. [Cp*Ir(Cl)$_2$]$_2$[52] and [HDMF][OTf][53] were prepared following established literature procedure. Substituted bipyridine ligands were commercially available and used without further purification.

UV-Vis spectra were obtained with a Cary 60 spectrophotometer. NMR spectra were obtained on 400, 500, or 600 MHz spectrometers. ^{1}H NMR spectra were referenced to the residual solvent signals. Spectra were processed using the MestReNova software suite from Mestrelab Research S. L.

4.4.2 Synthesis

*General Synthesis of [Cp*Ir(bpy-X)(Cl)][Cl] Complexes:*

The chloride complexes of **1-6** were prepared following the method of Dadci *et al.*, with final precipitation from MeOH/Et$_2$O.[25] The products [Cp*Ir(bpy)(Cl)][Cl] (**1Cl**)[54], [Cp*Ir(bpy-Me)(Cl)][Cl] (**2Cl**)[28], [Cp*Ir(bpy-tBu)(Cl)][Cl] (**3Cl**),[28] [Cp*Ir(bpy-OMe)(Cl)][Cl] (**4Cl**)[55], [Cp*Ir(bpy-CO$_2$Me)(Cl)][Cl] (**5Cl**),[22] and [Cp*Ir(bpy-CF$_3$)(Cl)][Cl] (**6Cl**)[28] were verified by comparison with published literature spectra.

[Cp*Ir(bpy)(Cl)][BAr$^F_4$] ([**1Cl**]BAr$^F_4$): A 20-mL scintillation vial was charged with 0.1 mmol of **1Cl** dissolved in 5 mL dichloromethane. With stirring, 0.1 mmol of NaBAr$^F_4$ (Ar$^F_4$ is 3,5-bis-(trifluoromethyl)phenyl) was added as a solution in 5 mL dichloromethane. The reaction was stirred at room temperature for 1 hour and filtered to give a pale yellow solution of [**1Cl**]BAr$^F_4$ (86% yield, 100% pure) ^{1}H NMR (400 MHz, CD$_3$CN) δ 8.91 (d, $J = 5.6$, 2H), 8.47 (d, $J = 8.4$ Hz, 2H), 8.24 (t, $J = 7.9$, 2H), 7.81 (t, $J = 7.4$, 2H), 7.71 (m, 12H, BAr$^F_4$), 1.68 (s, 15H).

General Synthesis of [Cp*Ir(bpy-X)(NCCH$_3$)][PF$_6$]$_2$ Complexes:

In a nitrogen-filled glovebox, 0.1 mmol of [Cp*Ir(bpy-X)(Cl)][Cl] was added to a scintillation vial and dissolved in 5 mL H$_2$O. Silver hexafluorophosphate (0.21 mmol) was then added to the vial as a solution in 5 mL H$_2$O. The mixture was then stirred at room temperature overnight. The vial was brought out of the glovebox and silver chloride was removed by vacuum filtration yielding a pale-yellow filtrate. Water was removed via rotary evaporation. The solid was then re-suspended in acetonitrile and stirred over 3 Å molecular sieves for 30 mins. The solution was then filtered and dried *in vacuo* to yield the product. [Cp*Ir(bpy)(NCCH$_3$)][PF$_6$]$_2$ (**1NCCH$_3$**) was verified by comparison with known literature spectra.[39] Characterization data for previously unreported complexes is presented below:

[Cp*Ir(bpy-Me)(NCCH$_3$)][PF$_6$]$_2$ (**2NCCH$_3$**) (43% yield, 97% pure) ^{1}H NMR (600 MHz, CD$_3$CN) δ 8.87 (d, *J* = 5.7 Hz, 2H), 8.30 (s, 2H), 7.45 (d, *J* = 5.7 Hz, 2H), 2.46 (s, 6H), 1.61 (s, 15H).

[Cp*Ir(bpy-tBu)(NCCH$_3$)][PF$_6$]$_2$ (**3NCCH$_3$**): ^{1}H NMR (500 MHz, CD$_3$CN) δ 8.99 (d, *J* = 6.1 Hz, 2H), 8.35 (d, *J* = 2.1 Hz, 2H), 7.71 (dd, *J* = 6.1, 2.1 Hz, 2H), 1.63 (s, 15H), 1.45 (s, 18H).

[Cp*Ir(bpy-OMe)(NCCH$_3$)][PF$_6$]$_2$ (**4NCCH$_3$**): (60% yield, 98% purity) ^{1}H NMR (500 MHz, CD$_3$CN) δ 8.65 (d, *J* = 6.6 Hz, 2H), 7.98 (d, *J* = 2.8 Hz, 2H), 7.36 (dd, *J* = 6.6, 2.8 Hz, 2H), 4.11 (s, 6H), 1.66 (s, 15H).

[Cp*Ir(bpy-CO$_2$Me)(NCCH$_3$)][PF$_6$]$_2$ (**5NCCH$_3$**) (59% yield, 100% purity) ^{1}H NMR (500 MHz, CD$_3$CN) δ 9.09 (m, *J* = 5.7 Hz, 4H), 8.31 (d, *J* = 5.9, 2H), 4.06 (s, 6H), 1.69 (s, 15H).

[Cp*Ir(bpy-CF$_3$)(NCCH$_3$)][PF$_6$]$_2$ (**6NCCH$_3$**) (47% yield, 100% purity) Single crystals suitable for X-ray diffraction studies were grown by vapor diffusion of Et$_2$O into an acetonitrile solution of **6NCCH$_3$**. ^{1}H NMR (500 MHz, CD$_3$CN) δ 9.18 (d, J = 5.9 Hz, 2H), 9.02 (s, 2H), 8.24 (dd, J = 5.9, 1.9 Hz, 2H), 1.72 (s, 15H).

*Synthesis of [Cp*Ir(bpy-X)(H)][Cl] Complexes:*

The synthesis of hydride complexes **1H**, **2H**, **4H**, and **5H** with chloride counter ions was reported previously.[8] Synthesis of **3H** and **6H** was adapted from the synthesis of **1H**[8] (characterization data for unreported complexes is presented below).

[Cp*Ir(bpy-tBu)(H)][Cl] ([**3H**]Cl). ^{1}H NMR (500 MHz, CD$_3$CN) δ 8.78 (d, *J* = 6.2 Hz, 2H), 8.48 (d, *J* = 2.1 Hz, 2H), 7.64 (d, *J* = 6.1 Hz, 2H), 1.85 (s, 15H), 1.48 (s, 18H), -11.54 (s, 1H).

[Cp*Ir(bpy-CF$_3$)(H)][Cl] ([**6H**]Cl). ^{1}H NMR (600 MHz, CD$_3$CN) δ 9.18 (d, *J* = 5.9 Hz, 2H), 9.02 (s, 2H), 7.91 (s, 2H), 1.90 (s, 15H), -11.77 (s, 1H).

*Synthesis of [Cp*Ir(bpy-X)(H)][X] Complexes (X = PF$_6$ or OTf):*

The synthesis of complexes [**2H**]PF$_6$, [**3H**]PF$_6$, and [**4H**]PF$_6$, was adapted from the reported synthesis of [**1H**]PF$_6$.[29] The synthesis of complex [**4H**]PF$_6$ was verified by comparison with published spectra[20] and characterization data for unreported complexes are outlined below.

[Cp*Ir(bpy-Me)(H)][PF$_6$]$_2$ ([**2H**]PF$_6$). ^{1}H NMR (500 MHz, CD$_3$CN) δ 8.69 (d, J = 5.9 Hz, 2H), 8.21 (s, 2H), 7.42 (d, J = 5.7, 2H), 2.60 (s, 6H), 1.81 (s, 15H), -11.50 (s, 1H).

[Cp*Ir(bpy-tBu)(H)][PF$_6$]$_2$ ([**3H**]PF$_6$). ^{1}H NMR (500 MHz, CD$_3$CN) δ 8.75 (d, J = 6.1 Hz, 2H), 8.36 (d, J = 2.1 Hz, 2H), 7.59 (dd, J = 6.1, 2.2 Hz, 2H), 1.83 (s, 15H), 1.45 (s, 18H), -11.58 (s, 1H).

The synthesis of [Cp*Ir(bpy-CO$_2$Me)(H)][OTf]$_2$ ([**5H**]PF$_6$) and [Cp*Ir(bpy-CF$_3$)(H)][OTf]$_2$ ([**6H**]PF$_6$) followed the general procedure described below.

The Ir^I complex ([Cp*Ir(bpy-CO$_2$Me)] and [Cp*Ir(bpy-CF$_3$)], respectively) were synthesized from the iridium chloride complexes following established procedures.[8] The Ir^I complex was then dissolved in 10 mL of diethyl ether and a 0.01 M solution of [HDMF][OTf] in acetonitrile was added until the color change from dark purple to red-orange persisted for 1 min. The dark orange solid was then filtered and washed with 3 x 5 mL diethyl ether. The solid was then redissolved in acetonitrile and dried *in vacuo* to yield the product.

[Cp*Ir(bpy-CO$_2$Me)(H)][OTf]$_2$ ([**5H**]PF$_6$) ^{1}H NMR (500 MHz, CD$_3$CN) δ 9.05 (d, *J* = 6.0 Hz, 2H), 8.96 (d, *J* = 1.8 Hz, 2H), 8.00 (dd, *J* = 6.0, 1.8 Hz, 2H), 4.02 (s, 6H), 1.86 (s, 15H), -11.87 (s, 1H).

[Cp*Ir(bpy-CF$_3$)(H)][OTf]$_2$ ([**6H**]PF$_6$). Synthesis yields a mixture of [**6H**]PF$_6$ and **6NCCH$_3$** (77% hydride) due to a small amount of over protonation by the acid to release H$_2$. ^{1}H NMR (500 MHz, CD$_3$CN) δ 9.14 (d, J = 6.1 Hz, 2H), 8.88 (s, 2H), 7.88 (d, 2H), 1.89 (s, 15H), -11.79 (s, 1H).

REFERENCES

(1)   Wang, D.; Astruc, D. *Chem. Rev.* **2015**, *115*, 6621.

(2)   Hull, J. F.; Himeda, Y.; Wang, W.; Hashiguchi, B.; Periana, R.; Szalda, D. J.; Muckerman, J. T.; Fujita, E. *Nat. Chem.* **2012**, *4*, 383.

(3)   Choi, J.; MacArthur, A. H. R.; Brookhart, M.; Goldman, A. S. *Chem. Rev.* **2011**, *111*, 1761.

(4)   Robertson, A.; Matsumoto, T.; Ogo, S. *Dalton Trans.* **2011**, *40*, 10304.

(5)   Burgess, S. A.; Appel, A. M.; Linehan, J. C.; Wiedner, E. S. *Angew. Chem. Int. Ed.* **2017**, *56*, 15002.

(6)   Wiedner, E. S.; Chambers, M. B.; Pitman, C. L.; Bullock, R. M.; Miller, A. J. M.; Appel, A. M. *Chem. Rev.* **2016**, *116*, 8655.

(7)   Brereton, K. R.; Pitman, C. L.; Cundari, T. R.; Miller, A. J. M. *Inorg. Chem.* **2016**, *55*, 12042.

(8)   Pitman, C. L.; Brereton, K. R.; Miller, A. J. M. *J. Am. Chem. Soc.* **2016**, *138*, 2252.

(9)   Taheri, A.; Thompson, E. J.; Fettinger, J. C.; Berben, L. A. *ACS Catal.* **2015**, *5*, 7140.

(10)   Tsay, C.; Livesay, B. N.; Ruelas, S.; Yang, J. Y. *J. Am. Chem. Soc.* **2015**, *137*, 14114.

(11)   Connelly Robinson, S. J.; Zall, C. M.; Miller, D. L.; Linehan, J. C.; Appel, A. M. *Dalton Trans.* **2016**, *45*, 10017.

(12)   Creutz, C.; Chou, M. H.; Hou, H.; Muckerman, J. T. *Inorg. Chem.* **2010**, *49*, 9809.

(13)   Creutz, C.; Chou, M. H. *J. Am. Chem. Soc.* **2009**, *131*, 2794.

(14)   Chantooni, M. K.; Kolthoff, I. M. *J. Phys. Chem.* **1976**, *80*, 1306.

(15)   Bartnicka, H.; Bojanowska, I.; Kalinowski, M. K. *Aust. J. Chem.* **1993**, *46*, 31.

(16)   Suenobu, T.; Guldi, D. M.; Ogo, S.; Fukuzumi, S. *Angew. Chem. Int. Ed.* **2003**, *42*, 5492.

(17)   Ogo, S.; Makihara, N.; Kaneko, Y.; Watanabe, Y. *Organometallics* **2001**, *20*, 4903.

(18)   Gabrielsson, A.; Leeuwen, V.; Kaim, W. *Chem. Commun.* **2006**, 4926.

(19)   Miller, A. J. M.; Heinekey, D. M.; Mayer, J. M.; Goldberg, K. I. *Angew. Chem. Int. Ed.* **2013**, *52*, 3981.

(20)   Ogo, S.; Kabe, R.; Hayashi, H.; Harada, R.; Fukuzumi, S. *Dalton Trans.* **2006**, 4657.

(21)   Himeda, Y.; Miyazawa, S.; Onozawa-Komatsuzaki, N.; Hirose, T.; Kasuga, K. *Dalton Trans.* **2009**, 6286.

(22)   Brewster, T. P.; Miller, A. J. M.; Heinekey, D. M.; Goldberg, K. I. *J. Am. Chem. Soc.* **2013**, *135*, 16022.

(23)   Pitman, C. L.; Miller, A. J. M. *ACS Catal.* **2014**, *4*, 2727.

(24) Barrett, S. M.; Slattery, S. A.; Miller, A. J. M. *ACS Catal.* **2015**, *5*, 6320.

(25) Dadci, L.; Elias, H.; Frey, U.; Hörnig, A.; Koelle, U.; Merbach, A. E.; Paulus, H.; Schneider, J. S. *Inorg. Chem.* **1995**, *34*, 306.

(26) Leigh, G. J.; Sanders, J. R.; Hitchcock, P. B.; Fernandes, J. S.; Togrou, M. *Inorg. Chim. Acta* **2002**, *330*, 197.

(27) Hetterscheid, D. G. H.; Kaiser, J.; Reijerse, E.; Peters, T. P. J.; Thewissen, S.; Blok, A. N. J.; Smits, J. M. M.; De Gelder, R.; De Bruin, B. *J. Am. Chem. Soc.* **2005**, *127*, 1895.

(28) Sasayama, A. F.; Moore, C. E.; Kubiak, C. P. *Dalton Trans.* **2016**, *45*, 2436.

(29) Chambers, M. B.; Kurtz, D. A.; Pitman, C. L.; Brennaman, M. K.; Alexander, J. M. *J. Am. Chem. Soc.* **2016**, *138*, 13509.

(30) Curtis, C. J.; Miedaner, A.; Ellis, W. W.; DuBois, D. L. *J. Am. Chem. Soc.* **2002**, *124*, 1918.

(31) Matsubara, Y.; Fujita, E.; Doherty, M. D.; Muckerman, J. T.; Creutz, C. *J. Am. Chem. Soc.* **2012**, *134*, 15743.

(32) Miller, A. J. M.; Labinger, J. A.; Bercaw, J. E. *J. Am. Chem. Soc.* **2010**, *132*, 3301.

(33) Maity, A.; Teets, T. S. *Chem. Rev.* **2016**, *116*, 8873.

(34) Hansch, C.; Leo, A.; Taft, R. W. *Chem. Rev.* **1991**, *91*, 165.

(35) Hansch, C.; Leo, A. *Substituent Constants for Correlation Analysis in Chemistry and Biology*; John Wiley & Sons, Ltd.: Toronto, 1979.

(36) Jaffé, H. H. *Chem. Rev.* **1953**, *53*, 191.

(37) Shalan, H.; Colbert, A.; Nguyen, T. T.; Kato, M.; Cheruzel, L. *Inorg. Chem.* **2017**, *56*, 6558.

(38) Bordwell, F. G.; Mccallum, R. J.; Olmstead, W. N. *J. Org. Chem.* **1984**, *49*, 1424.

(39) Barrett, S. M.; Pitman, C. L.; Walden, A. G.; Miller, A. J. M. *J. Am. Chem. Soc.* **2014**, *136*, 14718.

(40) Pegis, M. L.; Roberts, J. A. S.; Wasylenko, D. J.; Mader, E. A.; Appel, A. M.; Mayer, J. M. *Inorg. Chem.* **2015**, *54*, 11883.

(41) DuBois, D. L.; Berning, D. E. *Appl. Organomet. Chem.* **2000**, *14*, 860.

(42) Miller, A. J. M.; Labinger, J. A.; Bercaw, J. E. *Organometallics* **2011**, *30*, 4308.

(43) Connelly, S. J.; Wiedner, E. S.; Appel, A. M. *Dalton Trans.* **2015**, *44*, 5933.

(44) Rakowski DuBois, M.; DuBois, D. L. *Acc. Chem. Res.* **2009**, *42*, 1974.

(45) Berning, D. E.; Noll, B. C.; DuBois, D. L. *J. Am. Chem. Soc.* **1999**, *121*, 11432.

(46) Chen, S.; Rousseau, R.; Raugei, S.; Dupuis, M.; DuBois, D. L.; Bullock, R. M. *Organometallics* **2011**, *30*, 6108.

(47)   Konno, Hideo; Kobayashi, Atsuo; Sakamoto, Kazuhiko; Fagalde, Florencia; Katz, Nestor E.; Saitoh, Hideki; Ishitani, O. *Inorg. Chim. Acta* **2000**, *299*, 155.

(48)   Thordarson, P. *Chem. Soc. Rev.* **2011**, *40*, 1305.

(49)   Smith, J. B.; Kerr, S. H.; White, P. S.; Miller, A. J. M. *Organometallics* **2017**, *36*, 3094.

(50)   Brown, H. J. S.; Wiese, S.; Roberts, J. A. S.; Bullock, R. M.; Helm, M. L. *ACS Catal.* **2015**, *5*, 2116.

(51)   Rountree, E. S.; Dempsey, J. L. *Inorg. Chem.* **2016**, *55*, 5079.

(52)   White, C.; Yates, A.; Maitlis, P. M. *Inorg. Synth.* **2007**, *29*, 228.

(53)   Favier, I.; Duñach, E. *Tetrahedron Lett.* **2004**, *45*, 3393.

(54)   Youinou, M.-T.; Ziessel, R. *J. Organomet. Chem.* **1989**, *363*, 197.

(55)   McFarland, J. M.; Francis, M. B. *J. Am. Chem. Soc.* **2005**, *127*, 13490.